Doctoral Dissertation
Doctoral Program in Metrology (38th Cycle)

3D Diagnostic Tools for Cultural Heritage

The use of Photogrammetry to support Conservation and Preservation Strategies

Sara Croci
* * * * * *

Supervisors
Prof. Sabrina Grassini, Supervisor
Dr. Federica Pozzi, Co-Supervisor

Doctoral Examination Committee:

Prof. Luca Lombardo, Politecnico di Torino, Italy
Prof. Francesco Lamonaca, Referee, Università della Calabria, Italy
Prof. Maurizio Spadavecchia, Referee, Politecnico di Bari, Italy

Politecnico di Torino
10th December 2025

La tesi di dottorato è stata redatta a conclusione del percorso di dottorato finanziato a valere sul PNRR, Missione 4, componente 1 "*Potenziamento dell'offerta dei servizi di istruzione: dagli asili nido all'Università*" – Investimento 4.1 "*Estensione del numero di dottorati di ricerca e dottorati innovativi per la pubblica amministrazione e il patrimonio culturale*", tramite il Decreto Ministeriale n. 351 del 9 aprile 2022 .

I hereby declare that the contents and organisation of this dissertation constitute my own original work and does not compromise in any way the rights of third parties, including those relating to the security of personal data.

Sara Croci

Turin, December 10, 2025

Summary

In recent years, the integration of three-dimensional digitization techniques into the field of Cultural Heritage has significantly enhanced the documentation, preservation, and study of artworks. Among these techniques, photogrammetry and multi-band imaging have emerged as powerful, non-invasive tools that provide complementary spatial and radiometric information. However, they are often applied separately, and the potential of combining them within a unified workflow remains largely unexplored.

The primary goal of this dissertation is to employ photogrammetry as an active support tool for the definition of conservation and preservation strategies in the Cultural Heritage field. Beyond its traditional role as a documentation technique, photogrammetry is here investigated as a method capable of detecting and monitoring surface changes and deformation phenomena that can affect artworks over time, thus contributing to preventive conservation practices.

The proposed workflow was first validated through the acquisition of a dimensional reference object, characterized by a well-defined geometry and measured using metrological instruments such as a Coordinate Measuring Machine and a laser scanner. These reference datasets were used to verify the reliability and consistency of the photogrammetric reconstructions. The comparison confirmed that, when properly calibrated and scaled, photogrammetry can produce geometrically consistent 3D models suitable for applications in Cultural Heritage documentation and monitoring.

Following the validation phase, two representative samples, one wooden and one painted wooden, were subjected to thermo-hygrometric aging to simulate deformation phenomena such as warping, cracking, and shrinkage. The samples were acquired before and after the aging process using both laser scanning and the proposed multi-band photogrammetric approach. In this context, the influence of different wavelength ranges on the reconstruction quality of 3D models was assessed in general terms, taking into account how variations in object shape and surface characteristics could affect the performance of the photogrammetric process. The results highlighted the consistency of the proposed workflow and its ability to provide reliable reconstructions suitable for monitoring deformation phenomena over time.

To demonstrate the versatility and applicability of the methodology, several case studies were carried out within the framework of a broader collaborative project between the Politecnico di Torino, the Centro per la Conservazione e il

Restauro dei Beni Culturali "*La Venaria Reale*" (CCR), and the participating museums. These include the photogrammetric reconstruction of gilded and non-gilded bronze sculptures from the Museo delle Civiltà (MuCiv) in Rome, where cross-polarization effectively reduced reflections on metallic surfaces; a comparison between photogrammetry and laser scanning applied to the skull of an Egyptian mummy from the Museo Egizio of Turin, used to design a custom display support; and the multi-band documentation of Chinese polychrome wooden sculptures from the Museo di Arte Orientale (MAO) of Turin, later featured in an innovative exhibition project.

The results confirm that photogrammetry, when properly calibrated and combined with multi-band imaging, is a reliable and versatile technique for the documentation and monitoring of cultural heritage artifacts. It enables the creation of geometrically accurate and radiometrically enriched 3D models that can actively support preventive conservation, restoration planning, and museum dissemination. Future developments should focus on improving the automation of the photogrammetric workflow and on the integration of artificial intelligence, enabling more efficient and continuous monitoring of artworks over time.

Acknowledgment

I would like to express my sincere gratitude to the Centro per la Conservazione e il Restauro “La Venaria Reale”, and in particular to the Wood Sculpture Conservation Laboratory, for warmly welcoming me and hosting my research for an entire year. My deepest thanks go to Dr. Paola Buscaglia, to whom I owe a special acknowledgment for her trust, constant support, and encouragement, without which I might never have undertaken this journey. I am also grateful to Dr. Federica Pozzi, my co-supervisor, as well as to all the colleagues and professionals who make the CCR such an inspiring and enriching environment.

My heartfelt thanks extend to the Museo Egizio of Turin, the Museum of Oriental Art of Turin, and the Museum of Civilizations in Rome, for allowing me to work on such fascinating case studies, and for offering me the unique opportunity to see part of my research presented in exhibition.

I would also like to express my gratitude to Professor Panayota Vassiliou and Professor Asterios Bakolas for welcoming me to the National Technical University of Athens in Greece, and for their constant support and warm hospitality. My sincere thanks go as well to Dr. Stefania Ioannidou for her collaboration and remarkable patience throughout the laser scanner acquisitions.

An immense thank-you goes to Professor Sabrina Grassini, my supervisor, for her unwavering support throughout the entire duration of my PhD. I also wish to extend my thanks to Professor Emma Angelini, Professor Marco Parvis, and all my colleagues at the Politecnico di Torino, for their continuous encouragement and guidance over the years. A special thank-you goes to Leila and Federico, constant guides and points of reference, without whom this journey would have undoubtedly been much more daunting, difficult, and far less enjoyable.

Finally, I would like to express my heartfelt gratitude to my extended family, whose support over these long years of study has been invaluable, thank you for always believing in me and enabling me to embark on this path. To my friends, thank you for the patience, understanding, and for standing by me throughout these years.

I would like to dedicate this thesis to my beloved family

For always encouraging me, and believing in me more than I ever did.

Contents

1 Introduction 1

1.1 Preface and Context 1
1.2 Thesis Outline 3

2 Digitization Techniques for Cultural Heritage 4

2.1 The use of Photogrammetry for Cultural Heritage 5

2.1.1 Introduction 5
2.1.2 Metrological Aspects 7

2.2 Imaging Techniques 8

2.2.1 Multi-band Imaging 8
2.2.2 Acquisition of reflective surfaces 11

3 Challenges in cultural heritage preservation 13

3.1 Introduction 14
3.2 Wooden properties and artifacts 15

3.2.1 Preservation issues 16

3.3 Monitoring deformations 17

4 Design and Development of Samples and Dimensional Reference 19

4.1 The Dimensional Reference 19
4.2 Samples development 20

4.2.1 Wooden sample 21
4.2.2 Painted sample 21
4.2.3 Artificial aging 22

5 Acquisition setup 23

5.1 Introduction 23
5.2 Digital camera 24
5.3 Radiation Sources and Optical Filters 24

5.4 Rotation platform and Markers 25
5.5 3D Reconstruction Methodology and Software 28
5.5.1 Meshroom 28
5.5.2 Metashape 30
5.6 Cross-polarization technique 31
6 Metrological Validation 33
6.1 Introduction 33
6.2 Photogrammetry 34
6.3 Coordinate Measuring Machine 38
6.4 Laser Scanning 42
7 Results and Discussion 48
7.1 Photogrammetric models 49
7.1.1 3D reconstruction Software comparison 49
7.1.2 Multi-band 3D models 51
7.1.3 Influence of wavelength in 3D reconstruction 59
7.1.4 3D model comparison for aging monitoring 60
7.2 Laser scanning models 64
7.2.1 3D comparison for aging monitoring 65
7.3 Cross-technique comparison 68
8 Case studies 72
8.1 Gilded and ungilded bronze sculptures from Museo delle Civiltà of Rome 72
8.1.1 The artifacts 73
8.1.2 Measurement campaign 75
8.2 Human remains of an Egyptian mummy from the Museo Egizio of Turin 86
8.2.1 The archaeological remains 86
8.2.2 Photogrammetric 3D model comparison with Structured Light Scanner 88
8.3 Polychrome wooden sculptures from the Museo di Arte Orientale of Turin 92
8.3.1 The artifacts 92

8.3.2 3D models by Photogrammetry combined with Multi-band imaging..... 93
9 Conclusions 99
10 References.....102

List of Tables

Table 5.1 Fujifilm XT-30 camera specifications. 24
Table 5.2 Minolta MC Rokkor-PF 50mm f/1.7 specifications. 24
Table 5.3 Light source and filter configurations used for the multi-band imaging techniques. 25
Table 6.1 Parameters used during image acquisition. 34
Table 6.2 Processing parameters of the VIS and UVR 3D model reconstruction of the dimensional reference. 37
Table 6.3 Analysis of experimental data comparing edge lengths of the dimensional reference measured by the CMM and photogrammetry.....41
Table 6.4 Analysis of experimental data comparing edge lengths of the dimensional reference measured by the photogrammetry and laser scanner.....44
Table 7.1 Parameters used during image acquisition. 53
Table 7.2 Metashape processing parameters and results.....54
Table 7.3 Processing parameters comparison of the multi-band 3D model reconstruction of the wood sample before the aging process. 59
Table 7.4 Processing parameters comparison of the multi-band 3D model reconstruction of the painted sample before the aging process. 60
Table 8.1 Artifacts in the Auriti's Collection: Inventory number (INV. N°), Century, Dynasty, height and Surface treatment. 76
Table 8.2 Specifications of portable Raman spectrometers: Laser wavelength, laser power, spectrometer model, resolution and spectral range of acquisition. ...80
Table 8.3 Parameters used during image acquisition. 84
Table 8.4 Camera and prime lens specifications; Table from [59]. 88
Table 8.5 Camera and prime lens specifications. 94
Table 8.6 Parameters employed during the acquisitions. 95

List of Figures

Figure 2.1 Schematic overview of the multi-band imaging techniques discussed. summarizing the illumination conditions and the nature of the reflected or emitted radiation, along with information on the penetration depth into the artifact; Figure adapted from [61]. 9

Figure 2.2 Representative diagram illustrating the substitution of RGB channels for the creation of false-color images: IRR-FC on the left and UVR-FC on the right. 11

Figure 4.1 Image of the dimensional reference. 20

Figure 4.2 Image of the wooden sample before the artificial aging process... 21

Figure 4.3 Image of the painted sample before the aging process object. 22

Figure 5.1 Custom-designed rotating platform modeled in AutoCAD, featuring eight markers compatible with Metashape and eight markers compatible with Meshroom, radially distributed around the center. 26

Figure 5.2 3D virtual replica of the platform: above is represented the mesh, and, below, the texture. 27

Figure 5.3 Flowchart of the photogrammetric process. 28

Figure 5.4 Example of a VIS-PL (a), VIS (b), and Specular Map (c) textures generated for the reproduction of a 3D model with metallic surfaces using the cross-polarization technique. 31

Figure 6.1 Image of the dimensional reference acquired during the acquisition process for each of the considered multi-bands. 35

Figure 6.2 VIS point cloud of the dimensional reference (left) and a map of recognized camera positions, in black, and image overlap, in blue (right). 36

Figure 6.3 Final UVR-3D model of the dimensional reference (left) and map of recognized camera positions, in black, and image overlap, in blue (right). 36

Figure 6.4 Results of the several processing steps due to the reconstruction of the 3D model of the dimensional reference in Metashape. 38

Figure 6.5 3D reconstruction of the dimensional reference generated using a Python script based on CMM data. The estimated vertices of the dodecahedron are shown in blue, and the raw measurement are displayed in green. Adapted from [101]. 39

Figure 6.6 3D reconstruction of the dimensional reference generated using a Python script based on CMM data. The estimated vertices of the dodecahedron are shown in blue, and the raw measurement are displayed in green. Adapted from [101]. 40
Figure 6.7 FARO Laser ScanArm Edge during the acquisition of the dimensional reference. 42
Figure 6.8 Final point cloud obtained by photogrammetry from the UV reflectography dataset (above) and by laser scanner (below). The red rectangles highlight details of the point density for each cloud. 45
Figure 6.9 Cloud-to-cloud absolute distances map computed in CloudCompare between the point clouds of the dimensional reference acquired by laser scanning and photogrammetry. 46
Figure 6.10 Histogram of computed absolute distances (mm) extracted in CloudCompare from the cloud-to-cloud comparison between the photogrammetric and scanned acquisition of the dimensional reference. 47
Figure 7.1 Representation of one of the IRR images used for the 3D reconstruction of the wood sample by Meshroom: (a) an image, (b) a masked image, and (c) details of the features (light blue dots), the image matches (orange dots) detected after the alignment process (red dots), and marker's detection (green squares). 49
Figure 7.2 Camera positions detected by Meshroom for the painted sample 3D model reconstructed by masked VIS acquisitions. 50
Figure 7.3 Representative scheme of all acquisitions performed in the different spectral bands, for both the wood and painted samples, before (Epoch 0) and after (Epoch 1) the aging process. 52
Figure 7.4 Black dots are representative of the camera locations of the wood sample (a) and the painted sample (b) before the aging process. In blue, the virtual reconstruction of the acquired objects, located on the platform used for the acquisition setup is presented. 54
Figure 7.5 Results of the several processing steps due to the reconstruction of the 3D model of the painted sample before the aging process in Metashape 55
Figure 7.6 Results of the several processing steps due to the reconstruction of the 3D model of the wood sample before the aging process in Metashape 56
Figure 7.7 Final 3D models of the painted sample before the aging process integrated by the multi-band imaging data. 57
Figure 7.8 Final 3D models of the painted sample after the aging process integrated by the multi-band imaging data. 57

Figure 7.9 Final 3D models of the wooden sample before the aging process integrated by the multi-band imaging data. 58
Figure 7.10 models of the wooden sample after the aging process integrated by the multi-band imaging data. 58
Figure 7.11 Cloud-to-mesh signed distances map (mm) between the photogrammetric models of the wood sample before and after the aging process; computed in CloudCompare. 61
Figure 7.12 Histogram of computed distances (mm) from the 3D surface comparison for deformation monitoring of the wood sample; computed in CloudCompare. 62
Figure 7.13 Cloud-to-mesh signed distances map (mm) between the photogrammetric models, before and after the aging process of the painted sample; computed in CloudCompare. 63
Figure 7.14 Histogram of computed distances (mm) from the 3d surface comparison for deformation monitoring of the painted sample; computed in CloudCompare 64
Figure 7.15 Cloud-to-cloud absolute distance map (mm) computed in CloudCompare between the point clouds acquired by laser scanning, before and after the aging process of the wood sample. In particular, the section of the point cloud in correspondence of a wooden deformation is presented. 65
Figure 7.16 Histogram of computed absolute distances (mm) extracted in CloudCompare from the cloud-to-cloud distance comparison for deformation monitoring of the wooden sample. 66
Figure 7.17 Cloud-to-cloud absolute distance map (mm) between the point cloud acquired by laser scanning, before and after the aging process of the painted sample, calculated with CloudCompare. In details, sections in correspondence of deeper deformations between the point clouds considered: a paint and preparation layer loss (left) and a paint layer lifting (right). 67
Figure 7.18 Histogram of absolute computed distances (mm) from the cloud-to-cloud distance comparison for deformation monitoring of the painted sample; computed in CloudCompare 67
Figure 7.19 Cloud-to-mesh signed distance map (mm) between the photogrammetric mesh and the laser point cloud acquired before the aging process of the wood sample, computed in CloudCompare. 69
Figure 7.20 Histogram of computed distances (mm) from the 3D surface comparison between the photogrammetric and laser scanning technique of the wood sample, acquired before the aging process, computed in CloudCompare 69

Figure 7.21 Cloud-to-mesh signed distance map (mm) between the photogrammetric mesh and laser scanned point cloud acquired before the aging process of the painted sample, computed in CloudCompare. 70
Figure 7.22Histogram of computed distances (mm) from the 3D surface comparison between the photogrammetric and laser scanning technique of the painted sample, acquired before the aging process, computed in CloudCompare. 70
Figure 8.1 Images of six small gilded bronze sculptures from the Auriti's collection of the Museo delle Civiltà of Rome: (a) INV.625, Bodhisattva Padmapani, VI Century, East Wei Dynasty; (b) INV.631, Standing Bodhisattva Avalokitesvara, VI Century, North Wei Dynasty; (c) INV.659, Seated Maitreya, VI Century, Unknown Dynasty; (d) INV. 667, Seated Buddha, VI Century, Wei Dynasty; (e) INV. 669, (f) INV. 670, Buddha with assistants, VI Century, North Qi/Su Dynasty 73
Figure 8.2 Images of four small ungilded bronze sculptures from the Auriti's collection of the Museo delle Civiltà of Rome: (a) INV.650 - Standing Bodhisattva Avalokitesvara, VI Century, Wei Dynasty; (b) INV.695 - Standing Bodhisattva Padmapani, VI Century, North Wei Dynasty; (c) INV. 708 - Bodhisattva in the attitude of "prince through" VI Century, East Wei Dynasty; (d) INV. 710- Buddha in Dyanamudra, V Century, North Wei Dynasty. 74
Figure 8.3 XRF spectra of the ungilded artifact INV. 708. Spectra recorded on different areas of the sculpture, i.e. black, red, bright green, and green. 77
Figure 8.4 XRF Analysis of ungilded artifacts (INV. 708, INV. 695, INV. 650, INV. 710): scatterplot of net-rates of (a) Sb/Rh vs. Ag/Rh; (b) Sb/Sn vs. Ag/Sn. See the legend for color information. 77
Figure 8.5 XRF spectra of the ungilded artifact INV. 625. Spectra recorded in correspondence of gold losses (a), and in presence of gold, showed in comparison with a gold loss (b) 78
Figure 8.6 Raman spectra of artifact INV. 659 acquired in correspondence of reddish compared to the RRUFF reference (database RRUFF, R140763). 80
Figure 8.7 Raman spectra of the artifact INV. 710. Comparison of the tenorite combined with the amorphous carbon spectra acquired in correspondence with a black area with the RRUFF reference (database RRUFF, R120076). 81
Figure 8.8 Raman spectra artifact INV. 667. Comparison of the rouaite in combination with atacamite spectra acquired in correspondence with a green area with the RRUFF references (database RRUFF, rouaite R080086, and atacamite R050098). 82
Figure 8.9 Raman spectra of the areas indicated in the optical images of the artifact INV. 708: Red area of the sculpture; Green area of the sculpture. For

comparison purposes, spectra of cuprite from database RRUFF, R140763 and of clinoatacamite from database RRUFF, R061066; spectrum of amorphous carbon. 82
Figure 8.10 Acquisition strategy of the gilded sculpture INV. 667. 84
Figure 8.11 Texture generated for the VIS and UVL 3D model: (a) Visible texture, (b) Polarized texture, (c) Specular Map, (d) Ultraviolet Luminescence texture. 85
Figure 8.12 3D VIS model of the artifact INV. 667. Starting from left: front view, left view, right view, back view. 85
Figure 8.13 3D UVL model of the artifact INV.667. Starting from left: front view, left view, right view, back view. 86
Figure 8.14 Remains of an Egyptian human (Provv. 0549) mummy with cartonnage mask and painted shroud of the Roman period (30 B.C.E. – 395 C.E.), from the Museo Egizio of Turin. 87
Figure 8.15 The mummy's skull (a) and cartonnage mask (b)temporarily separated from the rest of the body during conservation and restoration activity. 87
Figure 8.16 Acquisition setup for the reconstruction of the skull's 3D model by photogrammetry; Figure from [59]. 89
Figure 8.17 Acquisition setup Acquisition setup for the reconstruction of the skull's 3D model by 3D scanning. 90
Figure 8.18 3D models of the skull of the Museo Egizio of Turin by 3D scanner: (a) mesh; (b) textured 3D model; adapted from [59]. 91
Figure 8.19 3D models of the skull of the Museo Egizio of Turin by photogrammetry: (a) mesh; (b) textured 3D model; adapted from [59]. 91
Figure 8.20 (a) Distance map between the 3D scanner and photogrammetry models (mm); (b): Histograms of computed distances (mm) from the 3D surface comparison computed in CloudCompare; Figure from [59]. 92
Figure 8.21 Acquisition setup the Lohan INV. 454 (left), and the Bodhisattva INV. 450 (right). 94
Figure 8.22 UVL 3D model Bodhisattva INV.450, front (a) and back view (b). 96
Figure 8.23 UVL 3D model Lohan INV.454, front (a) and right view (b). 96
Figure 8.24 IRR (a) and IRR-FC (b) 3D model Bodhisattva INV.450. 97
Figure 8.25 Detail of retouching on the 3D model of Bodhisattva INV.450 in VIS (a), IRR (b), and IRR-FC (c). 97
Figure 8.26 3D model of Lohan INV.454 in VIS (a), IRR (b), and IRR-FC (c). 98

Chapter 1

Introduction

1.1 Preface and Context

This dissertation investigates the capabilities and limitations of some of the most widely used three-dimensional (3D) digitization techniques applied in the field of Cultural Heritage, with a particular focus on their potential use as active tools for preventive conservation and long-term monitoring of artifacts.

Laser scanning and photogrammetry are among the most common 3D acquisition methods in Cultural Heritage. Their popularity has grown in parallel with algorithm improvements, allowing fast, accurate, and semi-automated generation of 3D models. These virtual replicas encode both geometric and surface information, such as shape, colour, and surface texture. As such, they represent a valuable tool for documentation, research, conservation, preservation planning, and public dissemination.

Within this context, photogrammetry plays a key role due to its image-based nature. It provides high-resolution, photorealistic 3D reconstructions and can be easily integrated with other imaging techniques. These qualities make it particularly suitable for applications requiring both geometrical and radiometric information.

The main aim of this dissertation is to evaluate the metrological performance of photogrammetry in detecting macro- and micro-deformations in wooden and painted wooden artifacts, before and after artificial aging. The goal is to assess whether photogrammetry can reliably support quantitative dimensional monitoring over time, and to determine its accuracy, resolution limits, repeatability, and overall uncertainty in comparison to laser scanning, used as gold standard techniques in the cultural heritage field. Additionally, the method was further validated by comparing measurements acquired with a coordinate measuring machine (CMM) to those extracted directly from the 3D model of an object used as a dimensional reference.

Several 3D models of a reference samples were generated under different conditions and acquisition parameters. Moreover, the performance of two different 3D reconstruction software solutions, one open-source and one commercial, was

evaluated in the generation of virtual replicas. By comparing these models from the dimensional and morphological point of view, it was possible to quantify geometric deviations and evaluate the ability of photogrammetry to detect material deformations and degradation phenomena over time. Particular attention was given to the correlation between the state of conservation and the environmental conditions in which the artifacts are preserved, especially for outdoor exposure.

In addition, the integration of multi-band imaging, a technique widely used in conservation and preservation planning, was used to enhance the data content of the photogrammetric models. Multi-band imaging enables the isolation of specific wavelengths of the electromagnetic spectrum, revealing material properties not visible to the naked eye. However, its use is often limited to two-dimensional applications. The implementation of this technique in a 3D context expands its potential, allowing for the generation of radiometrically and geometrically integrated 3D models.

One of the main challenges addressed in this dissertation is the definition of a metrologically verified workflow for 3D photogrammetry in Cultural Heritage. This includes evaluating the instrumental limits, resolution, and uncertainty of photogrammetric acquisitions, particularly in the detection of small-scale deformations. The methodology was validated through experimental comparisons with laser-scanned and CMM data, which provide a reliable dimensional reference due to their well-defined measurement uncertainty. To support this evaluation, a custom dimensional reference object was designed and developed, serving as a controlled test for systematic comparisons. The setup was implemented by user-friendly software tools to allow fast, repeatable, and accessible workflows, suitable for conservators and cultural heritage professionals.

As a case study, wooden and painted wooden samples were selected to represent typical degradation phenomena. Artificial aging procedures were applied to simulate environmental effects, and 3D models were acquired at different epochs to assess the progression of damage. The small size of the samples allowed the instrument to be tested at its minimum focusing distance, enabling the determination of its performance limits.

1.2 Thesis Outline

Chapter 2 – This chapter provides a general introduction to image-based methods used in the field of Cultural Heritage, with particular attention to photogrammetry and multi-band imaging.

Chapter 3 – This chapter introduces the issues that are usually encountered in the field of conservation and restoration of artifacts. It also presents the main characteristics and primary degradation factors of wooden artifacts, highlighting the importance of preventive conservation through the monitoring of deformations over time.

Chapter 4 – This chapter outlines the custom dimensional reference object developed for this dissertation to perform the metrological validation of the photogrammetric acquisition. Moreover, the wooden and painted wooden samples employed to investigate the effectiveness of the wood deformation monitoring by photogrammetry are described.

The design process is thoroughly described, with particular focus on the materials used and the techniques implemented during its development.

Chapter 5 – This chapter describes the acquisition setup used for generating multiband 3D models. Each component of the system is detailed, including the digital camera, light sources, and optical filters. Finally, the software tools used for integrating radiometric and geometric data onto a 3D model are presented.

Chapter 6 – This chapter presents the metrological characterization performed on the reference object, outlining the techniques applied during the process.

Chapter 7 – This chapter presents and discusses the results obtained from monitoring the deformations of the painted sample and the wooden sample before and after the aging process. Specifically, the performance of two different 3D reconstruction software tools and the models generated through multi-band photogrammetric acquisition were evaluated. The influence of the wavelength used for model reconstruction was also assessed. The effectiveness of photogrammetry and laser scanning in monitoring the dimensional variations of each sample over time was evaluated. In particular, the results obtained with both techniques were compared, including acquisitions performed simultaneously on the same sample.

Chapter 8 – This chapter presents several case studies involving historical artifacts, where the multiband 3D imaging approach has been applied.

Chapter 9 – This chapter summarizes the outcomes of the research, highlighting the main contributions and outlining potential directions for future work.

Chapter 2

Digitization Techniques for Cultural Heritage

Nowadays, digitization techniques are an essential tool for preserving, studying, and disseminating cultural heritage. Through bi-dimensional (2D) and three-dimensional (3D) image-based technologies, it is possible to document over time the state of preservation of artifacts, monuments, and archaeological sites of historical and artistic interest with high accuracy, and a non-invasive and non-destructive approach. Moreover, these techniques provide dimensional and morphological crucial data for monitoring and planning preservation activities. The results can be easily shared with conservators, conservation scientists, and scholars through virtual archives and exhibitions, promoting public engagement as well [1], [2], [3], [4], [5], [6].

Among the most widely used digitization methods are:

- Photogrammetry, which creates detailed three-dimensional models from photographic data [7];
- Three-dimensional scanning, which allows the model generation by the use of lasers or structured light [8];
- Multi-band imaging techniques, which provide information beyond the visible spectrum to reveal hidden features depending on the material compositions [3], [9].

In this chapter, the fundamental principles of the techniques described above are presented.

2.1 The use of Photogrammetry for Cultural Heritage

2.1.1 Introduction

Nowadays, the creation of three-dimensional digital models of objects of historical and artistic interest is a standard practice for the preservation and conservation of cultural heritage [10]. This growing diffusion of this practice reflects the active engagement of the scientific community in cultural heritage, with the aim of addressing the specific needs and challenges faced by conservators, researchers, and museums. The main aim of the creation of virtual replicas is to study and document the state of preservation of the works of art [11], [12], [10], providing a detailed record that can be used to support the conservation decision making process.

The models can also be sorted in digital accessible archives allowing for worldwide access to researches, experts and users [13], [14], [15]. Furthermore, advances in computer graphics enable conservators to virtually reconstruct missing elements and simulate the artifact's supposed original appearance, enhancing the understanding of the artifact original context [16], [17], [18].

Even if these technologies are advancing, environmental factors, such as thermos-hygrometric factors, continue to irreversibly damage outdoor artworks. Thus, it is essential to carry out consistent monitoring strategies. In this context, the long-term monitoring of the preservation state of artworks represents one of the most critical and rapidly evolving research areas within the cultural heritage domain [11], [19], [20]. Indeed, by combining high-resolution 3D digitization with more traditional monitoring techniques, it is possible not only to detect and quantify material degradation over time but also to inform preventive conservation measures, ensuring that interventions are timely and minimally invasive.

There are many three-dimensional digitization techniques for creating 3D models. Specifically, these techniques are divided into active, such as laser and structured light scanning, and passive, as photogrammetry, depending on whether an external light source is required. Thanks to the structured coding of the projected light, laser and structured light scanners can digitally capture the morphology of an object's surface with high spatial resolution. These devices generate a dense point cloud, where each pixel encodes the three-dimensional spatial coordinates of the corresponding point. Conversely, photogrammetry relies on the acquisition of overlapping images [10]. Despite having fundamentally different characteristics, 3D scanning technologies and photogrammetry play a key role in the field of cultural heritage because they offer the best balance of quality, portability, acquisition time, and flexibility [21]. Nevertheless, there is often no single tool capable of satisfying all the requirements for achieving a complete 3D reconstruction due to the morphological complexity, shape, and size of an object [22]. For this reason, there are some examples where a combined system of different sensors is preferred [23], [24], [25].

To understand the birth and development of photogrammetry, it is necessary to consider the technological advances that occurred in the 19th century [26]. At first,

the invention of photography by Daguerre 1839 is noteworthy [27]. In the field of cultural heritage, the potential of photography was mainly recognised for reproduction, the study of architectural surveys, and the documentation of the original state of preservation of historic buildings and, more specifically, in the field or archaeology. However, the need to obtain metric information promoted research and development for a single three-dimensional model that is more performant and multi-functional. Then, the term photogrammetry was coined in 1867 by Maydenbauer, currently considered the father of architectural photogrammetry [28], [29], [30], [31]. The evolution of photogrammetry from early analog methods to modern digital workflows underscores its value and importance in cultural heritage preservation, encouraging its development and research.

Photogrammetry relies on the use of multiple images, at least two, and the principle of collinearity. Thanks to the principle of collinearity, it is possible to establish that a point on the surface of a real object and its corresponding image point are connected by a straight line passing through the camera's perspective center. For each point represented in at least two images, defined as homologous points, a collinearity equation is computed. Then, the equation system is solved by the so-called photogrammetric triangulation or bundle adjustment method. While digital photogrammetry requires complex mathematical calculations to enable the reconstruction of the three-dimensional representation, in active systems these information are provided directly by the sensor [10]. However, continuous advances in computer vision and related algorithms have significantly improved the quality and quantity of information that can be extracted from digital images, enhancing the performance of 3D reconstruction methods in photogrammetry. In particular, photogrammetric 3D models can be generated using Structure-from-Motion (SfM), a self-calibrating method that estimates both the internal and external parameters of the camera through bundle adjustment. This technique is combined with Multi-View Stereo (MVS), which identifies corresponding features across multiple images [32].

The feature that most distinguishes photogrammetry from passive sensors is the significantly higher quality of the texture. Thanks to photogrammetry, it is possible to obtain realistic, high-resolution textures that are essential not only for conservators, archaeologists, and researchers but also to enable adequate documentation of the surface appearance [33]. Furthermore, image-based 3D digital acquisition can be integrated with various image acquisition techniques; examples include multi-band imaging [34], [35], reflectance transformation imaging (RTI) [9] or cross-polarization [36]. Furthermore, since the texture generated as an output is essentially a common image file, it can be processed accordingly. In this way, there is today’s growing trend toward using artificial intelligence to automate and improve the extraction of information from images. Examples include image segmentation [37], [38], semantic segmentation [39], [40], [41] and automatic detection of artifact degradation [42], [43]. In addition, recent studies have focused on investigating the challenges that both active and passive digitization systems face when dealing with morphological features, such as reflective or transparent surfaces [44], [45], [46]. In addition, sensor costs can vary significantly [12];

compared to active sensors, photogrammetry is considerably more affordable, making it accessible even to smaller institutions and encouraging the standardization and broader adoption of 3D digital acquisition for works of art.

Unlike active-sensor technologies, which can provide accurate dimensional data or measurements with a known degree of uncertainty (since they are calibrated by their manufacturers) photogrammetric data, though morphologically accurate, do not inherently include dimensional information. Such data must therefore be defined using additional measuring instruments [8]. Despite its widespread use, the metrological evaluation and the definition of acquisition standards for 3D models obtained through photogrammetry are still not fully established across all application fields. In this study, the focus is on monitoring the deformation of wood. The following paragraph introduces the metrological aspects relevant to photogrammetry.

2.1.2 Metrological Aspects

The growing accessibility of 3D scanning technologies has enabled both experts and non-specialists to create digital replicas of real-world objects. While a wide range of software solutions, ranging from commercial to open-source platforms, enables the generation of photorealistic 3D models, they lack clear and affordable dimensional accuracy [47]. From a metrological perspective, photogrammetry can be considered a measurement instrument, where the extracted spatial coordinates are estimations of the actual surface geometry. According to the literature, the accuracy and reliability of these estimations are influenced by several factors, including environmental conditions, operator variability, the properties of the investigated material, the employed methodology, and the hardware–software configuration [48].

Unlike contact or laser-based systems, photogrammetric methods are rarely standardized or certified, complicating the quantification of measurement uncertainty in accordance with the International System of Units (SI) [49]. To ensure scale accuracy, photogrammetric reconstructions typically require the use of known reference distances between at least three well-defined points. This can be achieved through system calibration, physical artefacts, or coded targets integrated into a traceability chain, ideally aligned with existing metrology. In particular, coded markers are optimized for automated detection and allow simultaneous acquisition of multiple reference points from a single viewpoint [49], [50].

Measurement performance can be evaluated in terms of accuracy, which "describes the closeness between measurements and their true values. The closer a measurement is to its true value, the more accurate it is", and precision, "to describe the consistency with which a measurement or set of measurements can be repeated" [51]. Moreover, according to Andrews et al. [51], the resolution of photogrammetric techniques can be quantified through the ground sampling distance (GSD), which is determined by the lens focal length, the pixel size of the sensor, and the distance from the acquired object. Determining the required resolution involves identifying the smallest detail that needs to be captured. For cultural heritage objects, this is

typically in the range of 0.02 to 0.075 mm [52]. To accurately capture such features, the sampling frequency must be at least double the smallest dimension, corresponding to approximately 27–100 pixels/mm. MacDonald [52] recommends a nominal resolution of 50 pixels/mm to ensure accurate detection of features around 0.04 mm [53].

For this reason, the performance of 3D photogrammetric systems is often evaluated through comparative analyses. In fact, specifically, shape variations or surface deviations observed between virtual models of the same object in the same conditions are used to assess the method's accuracy. This can involve comparisons with known geometric references or with models produced by alternative 3D acquisition techniques, typically through alignment and deviation analysis [53]. Common approaches include benchmarking against high-precision systems, for example, laser scanners, comparing with calibrated geometric objects such as spheres or planes, or using repeated acquisitions to produce an averaged model for reference [47], [54], [55], [56], [57], [58], [59]. Quality assessment frequently relies on statistical metrics provided by reconstruction software, although these should be interpreted cautiously given their dependency on internal algorithmic assumptions [58], [60].

2.2 Imaging Techniques

2.2.1 Multi-band Imaging

Multi-band imaging (MBI) is a non-invasive and portable imaging technique. It captures information about a specific range of the electromagnetic spectrum using selected light sources and optical filters, usually mounted directly onto the camera lens. This method is often carried out with modified digital camera to capture and record images of a specific range of the electromagnetic spectrum, equipped with silicon-based sensors. These sensors are sensitive to wavelengths ranging approximately from 200 nm to 1100 nm [61].

Over the past few decades, MBI has become a valuable tool for supporting diagnostic analysis in the field of cultural heritage, widely used for the documentation of artworks and historical artifacts. Its growing popularity is due to its simplicity, rapid execution, cost-effectiveness, and its non-destructive nature.

The materials that constitute cultural objects respond differently to various wavelengths, allowing MBI to reveal features that are invisible to the naked eye, such as underdrawings, retouching, or degradation areas, and to provide qualitative insights into the state of preservation of an object, which are essential for conservation efforts [62], [63], [64].

A general MBI setup involves three main components: incident radiation, the illuminated object, and the recorded radiation resulting from the interaction between them.

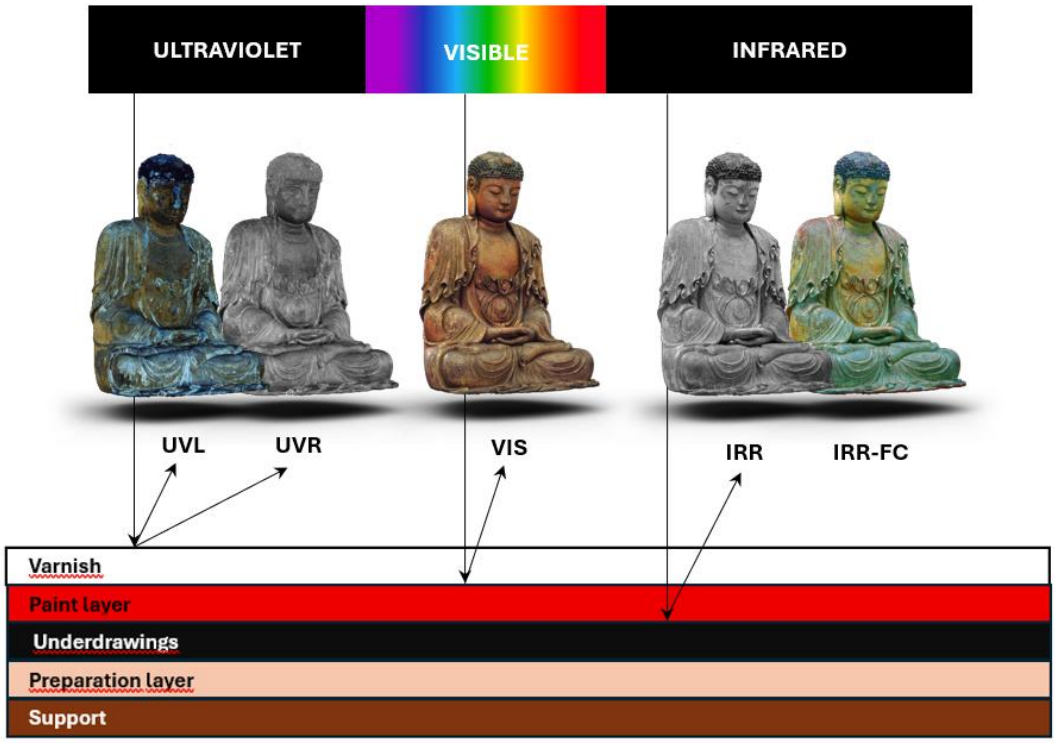

Figure 2.1 Schematic overview of the multi-band imaging techniques discussed. summarizing the illumination conditions and the nature of the reflected or emitted radiation, along with information on the penetration depth into the artifact; Figure adapted from [61].

Depending on the nature of this interaction, the captured signal may fall into two main categories: reflected imaging, where the incident radiation is reflected off the object, as in visible (VIS), infrared (IRR), and ultraviolet reflected (UVR) imaging; and photo-induced luminescence imaging, where the material absorbs the incoming radiation and re-emits it at longer wavelengths, such as in ultraviolet luminescence (UVL) imaging [63], [65], [66], [67]. Figure 2.1 illustrates a schematic representation of the possible interactions between electromagnetic radiation and materials, highlighting the typical penetration depths associated with various wavelengths commonly used in artifact analysis.

The following selections introduce the multiband imaging techniques used in this dissertation.

2.2.1.1 Visible Reflected Imaging (VIS)

Visible Reflected imaging (VIS) refers to the standard acquisition of RGB color data using reflected light within the visible range of the electromagnetic spectrum, typically between 400 and 700 nm. In conservation practice, VIS imaging is commonly employed for documentation purposes and is typically performed at multiple stages of an intervention: before restoration, during intermediate phases such as cleaning, and at the end of the conservation work [65], [68].

2.2.1.2 Infrared Reflected Imaging (IRR)

Infrared Reflected imaging (IRR) is widely employed as a diagnostic tool for the conservation of a broad range of cultural heritage objects, including painted wooden sculptures, easel paintings, painting on canvas, metals, glasses, ceramics, and paper-based materials. Through IRR acquisitions, it is possible to detect variations in material composition that reveal features not visible to the naked eye, such as underdrawings, pentimenti, or materials related to previous conservation treatments [64], [65], [69]. As defined by Warda [70] and Keats Webb [64], the term "infrared reflected imaging" refers specifically to the Near-Infrared (NIR) region of the electromagnetic spectrum, typically between 700 and 1000 nm, which correspond with the sensitivity of digital silicon-based sensors in this range.

2.2.1.3 Ultraviolet Reflected Imaging (UVR)

Ultraviolet Reflected imaging (UVR) involves illuminating the surface of an object with ultraviolet radiation in the 200 – 400 nm range and acquiring the reflected signal within the same spectral region. As UV radiation is primarily superficially absorbed, the technique provides information related to the superficial distribution of materials such as pigments, protective coatings, or other surface treatments [65], [66]. In the field of cultural heritage conservation, UVR is particularly valuable for discriminating between optical similar pigments that exhibit distinct chemical compositions, such as in the evaluation of various white pigments [71].

2.2.1.4 Ultraviolet Luminescence Imaging (UVL)

Ultraviolet Luminescence imaging (UVL) involves the illumination of an object using a UV radiation source within the 200 – 400 nm range, while the emission is recorded in the visible region of the electromagnetic spectrum. This process induces an excitation in the atoms of the material, followed by the emission of visible radiation. The characteristics of the emitted light depend not only on the excitation wavelength, but also on the material’s composition and its aging degree [68]. Provided that exposure thresholds are not exceeded, the method is considered non-invasive. UVL imaging is commonly applied in the field of cultural heritage for the evaluation of the preservation state of objects, the detection of retouching or restoration materials, and to verify the presence and distribution of protective layers [71].

2.2.1.5 False-Color Imaging

False-color imaging consists in the generation of a trichromatic image by combining data acquired through ultraviolet reflectography (UVR) or infrared reflectography (IRR) with information from the visible spectrum. This process produces "false colors”, visual representations that do not correspond to natural perception, which are useful for distinguishing materials such as pigments based on their chemical composition.

In UVR False-Color (UVR-FC) imaging, the visible image is split into the red, green, and blue (RGB) channels. The red and green channels are replaced with the green and blue channels of the original visible image, while the blue channel is substituted with the UVR image. On the other hand, IRR False-Color (IRR-FC) imaging involves replacing the red channel with the IRR image and substituting the green and blue channels with the red and green channels from the visible image, respectively. The RGB channel replacement process is illustrated in Figure 2.2 [65].

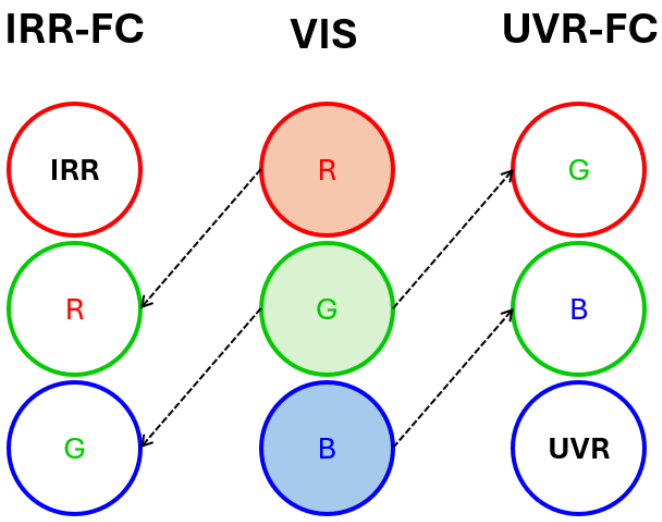

Figure 2.2 Representative diagram illustrating the substitution of RGB channels for the creation of false-color images: IRR-FC on the left and UVR-FC on the right.

2.2.2 Acquisition of reflective surfaces

Cross-polarization is a photographic technique used to acquire images that are free from reflections by polarized light. Light polarization is achieved by placing a linear polarizing filter in front of the light source. To complete the cross-polarization setup, a second polarizing filter is mounted on the camera lens and rotated 90° relative to the first [36], [72], [73], [74].

The limited adoption of this method makes it relevant to assess its potential applicability in additional contexts, such as conservation and cultural heritage. Moreover, although applied to two-dimensional imaging, cross-polarization can also be integrated into three-dimensional imaging workflows using photogrammetry. For each image, two acquisitions are required: one using non polarized light, and a second with polarized light. During post-processing, these two images are used to generate two distinct textures, one polarized and one cross-polarized, which are subtracted to produce a third, known as the “specular map”.

The specular map is a grayscale image that encodes surface reflectance: dark regions correspond to non-reflective areas, while light regions indicate high reflectivity. This map is used during rendering to apply surface reflections only

where they are physically present, thereby enhancing the realism of the 3D model and improving the representation of metallic or glossy materials [36].

Chapter 3

Challenges in cultural heritage preservation

The conservation of historical and artistic artifacts requires not only a multidisciplinary approach but also the application of rigorous, standardized criteria. These efforts aim to preserve the material integrity and cultural value of objects over time. Conservation practice principles include:

- *minimal intervention*: limits actions to those strictly necessary for stabilization and preservation [75];
- *reversibility*: employs materials and techniques that can be removed without compromising the original artifact [75], [76];
- *compatibility*: involves selecting materials that are chemically and physically compatible with the original substrates, thereby avoiding adverse interactions[75].

Scientific and technological tools are necessary for evaluating the state of preservation and for determining appropriate conservation strategies. By providing information about the physical and chemical properties of constituent materials, these tools allow for a thorough assessment of an object's susceptibility to degradation and its interaction with the material used in conservation treatments. Assessment of environmental conditions remains equally important. Factors such as temperature, relative humidity, ultraviolet radiation, air pollutants, and thermohygrometric fluctuations all have significant impacts on the long-term stability of materials.

Each material exhibits specific physical and chemical properties and responds differently to environmental factors, including degradation mechanisms and storage conditions. In this study, the focus is placed on a single material, wood, due to its widespread use in cultural heritage artifacts. As an organic material, wood is particularly sensitive to environmental variations, especially in outdoor settings,

where significant thermo-hygrometric fluctuations can induce both reversible and permanent deformations, including structural cracking.

To contextualize the challenges associated with the analysis and conservation of wooden artifacts, this chapter provides an overview of the material properties of wood and the conservation issues related to its preservation.

3.1 Introduction

This chapter presents the main challenges faced by conservators when working with cultural heritage objects, with a specific overview of wooden works of art and properties.

Upon the arrival of an artifact in the conservation laboratory, the initial step is the documentation of its preservation state. A thorough examination from an art-historical perspective provides essential information regarding the object's provenance, dating, and attribution. On the other hand, scientific investigation uncovers data on original materials and techniques. This combination of knowledge enables conservators to make informed decisions, respect the original materials, and slow down the natural aging process.

Given the unique and irreplaceable nature of these objects, non-invasive and non-destructive analytical techniques are essential in the conservation of cultural heritage. Unlike other fields, where some level of alteration may be acceptable, cultural heritage conservation prioritizes the preservation of the object’s integrity.

Preventive conservation also plays a crucial role. Especially in the case of organic material such as wood, monitoring environmental conditions, including temperature, and humidity variations, is key to minimizing the risk of harmful chemical or physical transformations.

Conservation is inherently multidisciplinary. Conservators work in close collaboration with art historians, archaeologists, photographers, chemists, physicists, biologists, and conservation scientists. Their role is not necessarily to provide definitive answers, but to ask the right questions to specialists, which requires effective communication and interdisciplinary cooperation. Despite its importance, the scientific study of conservation materials and techniques remains an emerging field and has recently gained increased attention from the scientific community.

The selection of conservation materials must follow specific criteria: they have to be compatible with the original materials, avoid unwanted chemical or physical reactions, and be reversible. In many cases, transparency and colorlessness are also required. However, many materials currently used were not originally developed for conservation purposes, and most are not environmentally sustainable. As a result, the search for eco-friendly and sustainable conservation materials has become a significant area of research. Often, conservators are forced to balance ideal material properties with practical constraints, leading to compromises. Consequently, many conservation interventions today involve removing past treatments that have caused further deterioration, frequently due to insufficient preliminary study.

For these reasons, it is essential to support conservation work with scientific tools and methodologies. While the experience and intuition of the conservator remain fundamental, objective and measurable data are crucial to better assess both the preservation state of the object and the impact of the materials used. Scientific support ensures that conservation efforts are as effective, respectful, and durable as possible.

3.2 Wooden properties and artifacts

Wooden artifacts in historical and artistic heritage include a wide variety of objects, ranging from ancient artifacts, such as Egyptian coffins, to more recent examples like marquetry and wooden furniture. The diversity of artifact types, manufacturing techniques, and wood species is considerable. However, a preliminary and general classification can distinguish between wooden and painted wooden artifacts.

Wood is an organic material whose cell walls are primarily composed of the organic polymers cellulose and lignin, which exhibit complementary mechanical properties. Both polymers are hydrophilic and readily absorb moisture. Specifically, cellulose forms chemical bonds with water molecules, resulting in dimensional changes in the cell walls. As a result, when water is absorbed, the wood swells; on the other hand, when moisture evaporates, the wood shrinks [77], [78]. Some of the fundamental properties of wood include:

- *Anisotropy* – The physical and mechanical properties of wood depend on the direction in which they are measured (radial, longitudinal, or tangential section). Its morphological characteristics also vary according to the section being analyzed;
- *Hygroscopicity* – Wood inherently contains a certain amount of water bound to its cell walls. If the wood is very moist, such as fresh or waterlogged wood, an additional amount of unbound or free water is present. The moisture content is calculated as the percentage ratio between the current weight and the oven-dry weight of the wood. By convention, moisture content above 30% indicates the presence of free water;
- *Biodegradability* – Wood is highly susceptible to degradation by biological agents, such as fungi and insects. However, it is also a remarkably durable material: it does not deteriorate intrinsically over time, but only because of external agents. This durability is evident in the survival of ancient wooden structures such as Egyptian coffins, historical bridges, and centuries-old churches;
- *Variability* – A wide variety of plant species produce wood, leading to a significant range of physical and chemical properties among different types of wood [78].

Historically, in the context of art and cultural heritage, wood has often been considered a "poor" material, particularly in the creation of polychrome wooden

sculptures, where symbolic value often outweighed artistic recognition, unlike other materials more traditionally associated with fine art, such as paintings on canvas.

Today, conservators may encounter untreated wooden surfaces, wood covered with one or more protective coatings, or painted surfaces. Additionally, the presence of restoration materials, structural modifications, or later additions must always be considered. In particular, wooden sculptures frequently exhibit many alterations from their original appearance. These characteristics make wooden artifacts, especially polychrome ones, highly complex in terms of conservation analysis, due to the presence of several and frequently undocumented pictorial stratifications. Nevertheless, this complexity also makes them of significant interest. It is not uncommon to find a stratigraphy consisting of multiple paint layers, each corresponding to a different historical phase in the artifact's life [77].

3.2.1 Preservation issues

When the cell walls of wood absorb or release moisture (u), dimensional changes occur, known respectively as swelling and shrinkage. As mentioned previously, the properties of wood vary depending on the species, the environmental conditions during growth, its age, and geographical origin. Consequently, its dimensional variation is directly proportional to its density [78].

Generally, the dimensional changes in wood are reversible, provided the moisture content remains between the anhydrous state (u = 0%) and the fiber saturation point (u ≈ 30%). Total shrinkage is calculated by the sum of the linear shrinkage along the three anatomical directions of the wood: *axial*, which generally exhibits negligible shrinkage; *radial*, which shows moderate shrinkage; and *tangential*, which is typically responsible for the most significant deformations [77], [78], [79], [80], [81]. Another critical factor influencing dimensional stability is the type of cut used to produce the wooden object. To minimize deformations and improve shape stability, tangential or radial cuts are generally preferred.

The primary types of wood deformation caused by shrinkage and swelling, and the anisotropic nature of wood, include:

- *Distortion* – A wooden element cut from fresh wood will undergo volume reduction and substantial deformation during the drying process;
- *Cracking* – If the wooden material contains part of the pith, angular shrinkage induces internal stress, often resulting in deep cracks;
- *Warping* – In boards without pith, the outer portion tends to shrink more, with the convex side oriented toward the pith. Greater thickness and tangential orientation amplify this effect;
- *Mowing* – Caused by greater axial shrinkage at the edge of the board, leading to longitudinal bending;
- *Arching* – Results from abnormal shrinkage in a localized area, along the transverse direction, creating a “barrel-shaped curvature”;
- *Twisting* – Occurs when the central part of the board shrinks or when the grain is irregular, causing the entire board to rotate around its axis [77], [78].

Although deformation due to shrinkage and swelling is inevitable, it is significantly influenced by fluctuations in the ambient relative humidity and the rate at which these changes occur. Exposure to thermo-hygrometric conditions that differ from those under which the wood was originally seasoned or dried further amplifies the problem. When wooden elements are constrained, such as by nails or, in the case of boards, by crossbars, the impossibility to accommodate natural dimensional movements can lead to mechanical stress and structural damage [78].

3.3 Monitoring deformations

As previously emphasized, preventive conservation plays a key role in today's conservation strategies. Its main aim is to slow down the natural aging process and, consequently, the deterioration of artifacts, thereby reducing the need for direct interventions. In this context, the study and understanding of an artwork's state of preservation becomes essential. Constant monitoring enables the evaluation of material behavior and its response to external agents and environmental changes over time [77], [82], [83].

This is particularly crucial in the case of organic materials with heterogeneous and unpredictable properties, such as wood. For such materials, three-dimensional monitoring of structural changes has become a necessary tool. By the comparison of multiple acquisitions of an object's geometric structure over time, it is possible to detect and quantify ongoing deformations [82]. These measurements can be performed *in situ*, both indoors and outdoors, and are valuable for everyday maintenance as well as emergency assessments.

Monitoring is also essential for the development of sustainable conservation strategies and to identify the primary causes of deterioration. Through continuous observation of dimensional variations, potential damage can be anticipated before more invasive interventions become necessary. Moreover, the detection and analysis of active deformations support the design of customized structural supports, tailored to the specific behaviour of each object. It is also important to consider the presence of elements made from modern wood materials, which may have been added during previous restorations and could exhibit different mechanical and hygroscopic behaviour compared to the original components [84].

Wood deformation can be monitored using both contact and non-contact systems. Contact systems involve the use of sensors, such as strain gauges, which provide data on displacement and/or deformation within the wooden structure [81], [85]. In contrast, non-contact systems rely on optical methods, such as photogrammetry and laser scanning. These methods do not require physical contact with the artifact and offer high levels of accuracy [86], [87]. Because of this, they are particularly suitable for the monitoring and conservation of archaeological objects [84], [82], historic buildings [83], and even underwater archaeological sites [88].

In this context, this thesis aims to assess the suitability of photogrammetry for dimensional monitoring of deformations in wooden and polychrome wooden artifacts, a representative sample was selected for painted and non-painted works

of art. The samples were acquired both before and after an artificial aging process. All acquisitions were carried out using both photogrammetric methods and laser scanning, allowing for dimensional accuracy comparison. Additionally, to validate the methodology, different 3D acquisition systems, characterized by different resolutions and accuracies, were tested on an object used as a dimensional reference standard. Details regarding the samples and the acquisition setup are presented in the following chapters.

Chapter 4

Design and Development of Samples and Dimensional Reference

This chapter presents the different objects/samples, which were used in this research as references for monitoring deformations over time by visible and multi-band photogrammetry acquisition. In particular, a custom reference object was developed to serve as a dimensional reference for 3D reconstruction. The reference was used to assess the dimensional accuracy of reconstructed 3D model by photogrammetry, by comparison with laser scanning as ground truth/gold standard. Additionally, a comparison was conducted between the side lengths of the sample measured using a Coordinate Measuring Machine (CMM) and the corresponding dimensions extracted from the photogrammetrically reconstructed 3D model.

After the validation of the photogrammetric method, a wooden and a painted wooden sample were produced to represent typical wooden artifacts to serve as reference for dimensional monitoring of wooden deformation. The samples undergo artificial aging, and they were acquired before and after aging, using both photogrammetry and laser scanning as gold reference.

The design and development of the reference samples are presented in the following sections.

4.1 The Dimensional Reference

A custom object was developed as a dimensional reference for assessing 3D models generated by photogrammetric methods. The design process is summarized as follows. To ensure traceability to length standards, the object was modelled with distinct, sharp edges in a dodecahedron shape, using FreeCAD [89], an open-source CAD software. It was fabricated by a 3D printer (ProJet 2500 Plus by 3D Systems) using VisiJet® M2R-GRY, a UV-curable resin. The resulting object had a smooth

surface and uniform grey colour. To improve its suitability for photogrammetric reconstruction, specific surface features were added during design, including holes on each face for identification and ticks along the edges. These elements were intentionally added to increase the Scale-Invariant Feature Transform (SIFT) algorithm, used to identify key features across different images regardless of their scale, and support reliable image matching within photogrammetric workflow. On each face, a pentagon was cut from white paper and applied, with the face number visibly indicated. In Figure 4.1 the dimensional reference is presented.

Figure 4.1 Image of the dimensional reference.

4.2 Samples development

The samples were made from coniferous wood, specifically a type of fir. To induce measurable deformations during the artificial aging process, sections were selected along the longitudinal–tangential section, incorporating material discontinuities such as knots and resin. It is essential to emphasize that the main aim of this study is not to characterize the aging process in wooden artifacts, but rather to evaluate photogrammetry as a measurement technique for detecting geometric deviations at both macroscopic and microscopic scales. Two reference specimens were created: the first designed to simulate the structural degradation and deformation of wood, and the second for analyzing and monitoring the degradation processes affecting a polychrome layer applied to a wooden support.

Detailed descriptions of the samples are provided in the following sections.

4.2.1 Wooden sample

The wooden sample (55 x 20 x 55 mm) shown in Figure 4.2 was made from fir wood with natural defects, such as knots and pith. It represents an uncoated wooden artifact, without any preparatory, pictorial, or protective layers. The sample is used to study deformation phenomena, including warping and shrinkage cracks. Dimensional changes are encouraged by both the wood's structural irregularities, the use of wooden tangential section, and the effects of artificial aging.

Figure 4.2 Image of the wooden sample before the artificial aging process.

4.2.2 Painted sample

The painted sample (55 x 20 x 55 mm) was prepared using the same fir wood as the first specimen. In this case, the substrate also includes natural defects such as knots, resin deposits, and a portion of the pith. The sample consists of the following sequential layers: a wooden support, a preparation layer, a pictorial film, and a final varnish coating.

The stratification was designed to replicate the typical structure of a common polychrome wooden artifact. The preparation layer consists of plaster (Cts®, Gesso di Bologna), prepared with animal glue (Bresciani®, lapin glue), applied by brush in a uniform thickness. Above this, a layer of tempera, formulated by a mixture of red earth pigment and egg yolk, and a small amount of egg white and vinegar, was applied by brush. Then, a floral decoration was added using a synthetic yellow ochre tempera (Winsor&Newton®, Gouache), also applied by brush. The use of both naturally and synthetic binding media was intended to assess the capabilities of multi-band imaging techniques in differentiating between materials with distinct chemical compositions. Finally, a natural mastic varnish was applied to one half of the sample surface to highlight the challenges associated with the acquisition of glossy and reflective coatings compared to matte and homogeneous surfaces, and

for the multi-band acquisition. In fact, the applied coating exhibits specific luminescent properties when exposed to ultraviolet (UV) radiation. Figure 4.3 shows the sample, with some details of its structure.

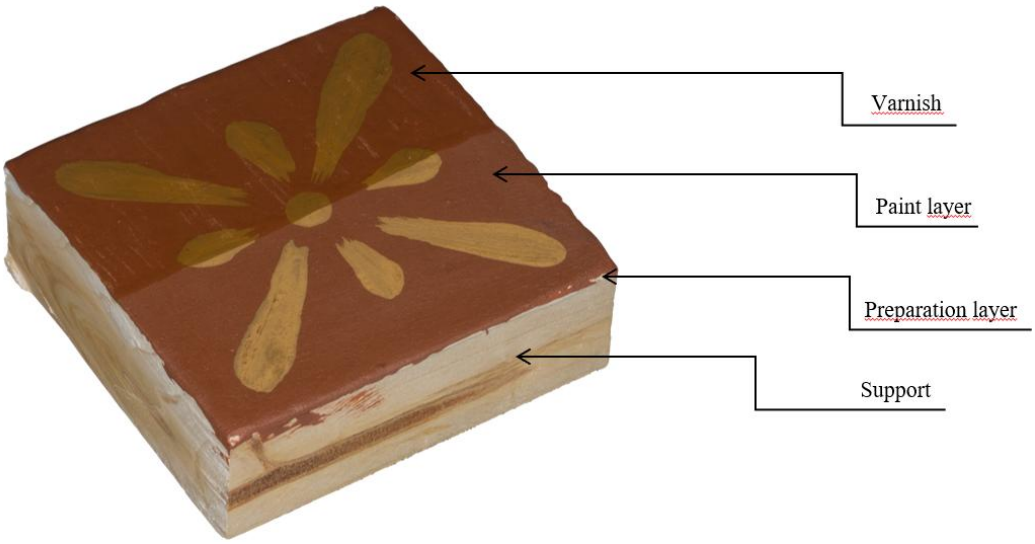

Figure 4.3 Image of the painted sample before the aging process object.

4.2.3 Artificial aging

The samples were subjected to accelerated thermo-hygrometric stress in order to induce artificial aging. The aging cycle was conducted over a period of 25 days and consisted of repeated 12-hour intervals under the following controlled conditions:

- In a drying oven (Binder ED115), at a temperature of 85°C
- In a laboratory glass desiccator at the ambient temperature of 24°C, and 100% of relative humidity
- In a freezer, at a temperature of -20 °C

It is important to clarify that the primary objective of this study is to investigate the wood deformation mechanism. The purpose of the artificial aging process was to generate deformations from millimeters to micrometers within a limited time frame. Repeated and abrupt fluctuations in temperature and humidity promote cycles of moisture absorption and desorption within the wood structure. These cycles induce internal mechanical stresses. As a result, warping, cracking, and other permanent dimensional changes develop more quickly.

Chapter 5

Acquisition setup

5.1 Introduction

The acquisition setup has been specifically customized for this research to be suitable for digitizing small to medium-sized objects (ranging from few, up to some tens of centimeters). In this study, the setup was employed to acquire multi-band 3D virtual replicas of the dimensional reference object and the samples described in Chapter 4, using the following imaging techniques: ultraviolet-induced visible luminescence (UVL), infrared reflectography (IRR), ultraviolet reflectography (UVR), false-color infrared reflectography (IRR-FC), and false-color ultraviolet reflectography (UVR-FC).

The system consists of several components and can therefore be modified based on the specific requirements of the studied object. In this chapter, the elements of the acquisition setup are presented. In particular, the system is composed by:

- A modified digital camera, to capture and record images of a specific range of the electromagnetic spectrum;
- A rotating platform equipped with scaling markers, to allow the artifact rotation around its axis and scaling in its actual size;
- Radiation sources, to supply the required radiation;
- Filters, to select a specific range of the electromagnetic spectrum.

Each of the elements outlined above is described in detail in the following sections.

5.2 Digital camera

A full-spectrum digital camera was used for the image acquisition to enable the creation of 3D digital models integrated with multi-band imaging. In particular, a commercially available camera was specifically modified to increase its sensitivity to the electromagnetic spectrum beyond the visible range of 380 nm to 700 nm to 200 nm to 1100 nm [90]. Specifically, the IR-blocking hot mirror filter commonly contained within commercial digital cameras was removed. In detail, the camera is a Fujifilm XT-30, paired with an APS-C X-Trans 1 CMOS 4 sensor. All the camera specifications are listed in Table 5.1.

Table 5.1 Fujifilm XT-30 camera specifications.

Fujifilm XT-30	
Image size (pixels)	4608 × 3072
Resolution (megapixels)	26.1
Sensor size	23.5mm× 15.6mm (APS-C)
Sensor type	X-Trans CMOS 4
Pixel size (μm)	4.94
ISO range	160−12800

Table 5.2 Minolta MC Rokkor-PF 50mm f/1.7 specifications.

Minolta MC Rokkor-PF 50mm f/1.7	
Focal length	50 mm
Minimum aperture	f/1.7
Maximum aperture	f/16
Focus type	Manual
Type	Prime

A Minolta MC Rokkor-PF 50mm f/1.7 fixed focal length lens was used with the camera system. Table 5.2 provides a detailed overview of the lens specifications. To ensure that the photogrammetry software can accurately detect corresponding features across multiple images, all camera and lens settings were kept constant throughout the image acquisition process. For this reason, only manual focus prime lenses were employed. The camera was securely mounted on a tripod during all acquisitions to maintain a fixed orientation and to avoid variations in perspective.

5.3 Radiation Sources and Optical Filters

This section describes the sources used for each imaging technique, along with the optical filters required to isolate the relevant signal. The filters were mounted directly onto the lens. Table 5.3 provides a summary of the light source and filter combinations employed for each of the multi-band imaging techniques considered.

Table 5.3 Light source and filter configurations used for the multi-band imaging techniques.

Multi-band Imaging	Light source	Filter
VIS	VIS	VIS
VIS-PL	VIS	VIS and polarizing filters
UVL	UV	VIS
UVR	UV	UV
IRR	IR	IR

For the acquisition of reflected images in the visible range of the electromagnetic spectrum, a JJC (Shenzhen Jin Jia Cheng Photography Equipment Co., Shenzen, China), ring light composed of 60 LEDs (4 W) was used as the radiation source. The device provided constant illumination with adjustable brightness and a color temperature of 5600 K. It was mounted directly onto the camera lens. During all acquisitions, the brightness was kept constant. To polarize the light source, a linear polarizing sheet filter (RENIAN Optics Co., Ltd., China), was manually shaped to fit the ring light and applied directly in front of it.

To block UV and IR radiation, a HOYA UV&IR Cut filter, transmitting only the visible range (400–700 nm), was used in combination with a long-pass filter, similar to the Schott BG40 filter, which also cuts out almost all infrared radiation and significantly attenuates red wavelengths. These filters were coupled for the VIS acquisitions. To enable the VIS-PL acquisitions, a second linear polarizing film was mounted in front of the lens. Referring to the polarizer applied to the visible light source, the second polarizer, was oriented at 0° for visible-reflected imaging (VIS), and at 90° for cross-polarized imaging (VIS-PL).

To perform ultraviolet-induced visible luminescence, the polarizing filter in front of the lens was removed, and two UV LED lamps (3000 mW, AC/battery operated) with an emission centered at 365 nm were used to provide the required illumination.

UV reflectography was performed using the same UV sources employed for luminescence, but with the addition of a Baader U-Filter placed in front of the lens. This filter blocks the entire visible and infrared spectrum, allowing only electromagnetic radiation in the 320–380 nm range to pass through.

Infrared-reflected imaging was performed using two 850 nm battery-operated IR sources and an 850 nm long-pass filter, which blocks UV and visible radiation (200–700 nm).

5.4 Rotation platform and Markers

Photogrammetric 3D reconstruction requires the acquisition of a series of digital images from multiple viewpoints, with sufficient overlap to facilitate image alignment and model generation [12]. Two primary image acquisition strategies are commonly employed. In the first, the object is fixed while the camera is moving around to capture images from various angles. In the second, the camera remains

stationary while the object is placed on a rotating platform, which is incrementally rotated to maintain the required overlap between successive images [34].

In this study, the second configuration was used, specifically customized for capturing the geometry of the wooden samples and the dimensional reference. The objects were placed onto a platform with a diameter of 20 cm, equipped with steel spheres to enable smooth manual rotation. A custom reference pattern, designed in Autodesk AutoCAD, as illustrated in Figure 5.1 was fixed to the platform surface. This pattern included eight 12-*bit* coded targets compatible with Agisoft Metashape v. 2.0 software, alternated with eight additional markers, CCtags, detected by the open-source photogrammetry software AliceVision Meshroom v.2025.1.0 [91]. Both types of markers were included to enable a comparative analysis between the models generated by the two different photogrammetry software, including both commercial and open-source software. The markers were arranged radially around the object to ensure consistent spatial referencing. Additionally, an angular degree step was signed around the platform edges to guide uniform rotational increments, ensuring a consistent number of images were acquired at regular intervals.

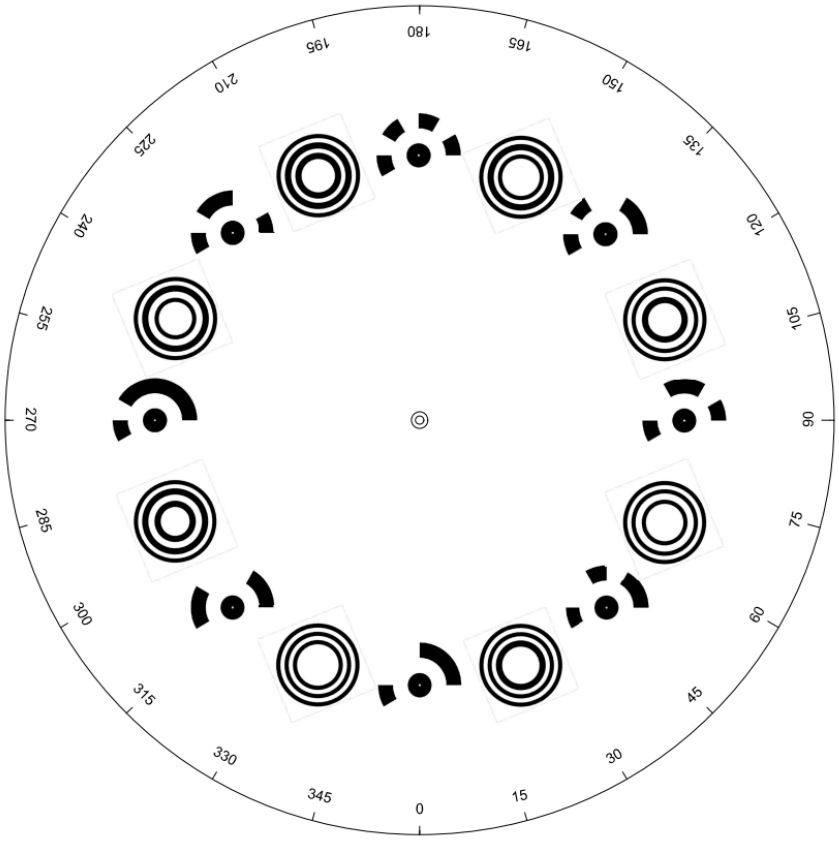

Figure 5.1 Custom-designed rotating platform modeled in AutoCAD, featuring eight markers compatible with Metashape and eight markers compatible with Meshroom, radially distributed around the center.

It should be noted that, for model scaling, the coordinates of both reference targets had to be manually entered. The distances between the markers were measured using CloudCompare, based on a 3D model of the rotating platform surface acquired by structured light scanner.

In details, the tool used to scan the rotating platform was an Artec Space Spider (Artec 3D, Luxembourg). This device uses blue light LED technology and is designed for high-resolution scanning. It operates effectively at a working distance between 170 mm and 350 mm, and is capable of capturing fine details on both small and large industrial objects. According to the manufacturer, it offers a resolution of up to 0.1 mm and an accuracy of up to 0.05 mm. Additionally, it features a 1.3 megapixel camera for capturing texture data.

Figure 5.2 3D virtual replica of the platform: above is represented the mesh, and, below, the texture.

During the scanning process, the device was manually moved around the object at an approximate distance of 30 cm. Data acquisition and processing were carried out using Artec Studio Professional, version 18.0. In Figure 5.2 the virtual replica of the platform is presented. The Artec device provides medium-resolution texture acquisition, essential for manually identifying and visualizing measurement points in CloudCompare.

5.5 3D Reconstruction Methodology and Software

In details, the computational processing were carried out on a workstation running a 64-bit Windows operating system, equipped with 196 GB of RAM, an Intel® Xeon® Gold 6128 CPU @ 3.40 GHz, and an NVIDIA Quadro P4000 GPU.

Figure 5.3 illustrates the photogrammetric workflow, from image acquisition to the three-dimensional digital reconstruction of the object.

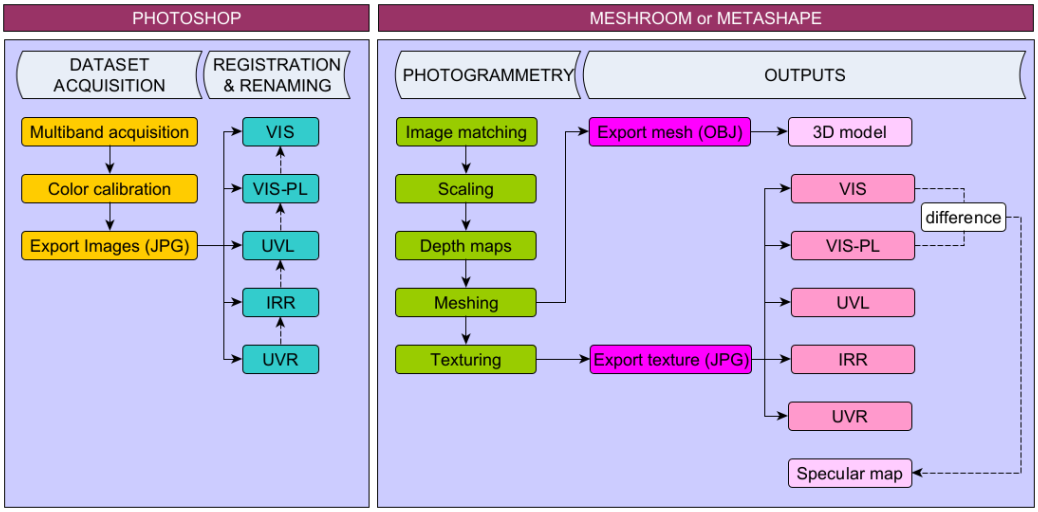

Figure 5.3 Flowchart of the photogrammetric process.

5.5.1 Meshroom

Meshroom is an open-source software, which offers the significant advantage of being freely accessible. It requires only a camera for data acquisition and is characterized by ease of use, and not limited to professionals or experts in the field [91], [92]. However, Meshroom is based on a manual node-based pipeline. While this structure allows greater control over each individual processing step, it often requires more time to identify the appropriate parameters for model reconstruction compared to more automated systems.

As an open-source tool, Meshroom relies on community support and documentation, and software updates depend directly on the AliceVision development team and external contributors [93]. The reconstruction workflow in Meshroom is created by connecting fundamental processing nodes, which can be adapted according to the needs of the specific application. Optional modules, such as custom filters, may be integrated to address particular requirements [94]. An

example is the use of masks to isolate selected regions of the images to be included in the 3D reconstruction process. In detail, the Meshroom processing pipeline consists of the following steps:

- *Camera Initialization*, analyzes the EXIF metadata of the input images (such as focal length and sensor size) to determine the camera model and the acquisition settings used;

- *Feature Extraction*, detects keypoints (features) in each image, recognizable and repeatable elements such as corners, edges, and textures, that can be matched across different views;

- *Image Matching*, compares the images to identify correspondences among keypoints appearing in multiple views, in order to determine the relative viewpoints from which a given 3D point was observed;

- *Features Matching*, evaluates the associations between key points (features) across the images by the previous node (Feature Extraction) and increase the model reconstruction accuracy;

- *Structure from Motion* (*SfM*), using the matched features, estimates the position and orientation of each camera and generates a sparse point cloud that approximates the 3D structure of the scene;

- *Prepare Dense Scene*, prepares the necessary data structures and refines the information from SfM for the Dense Cloud reconstruction phase;

- *Depth Map Estimation*, computes a depth map for each image, estimating the distance from the camera to each point in the scene;

- *Depth Map Filtering*, removes unreliable or noisy depth data to improve the consistency of the reconstruction;

- *Meshing*, Integrates all the depth maps into a continuous 3D surface by generating a mesh composed of interconnected triangles;

- *Meshing Filtering*, optimizes the mesh by removing artefacts, isolated or poorly defined triangles, and improving the overall quality of the geometry;

- *Texturing*, applies surface textures (i.e., colour and detail) to the 3D mesh using the original images to produce a realistic appearance;

This procedure can be applied to the reconstruction of a digital 3D model acquired in visible light or across different spectral bands. The quality of the 3D model generated from each of the considered multi-band acquisitions is directly influenced by the number of features detected by the SIFT algorithm, which can vary depending on the spectral band used during image acquisition. For example, a

model reconstructed from a set of images acquired under UV-induced luminescence conditions may present challenges due to variations in the luminescence intensity, which depends on the chemical composition of the materials being imaged. Such variations may reduce the number of detectable features and, consequently, the reconstruction accuracy.

To address this limitation, Meshroom allows for the generation of multiple textures for a single 3D model using an additional set of images that differs from the one used to create the point cloud and the mesh. The prerequisite for this operation is that both the camera and the object remain in fixed positions and orientations during all acquisitions across the different spectral bands. To implement this, the Prepare Dense Scene node must be duplicated in the processing pipeline, enabling the system to recalculate the necessary data using the new image set. At this point, a new texture can be generated and applied to the initial 3D model, effectively integrating multi-band data onto a single geometry.

The final result is a multi-band 3D model mapped within a single coordinate system, in which the visible acquisition can be integrated with data from ultraviolet-induced visible luminescence (UVL), infrared reflectography (IRR), ultraviolet reflectography (UVR), false-color infrared reflectography (IRR-FC), and false-color ultraviolet reflectography (UVR-FC).

5.5.2 Metashape

Metashape [95] is a stand-alone photogrammetric software that enables the generation of digital three-dimensional models through the digital image process. It supports images acquired using RGB, thermal, or multi-band cameras, and converts them into spatial data in the form of dense point clouds and textured polygonal models. The platform offers an automated and user-friendly processing environment, while also providing advanced features for specialist users. Among the licensed software solutions, Metashape is the most widely reviewed and is frequently used as a benchmark for evaluating other software in the context of 3D reconstruction of cultural heritage objects [96], [97], [98].

The processing workflow of Metashape is largely like that of Meshroom. However, after the generation of the sparse point cloud, Metashape provides an additional functionality (Gradual Selection) which enables filtering of the cloud based on parameters such as reprojection error and reconstruction accuracy. In particular, the reprojection error represents the pixel distance between the calculated position of a 3D point and its actual location in the image. A lower reprojection error leads to a more accurate model, and an average value of less than one pixel is generally recommended. Conversely, reconstruction accuracy is related to the reconstruction uncertainty of the 3D points. A high reconstruction uncertainty, indicating lower accuracy, suggests that the point is geometrically unstable. This typically occurs when the point is generated from images with a small baseline, meaning a short distance between camera positions, which results in a less reliable triangulation. This step allows for the optimization of camera alignment and helps reduce noise resulting from initial alignment inaccuracies.

Moreover, unlike Meshroom, Metashape automatically detects the 12-bit coded targets used for model scaling. This feature facilitates the placement of metric references, as scale bars, thereby streamlining and accelerating the model scaling process.

5.6 Cross-polarization technique

Although photogrammetry provides numerous advantages, its application is limited to certain materials. Because the method is based on the identification of homologous points in images, it may encounter difficulties when reconstructing the geometry of shiny, reflective, or metallic objects. In these cases, variations in surface reflectance due to changes in light incidence and viewing angle reduce the reliability of point matching and, consequently, the accuracy of the reconstructed model.

Some methods have been investigated to improve the applicability of photogrammetry to reflective materials [55], [99]. Among these, increasing image redundancy and using cross-polarization have shown effective results [36]. For shiny or metallic surfaces, polarized light reduces reflection variability, allowing a more stable acquisition of image correspondences and a more accurate reconstruction of shapes and surfaces. The resulting 3D models present improved accuracy, as polarization enhances the detection of geometric details and preserves the object's morphological characteristics.

(a) (b) (c)

Figure 5.4 Example of a VIS-PL (a), VIS (b), and Specular Map (c) textures generated for the reproduction of a 3D model with metallic surfaces using the cross-polarization technique.

The cross-polarization technique is particularly effective in applications such as industrial design, archaeology, and cultural heritage documentation, where geometric accuracy and surface quality are critical [36].

To apply cross-polarization in photogrammetry, each VIS image must correspond to a VIS-PL image acquired using polarizing filters, as described in Section 5.3. Both datasets (VIS and VIS-PL) are imported into the same chunk for alignment and homologous point identification. The combined use of the two

datasets provides complementary information that enhances reconstruction quality, especially in the presence of strong reflections. After alignment and dense cloud generation, a texture is created for each dataset: the VIS texture includes reflections, while the VIS-PL texture is fully polarized.

From these two textures, a third map, the Specular Map, is derived. This texture allows the rendering software to reproduce the correct reflectance only where the surface is actually reflective. It is obtained in post-processing through raster graphic software, such as Adobe Photoshop, using the "Subtraction" blending mode to compute the difference between the VIS and VIS-PL textures. The resulting color file is converted to grayscale and adjusted to match the rendering's illumination parameters (Figure 5.4c).

Because light behavior is complex to reproduce in a virtual environment, different rendering models have been developed to simulate its interaction with materials. Using a rendering 3D software, such as Blender or Sketchfab, several approaches can be applied. The method proposed here set the material behaviours by customizing the following properties, called "material shaders":

- Base Color - the VIS-PL texture (Figure 5.4a), representing the so-called "albedo", the real color of the material not affected by the reflective component;

- Metalness - the Specular Map (Figure 5.4c) added as a grayscale texture;

- Specular - Determine how surface irregularieties affect the reflection of light. As for Metalness, the Specular Map is applied.

In the Metalness map, bright areas correspond to higher reflectance, while dark areas indicate low reflectance. This approach effectively highlights features of interest, such as scratches, grooves, or losses of metallic film, thus improving the interpretability of complex reflective surfaces.

The described cross-polarization method is based on the workflow proposed by Frost et al. [15].

Chapter 6

Metrological Validation

6.1 Introduction

This chapter focuses on evaluating the dimensional accuracy of a 3D model acquired through photogrammetry by the comparison with the ground truth. The comparison was performed on a custom-made dimensional reference, specifically designed for this purpose, as described in Chapter 4. This was a preliminary comparison, with the main goal of verify the efficiency of the photogrammetric setup before the deformation monitoring of two wooden samples before and after the artificial aging process.

In particular, the dimensional reference was measured using a Coordinate Measuring Machine (CMM) and a laser scanner. These scientific instruments are characterized by different levels of known dimensional accuracy uncertainties, unlike photogrammetry.

The photogrammetric acquisition of the dimensional reference was conducted using both visible and multi-band imaging. Specifically, the object was acquired by visible-reflected light, infrared reflectography, ultraviolet reflectography, and ultraviolet-induced visible luminescence. The goal is to compare the photogrammetric 3D models reconstructed from each spectral band in order to assess any differences in the geometric reconstruction.

This chapter provides a description of the techniques employed and the corresponding results about:

- *Photogrammetry* – description of the acquisition setup and presentation of the 3D models of the dimensional reference obtained;
- *Coordinate Measurement Machine* – description of the instrument and the results obtained. The measurements performed on the dimensional reference were compared with those derived from the corresponding photogrammetric 3D model;
- *Laser Scanning* – description of the instrument and the results obtained. Then, the comparison between the measurements of the dimensional

reference performed by the photogrammetric and scanned 3D model is presented. Moreover, the cloud-to-cloud comparison between the digitization technique considered is performed.

6.2 Photogrammetry

This section presents the results obtained from the reconstruction of 3D model of the dimensional reference. The models were generated using a combination of multi-band imaging and photogrammetry. Each 3D reconstruction is acquired from several multi-band imaging techniques. In particular, the imaging techniques used include VIS-reflected imaging, IR-reflected imaging, UV-induced visible luminescence, and UV-reflected imaging. All the images were acquired using the setup described in Chapter 5.

This analysis was carried out to assess variations in reconstruction quality. Preliminary observations indicated that the IRR band could yield improved geometric definition compared to visible-spectrum acquisitions [53]. This enhancement is attributed to the higher penetration depth of IR radiation. However, such effects depend on the optical and material properties of the object investigated. Specifically, IR imaging may reveal sub-surface features, such as preparatory drawings or carbon-based pigments [100], due to the transparency of common organic coatings in this spectral range. To record the infrared reflectography, the image acquisition was performed using a modified camera equipped with a bandpass filter centered at 850 nm.

In parallel, UV imaging was conducted in both luminescence and reflectography modes. For UVL acquisitions, the camera was fitted with an optical filter isolating the visible range (Schott BG40 UVIR cut, 400–700 nm). For UVR imaging, a dichroic filter selecting the 320–380 nm range was used (Baader-U).

During image acquisition, the camera was fixed at a 45° inclination, and the images were captured at 10-degree horizontal intervals. To achieve full surface coverage of the dimensional reference, it was acquired in four rounds and different inclinations by sequentially rotating the object. A total of 144 images were acquired for each multi-band imaging technique. The acquisition parameters are summarized in Table 6.1.

Table 6.1 Parameters used during image acquisition.

Parameter	**Value**			
	VIS	**IRR**	**UVL**	**UVR**
Shutter Speed	2.5s	4s	15s	20s
Acquired Images	144 (36x4)	144 (36x4)	144 (36x4)	144 (36x4)
ISO	80	80	800	800
Camera Tilt	45°			
Image Size	6240x4160			
Image Format	RAF			
Focal Length	50 mm			
Aperture	f/16			
Horizontal Step Angle	10°			
Camera-object distance	~50 cm			

The reconstruction of the 3D models was performed using the photogrammetric pipeline embedded in Metashape, as described in Section 5.5.2. Then, the models were scaled using the reference markers as outlined in Section 5.4. It should be noted that, despite the acquisitions performed in different multi-bands, Metashape was able to reconstruct a 3D model of the dimensional reference only in the UVR and VIS bands. The high degree of symmetry and surface homogeneity of the dodecahedron substantially hindered the image-matching process, resulting in reconstruction failure in the other bands. Furthermore, in both the VIS and UVR bands, image alignment was successful only when the markers were identified before the alignment phase, providing the software with a priori information on their relative spatial positions. Without this preliminary information, the software was unable to complete the image-matching process.

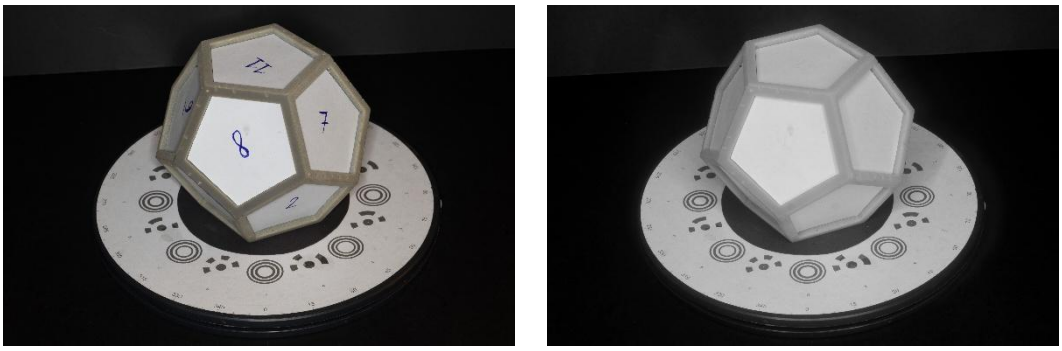

a) VIS b) IRR

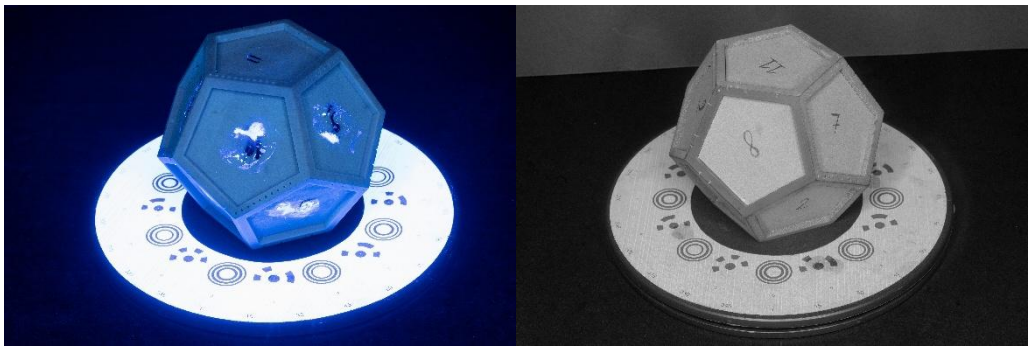

a) UVL d) UVR

Figure 6.1 Image of the dimensional reference acquired during the acquisition process for each of the considered multi-bands.

In

Figure 6.1, representative images acquired during the acquisition setup in each of the considered multi-bands of the dimensional reference are shown. To maintain methodological consistency, only the 3D models reconstructed from VIS and UVR data were considered. The UVL and IRR models were excluded due to insufficient reconstruction. Notably, during UVL acquisition, the white paper pentagons on the dimensional reference were removed to mitigate interference from their inherent luminescence. In both UVL and IRR, the relatively low surface texture and the

reduced contrast of the acquired images resulted in an inadequate number of homologous points, precluding accurate 3D model generation.

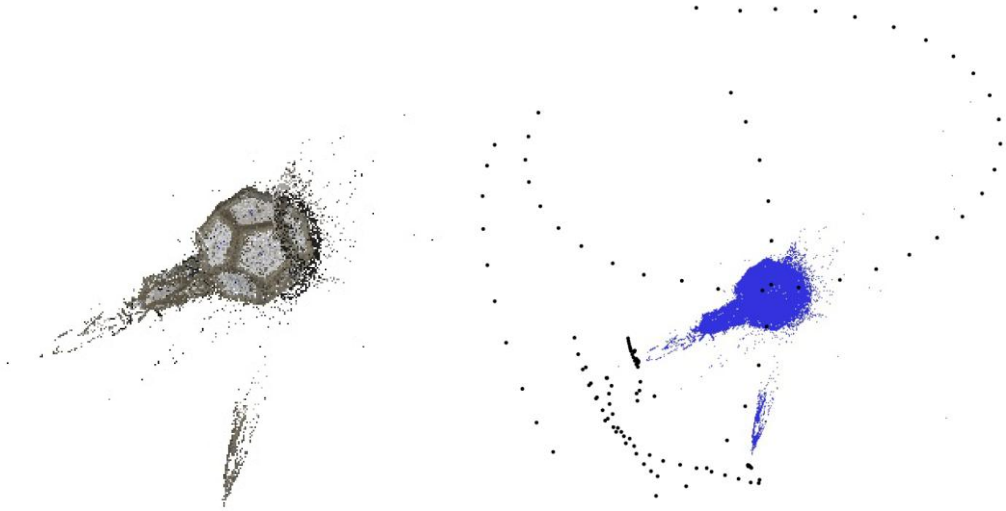

Figure 6.2 VIS point cloud of the dimensional reference (left) and a map of recognized camera positions, in black, and image overlap, in blue (right).

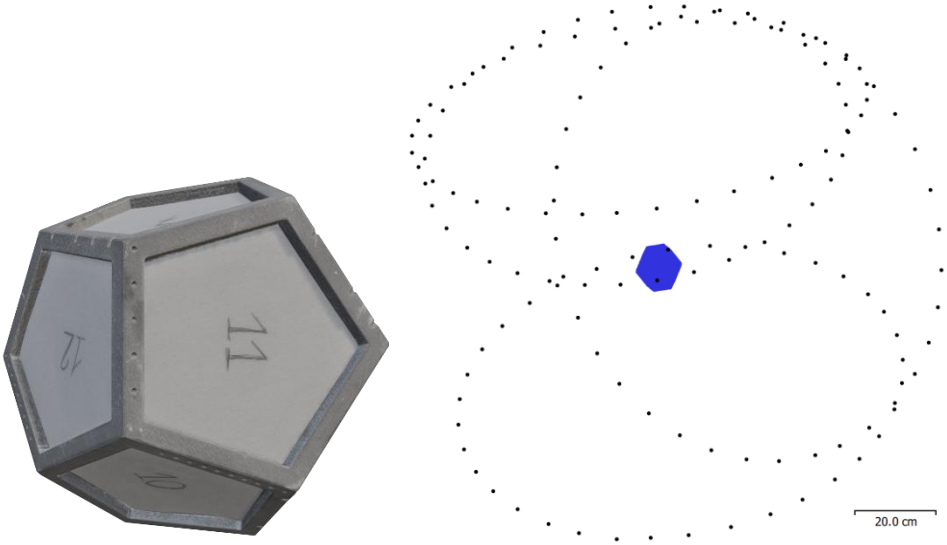

Figure 6.3 Final UVR-3D model of the dimensional reference (left) and map of recognized camera positions, in black, and image overlap, in blue (right).

A more detailed comparison among the photogrammetric 3D models reconstructed from each spectral band, aimed at assessing possible differences in geometric reconstruction, was carried out on the wooden and painted samples. The corresponding results are presented in Section 7.1.3.

Figure 6.2 and 6.3 present the final 3D reconstructions obtained from the VIS and UVR bands, respectively. The models were processed using Agisoft Metashape Professional, version 2.2.0. In the visible band, the insufficient number of keypoints prevented accurate camera pose estimation, thereby compromising the spatial definition of the reconstructed point cloud. Of the 144 images acquired, only 134 were successfully aligned with assigned camera positions. As illustrated in Figure 6.2, many of these positions were inaccurately estimated, further degrading the quality of the reconstruction.

The mean reprojection error for the visible-light model was 6.9 pixels, with a maximum reprojection error of up to 400 pixels, indicating a significant deviation between the projected image points and their observed positions, and thus a low level of geometric accuracy.

Conversely, in the UVR band, the software successfully recognized and aligned all 144 images, achieving a notably low mean reprojection error of 0.4 pixels. In Table 6.2 the Metashape processing parameters, for VIS and UVR 3D reconstruction, are presented. The accurate camera pose estimation enabled the generation of a dense point cloud of 7,950,253 points and the subsequent reconstruction of a mesh consisting of 6,564,818 faces and 3,282,413 vertices. In Figure 6.4 the final UVR-3D model of the dimensional reference is shown.

Although a direct comparison of the models acquired in different spectral bands was not feasible, the results demonstrate that, depending on the object's geometry and material properties, the visible spectrum (valid for both VIS and UVL), is not necessarily optimal for digital replication. In this study, the inherent characteristics of the UVR reflectography were critical to successful image matching. Specifically, the UV reflectography improved the capture of surface features related to the resin composition of the dodecahedron and the paper covering the pentagonal faces, thereby facilitating a robust 3D reconstruction.

Table 6.2 Processing parameters of the VIS and UVR 3D model reconstruction of the dimensional reference.

Parameter	VIS	UVR
Number of Images	144	144
Aligned images	134	144
Camera stations	134	144
GSD (mm/pix)	-	0.0435
Reprojection error (pix)	6.904	0.404
Max reprojection error (pix)	400	32.353
Faces	-	6,564,818
Vertices	-	3,282,413
Points	-	7,950,253

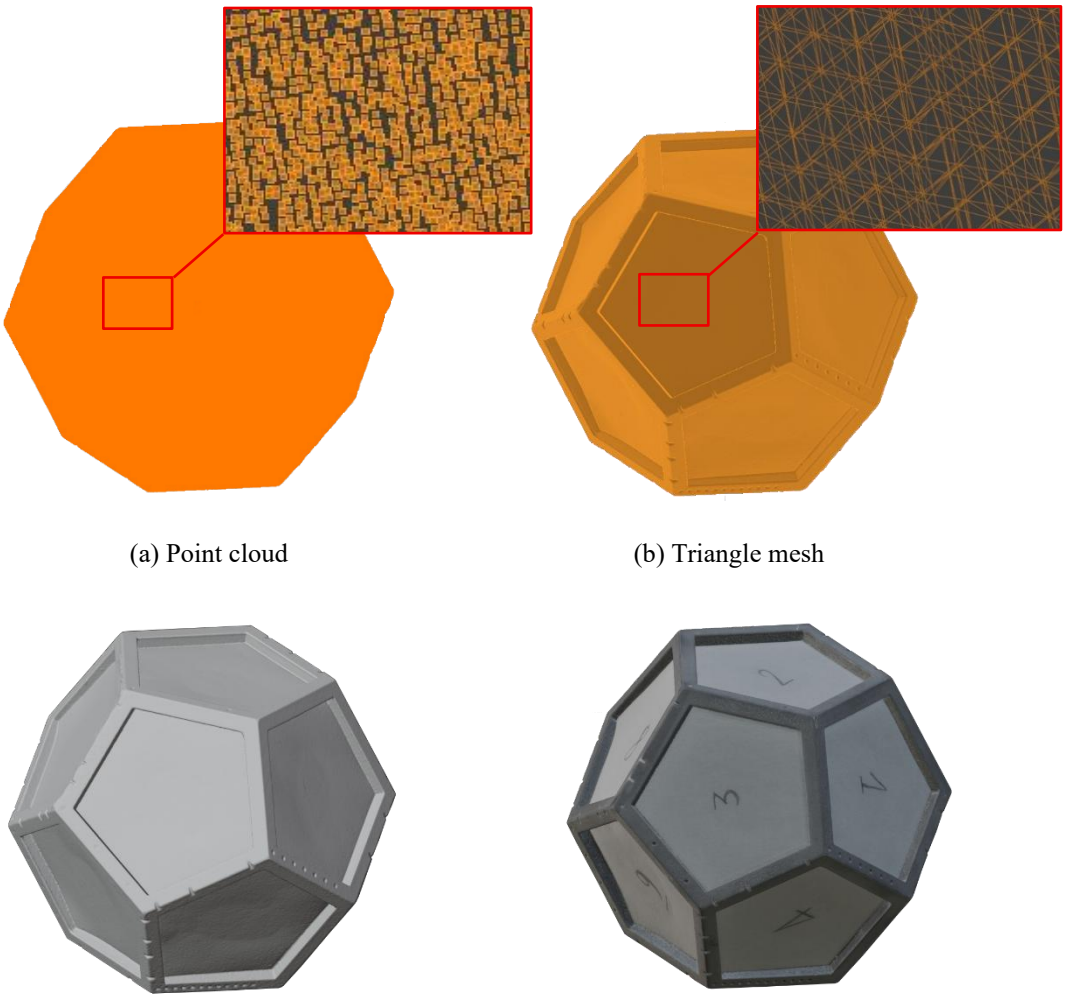

(a) Point cloud (b) Triangle mesh

(c) Untextured mesh (d) Textured 3D model

Figure 6.4 Results of the several processing steps due to the reconstruction of the 3D model of the dimensional reference in Metashape.

6.3 Coordinate Measuring Machine

A Coordinate Measuring Machine (CMM) is a high-precision instrument used to determine the geometry of an object by the contact of a probe with the surface. The position of the probe tip is recorded in 3D space relative to a reference origin, allowing accurate dimensional measurements.

In this study, a contact CMM was employed to generate a reference dataset for comparison with photogrammetric data. The instrument used was the Leitz PMM-C 12.10.7, located at the Istituto Nazionale di Ricerca Metrologica (INRIM) in Turin, Italy. The probing system was composed of three styli mounted at 90° angles, each equipped with a ruby sphere of 5 mm nominal diameter. This setup enabled

access to all surfaces of the object by translating the probe along the X, Y, and Z axes.

Before measurement, each stylus was calibrated using a certified ceramic reference sphere of known dimensions. The dimensional reference under examination was fixed to a metal support and secured on the CMM worktable to ensure stability throughout data acquisition. The complete setup, including the CMM, the dimensional reference, the probe assembly, and the calibration sphere, is shown in Figure 6.5.

Figure 6.5 3D reconstruction of the dimensional reference generated using a Python script based on CMM data. The estimated vertices of the dodecahedron are shown in blue, and the raw measurement are displayed in green. Adapted from [101].

Data acquisition involved measuring ten points on each face of a dodecahedral dimensional reference, with points distributed along the edges of each face. A total of 120 raw points were collected. Using a custom Python script, a best-fit plane was computed for each face. Vertex coordinates were then derived by calculating the intersection of three adjacent planes. Subsequently, the edge lengths were computed as distances between these reconstructed vertices. The final 3D reconstruction of the dodecahedron, based on this procedure, is illustrated in Figure 6.6. It is important to note that this method involves indirect vertex measurement. This approach was selected due to the challenges associated with directly probing the vertices using a contact stylus.

Because the measurement process involves physical contact with the reference's surface, the probe itself may cause minor surface deformation, especially considering the low mechanical strength of the dodecahedron resin. Furthermore, the thermal expansion properties of the resin itself and the inherent

uncertainties of the 3D printing process must be considered in the overall uncertainty analysis.

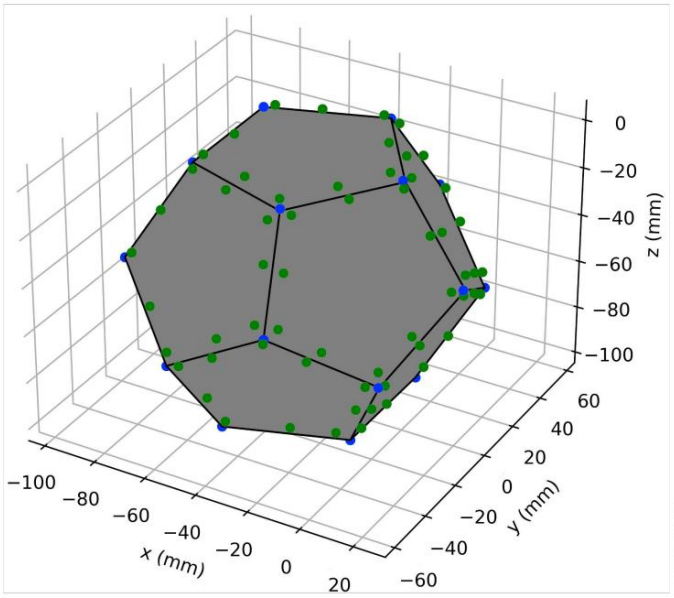

Figure 6.6 3D reconstruction of the dimensional reference generated using a Python script based on CMM data. The estimated vertices of the dodecahedron are shown in blue, and the raw measurement are displayed in green. Adapted from [101].

To evaluate measurement repeatability, several measurements were conducted on the top face of the object. The residuals from the best-fit plane showed a standard deviation in the order of 50 µm, which represents the expected measurement uncertainty. Given that the manufacturer's declared accuracy of the CMM is in the micrometer range, its contribution to the overall uncertainty, considering that the dimensional variations considered in this study are of a larger magnitude, can be considered negligible.

For comparison purposes, the same edge lengths were also measured on the 3D models generated by photogrammetry, using the point picking tool of the open-source software CloudCompare, version 2.14.alpha. Specifically, that measurements acquired on the photogrammetric model were obtained through manual point selection. For this reason, it is not possible to quantify the actual uncertainty of the measurements associated with the photogrammetric data. Instead, the purpose of this comparison is to assess the accuracy of the measurements obtained from the photogrammetric model by comparing them to those acquired with the selected reference systems, namely the CMM and laser scanning.

The photogrammetric models were scaled using reference targets placed at known distances within the scene and fixed on a rotating platform, as described in the Section 5.4. For this reason, no additional scaling operations were required during the measurement process.

Table 6.3 reports the edge lengths obtained using both the photogrammetric and CMM measurement techniques. The results show that all measured edges, whether

derived from the CMM or photogrammetric models, are about 44 mm. In the case of photogrammetry, the close match of the average edge lengths confirms the effectiveness of the scaling procedure.

Table 6.3 Analysis of experimental data comparing edge lengths of the dimensional reference measured by the CMM and photogrammetry.

Edge	CMM Length (mm)	PG Length (mm)	Error (mm)	Relative Error (%)
1	44.00	43.61	0.39	0.89
2	43.86	43.41	0.45	1.03
3	43.94	43.71	0.23	0.52
4	43.93	43.82	0.11	0.25
5	43.91	43.78	0.13	0.30
6	43.99	43.59	0.40	0.91
7	43.95	43.53	0.42	0.96
8	43.96	43.51	0.45	1.02
9	43.95	43.74	0.21	0.48
10	43.94	43.64	0.30	0.68
11	43.86	43.76	0.10	0.23
12	43.89	43.54	0.35	0.80
13	43.91	43.51	0.40	0.91
14	43.92	43.60	0.32	0.73
15	43.85	43.59	0.26	0.59
16	43.93	43.59	0.34	0.77
17	43.82	43.46	0.36	0.82
18	43.91	43.60	0.31	0.71
19	43.91	46.89	0.02	0.05
20	43.88	43.80	0.08	0.18
21	43.66	43.37	0.29	0.66
22	43.55	43.56	-0.01	-0.02
23	43.63	43.40	0.23	0.53
24	43.80	43.87	-0.07	-0.16
25	43.78	43.56	0.22	0.50
26	43.92	43.61	0.31	0.71
27	43.94	43.91	0.03	0.07
28	43.95	43.79	0.16	0.36
29	43.91	43.58	0.33	0.75
30	43.92	43.57	0.35	0.80
Average	**43.88**	**43.63**	**0.25**	**0.57%**
Std	**0.10**	**0.15**	**0.14**	**0.33%**
Max	**44.00**	**43.91**	**0.45**	**1.03%**

The standard deviation of the measurements obtained with the CMM is approximately 100 µm, consistent with the uncertainty associated with plane fitting. The photogrammetric model shows a standard deviation of 150 µm, less than twice the CMM value. Nonetheless, these results are particularly significant when considering the differences in equipment cost: approximately $1,500 USD for the photogrammetry setup, and over $225,000 USD for the CMM. The maximum absolute difference between corresponding edge lengths measured by the CMM and the photogrammetric model is approximately 0.45 mm, with a maximum relative error of about 1% (edge #8) and an average relative error of roughly 0.6%. These results indicate that the photogrammetric setup presented provides reliable dimensional measurements, confirming its suitability for monitoring deformation in wooden artifacts subjected to artificial aging.

6.4 Laser Scanning

To create a virtual 3D replica of the dimensional reference, a FARO Laser ScanArm Edge (FARO Technologies, Inc., Florida, US) [102], represented in Figure 6.7, was used. Measurements were carried out in collaboration with the National Technical University of Athens (NTUA, Greece), at the Department of Rural, Surveying and Geoinformatics Engineering (SRSE, Greece) laboratory.

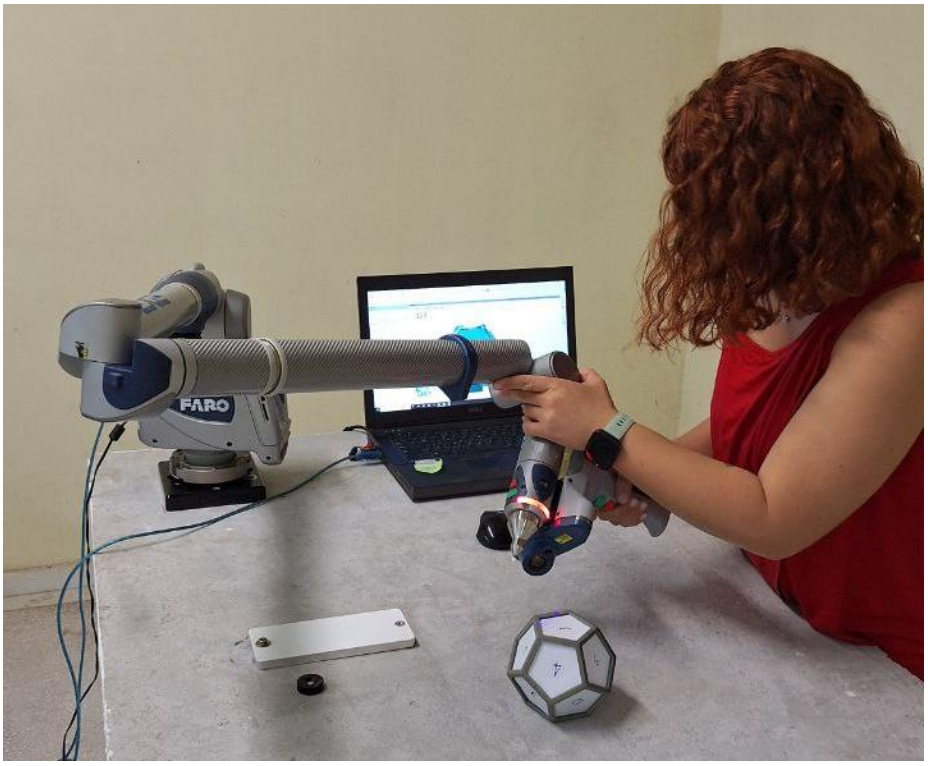

Figure 6.7 FARO Laser ScanArm Edge during the acquisition of the dimensional reference.

The system consists of a portable Coordinate Measuring Arm (CMA) equipped with a laser scanner. Specifically, the laser scanner is integrated with a FARO

VANTAGE Laser Tracker (FARO Technologies, Inc., Florida, US). The system is composed of a 7-axis articulated arm, mounted on a plate fixed to a levelled concrete worktable to ensure stability. Each joint is equipped with a rotary optical encoder, and the acquired signals are processed using error compensation algorithms and temperature correction models.

The laser scanner operates using the triangulation principle and employs a light-stripe projection method, emitting a horizontal beam at 450 nm wavelength. The reflected light is captured by a CMOS sensor, and 3D coordinates are calculated by triangulation. The instrument's single point error is 0.029 mm, and the volumetric error is ± 0.041 mm.

Before data acquisition, environmental conditions were verified to satisfy some operating specifications: the instrument ensures accurate results in a temperature range between 0°C and 45°C, and relative humidity up to 95%. During scanning, the distance between the scanner and the object was kept as constant as possible. Moreover, the instrument automatically identifies the optimal scanning distance and provides visual feedback by a LED indicator on the handle, which changes color from green (optimal) to red (unsuitable) [103].

As the laser tracker and laser scanner are integrated, both tools must be calibrated. Therefore, after a 30-minute warm-up period, probe compensation and LLP (Line Laser Probe) compensation were performed. Probe compensation was carried out using a sphere of unknown diameter, while LLP compensation used a white calibration plate. After measuring 14 points on the plate with the probe and scanning it in five orientations, the resulting compensation error was 0.035 mm.

The LLP has a measurement accuracy of ± 0.054 mm, captures 2000 points per line, and features a line-to-line distance of 0.040 mm. Multiple scanning directions were used due to the surface roughness of the resin. The dimensional reference was scanned in four orientations to ensure complete coverage. Each side was scanned separately, and the final point cloud was obtained by registration using the ICP (Iterative Closest Point) algorithm. Registration error was negligible due to the high overlap between point clouds.

After scanning, noise removal was performed to delete points located on the worktable or isolated from the main point cloud. At the end of the process, the final point cloud contains 12,600,290 points.

The surface and the overall geometry were accurately reconstructed, with minor exceptions. Specifically, the undercuts defining the pentagonal faces of the dodecahedron were only partially detected, resulting in sparse or missing data in those areas. This is due to the object's shape and the material properties, but it didn't affect the measurement of the edges, which are used for the comparison with measurements acquired on the photogrammetric 3D model. To improve laser scanning performance, the pentagonal surfaces were covered with white paper to enhance light reflection and ensure proper acquisition.

The 30 edges lengths of the model obtained by laser scanning were evaluated directly on the point cloud, measured as distances between selected points using the open-source software CloudCompare, by the point picking tool [104]. Similar to the photogrammetric model, the measurements from the laser scanning were

obtained by manual point selection. Therefore, it is not possible to quantify the measurement uncertainty. The results are reported in Table 6.4, showing edge lengths and their comparison with those obtained via photogrammetry.

Table 6.4 Analysis of experimental data comparing edge lengths of the dimensional reference measured by the photogrammetry and laser scanner.

Edge	PG Length (mm)	LS Length (mm)	PG – LS (mm)	Relative Error (%)
1	43.61	43.79	-0.18	-0.41
2	43.41	43.81	-0.40	-0.92
3	43.71	43.63	0.08	0.18
4	43.82	43.70	0.12	0.27
5	43.78	43.68	0.10	0.23
6	43.59	43.71	-0.12	-0.28
7	43.53	43.55	-0.02	-0.05
8	43.51	43.54	-0.03	-0.07
9	43.74	43.88	-0.14	-0.32
10	43.64	43.95	-0.31	-0.71
11	43.76	43.52	0.24	0.55
12	43.54	43.46	0.08	0.18
13	43.51	43.65	-0.14	-0.32
14	43.60	43.81	-0.21	-0.48
15	43.59	43.59	-	-
16	43.59	43.72	-0.13	-0.30
17	43.46	43.90	-0.44	-1.01
18	43.60	43.70	-0.10	-0.23
19	43.89	43.82	0.07	0.16
20	43.80	43.69	0.11	0.25
21	43.37	43.60	-0.23	-0.53
22	43.56	43.58	-0.02	-0.05
23	43.40	43.68	-0.28	-0.65
24	43.87	43.71	0.16	0.36
25	43.56	43.62	-0.06	-0.14
26	43.61	43.61	-	-
27	43.91	43.87	0.04	0.09
28	43.79	43.80	-0.01	-0.02
29	43.58	43.63	-0.05	-0.11
30	43.57	43.90	-0.33	-0.76
Average	**43.63**	**43.7**	**-0.07**	**-0.17%**
Std	**0.15**	**0.13**	**0.17**	**0.39%**
Max	**43.91**	**43.95**	**-0.44**	**-0.92%**

The results show that the edge lengths measured with both the laser scanner and photogrammetry are very close to the nominal dimension of 44 mm, with an average difference of 73 µm. The standard deviation of the measurements on the laser scanner point cloud is approximately 130 µm, which is slightly lower than that of the photogrammetric point cloud.

The maximum deviation between the two methods is -0.44 mm, corresponding to a maximum relative error of approximately -0.92% (edge #2). This discrepancy can be explained by observing the point clouds in Figure 6.8, where it is clearly visible that certain features, such as the undercuts, were not correctly reconstructed in the laser scanner dataset.

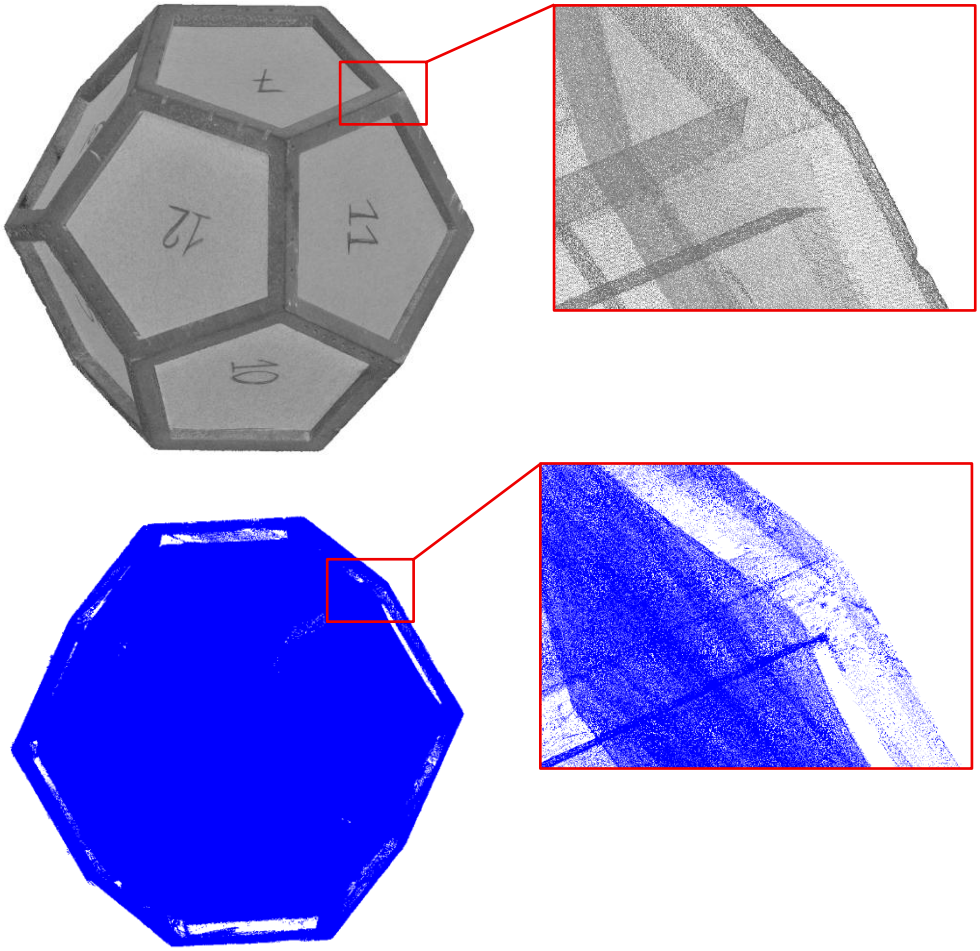

Figure 6.8 Final point cloud obtained by photogrammetry from the UV reflectography dataset (above) and by laser scanner (below). The red rectangles highlight details of the point density for each cloud.

Another comparison was carried out between the photogrammetric point cloud acquired in the UVR band and the one obtained with the laser scanner. The photogrammetric point cloud consists of 7,950,253 points, slightly more than half of the laser scanner cloud, which contains 12,600,290 points. The comparison was performed using CloudCompare, processing and analyzing 3D data, which enables

the calculation of distances between two meshes, two point clouds, or between a point cloud and a mesh.

For this analysis, the cloud-to-mesh distance between the laser scanned and the photogrammetric model was computed without any further scaling adjustment. Before distance calculation, the two models of each sample were preliminarily registered based on their geometric features. Corresponding surface points were manually selected to register the models in a common coordinate system. Since the photogrammetric workflow allows for model scaling through reference targets placed in the scene, this phase did not require any additional scaling. The registration was performed using the scanned model as the reference. After this first manual registration, a refined one was performed using the ICP algorithm. This algorithm iteratively minimizes the distances between datasets to optimize correspondence with the reference model. The process continues until optimal alignment is reached, and approaches a theoretical 100% overlap between the surfaces. In this case, ICP registration yielded a root mean square (RMS) error of 0.963615, calculated over 50,000 points.

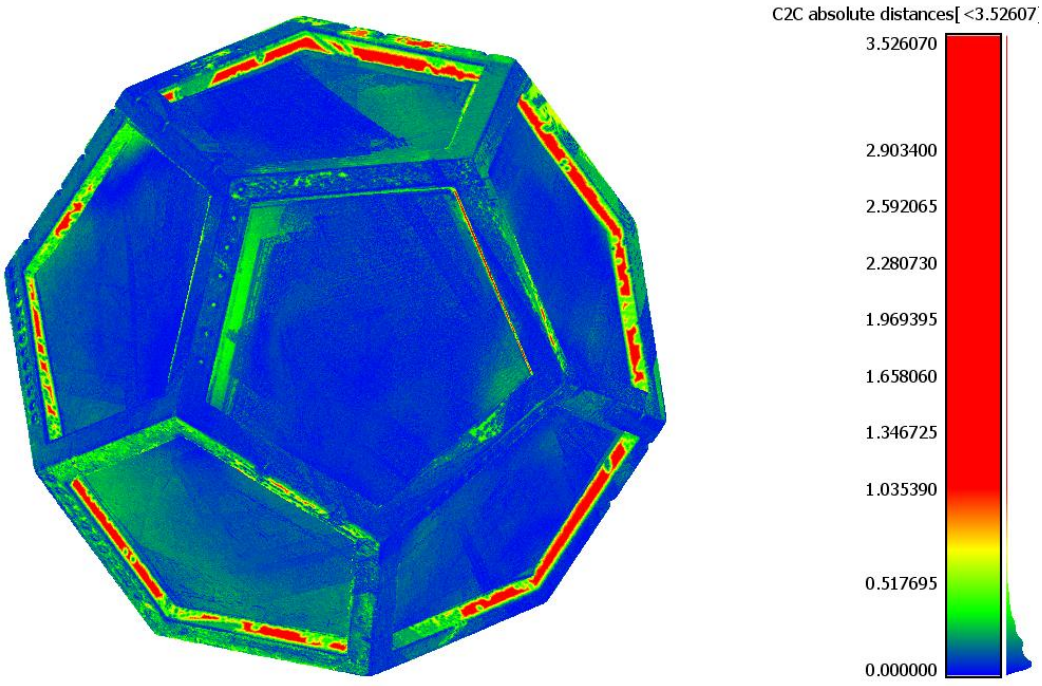

Figure 6.9 Cloud-to-cloud absolute distances map computed in CloudCompare between the point clouds of the dimensional reference acquired by laser scanning and photogrammetry.

The results are shown in Figure 6.9, which includes a color-coded distance map indicating the spatial absolute distances between the point clouds. In particular, when comparing two point clouds, CloudCompare provides only absolute positive distances (C2C absolute distances). However, when at least one mesh is involved, the comparison can include both positive and negative distance values, yelding to relative distances. Once the models were registered, the absolute distances between corresponding points were computed, providing values for the mean distance,

standard deviation, and RMS error. The mean distance indicates the average deviation between the two surfaces. The standard deviation quantifies the distribution of these deviations, indicating how consistent the differences are across the surface. The RMS error offers a global measure of the discrepancy between the models, taking into account both the magnitude and direction of the deviations. The results are visualized using a scalar field mapped onto the surface of the model, where color gradients represent the distribution and magnitude of the detected shape distances.

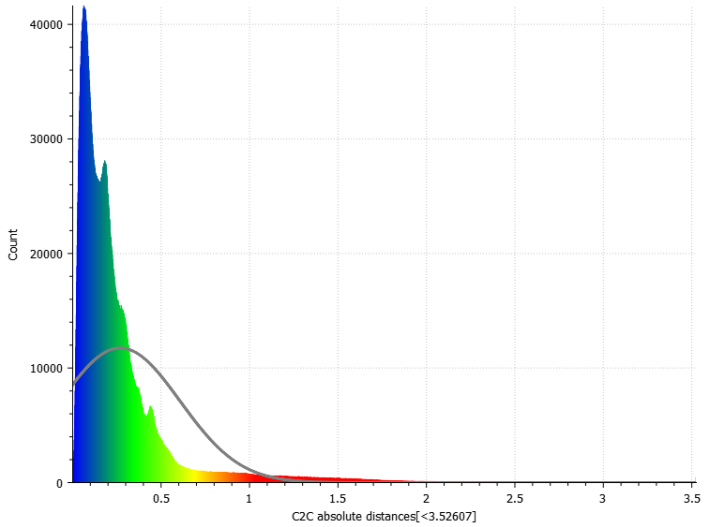

Figure 6.10 Histogram of computed absolute distances (mm) extracted in CloudCompare from the cloud-to-cloud comparison between the photogrammetric and scanned acquisition of the dimensional reference.

The generated absolute distance map highlights areas with minimal deviation between the point clouds in blue, corresponding to values close to zero. Larger deviations are shown in green and red and are mainly associated with the cloud acquired using the laser scanner. As previously noted, the scanned cloud is less dense in certain detailed regions of the dodecahedron, particularly around the undercuts. This affects both the standard deviation, equal to 0.337524, and the mean peak value of 0.269691, as shown in the histogram in Figure 6.10. Overall, the maximum absolute deviation recorded is approximately 3.5 mm.

Chapter 7

Results and Discussion

This chapter presents the results of the deformation monitoring performed on the two reference wooden samples. Both specimens were acquired before and after aging using two techniques: photogrammetry and laser scanning. The resulting 3D models were analyzed and compared through the following approaches:

- *Photogrammetric models*
    - Performance evaluation of 3D reconstruction software: Meshroom and Metashape
    - Generation of multi-band 3D models
    - Comparison of the models recorded in the different spectral ranges (VIS, VIS PL, UVL, UVR, and IRR)
    - Comparison of pre- and post-aging models for both samples
- *Laser scanning models*
    - Comparison of pre- and post-aging acquisitions for both samples
- *Cross-techniques comparison*
    - Comparison between photogrammetric and laser-scanned models acquired before the aging process

7.1 Photogrammetric models

7.1.1 3D reconstruction Software comparison

This section presents a comparative assessment of the performance of two photogrammetric software platforms, Meshroom and Metashape**,** in the 3D reconstruction of the wooden and painted wooden samples. This comparison aims to justify the selection of the software used in this study. Detailed information regarding the image acquisition procedures is described in Section 7.1.2. The technical specifications of both software platforms are described in Section 5.5.

Meshroom, an open-source software, was initially considered due to its accessibility. However, despite multiple attempts, the reconstructions generated from each of the multi-band technique considered by Meshroom were unsatisfactory. This was especially true for the wooden sample. During the image-matching phase, configured with high Describer Density, the software failed to effectively detect and match features on the surface of the sample.

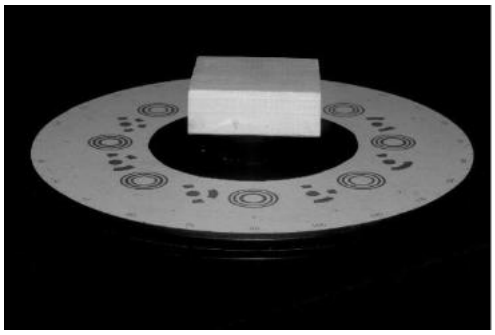

(a) Image

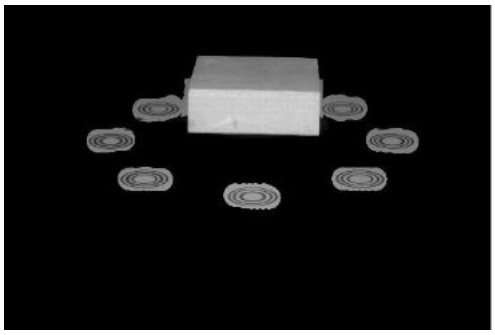

(b) Masked image

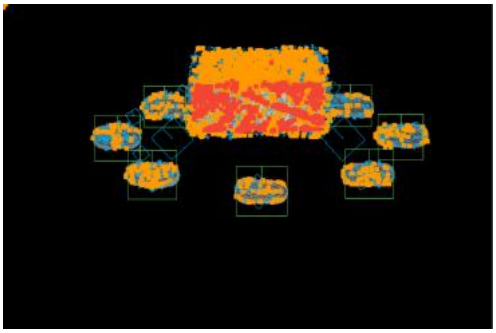

(c) Image matching

Figure 7.1 Representation of one of the IRR images used for the 3D reconstruction of the wood sample by Meshroom: (a) an image, (b) a masked image, and (c) details of the features (light blue dots), the image matches (orange dots) detected after the alignment process (red dots), and marker's detection (green squares).

Since an insufficient number of image matches could be detected in most of the analyzed spectral bands, except for the VIS and IRR, only these two were considered for further analysis. No significant differences were observed between the VIS and VIS-PL reconstructions; therefore, only the VIS band was retained.

From the acquired images, it is evident that, for each band and for each sample, the sample surface occupies approximately one-sixth of the total image area. As an example,

Figure 7.1a shows one of the images acquired during the IRR setup of the wood sample. The distance between the camera and the object was defined by the focusing limits of the lens, which had to remain in focus during the 360° rotation of the sample. However, this setup caused most of the image area to be occupied by the background and the rotating platform supporting the sample. As a result, feature matches were mostly concentrated outside the area of the samples. To address this issue, image masks were applied to isolate only the regions of interest, namely the sample and the reference markers, as shown in

Figure 7.1b. This approach excluded the surrounding environment from the processing.

Figure 7.1c illustrates the outcome of feature detection and image matching after masking. In this visualization, blue areas indicate detected features, orange areas represent matched points identified in at least two images, and red areas correspond to successfully triangulated points.

The 3D reconstruction of the wood sample obtained through the use of image masks was minimal. In the VIS band, the software was able to recognize only 4 out of 72 camera positions, which was insufficient for creating a complete or reliable 3D model. Interestingly, slightly improved results were obtained using the IRR images. Meshroom identified 36 camera positions, i.e. 50% of the total. Although this still did not produce a reliable 3D reconstruction, the best performance was noted in a non-visible multi-band. Section 7.1.3, presents a more detailed analysis of multi-band influence on 3D accuracy.

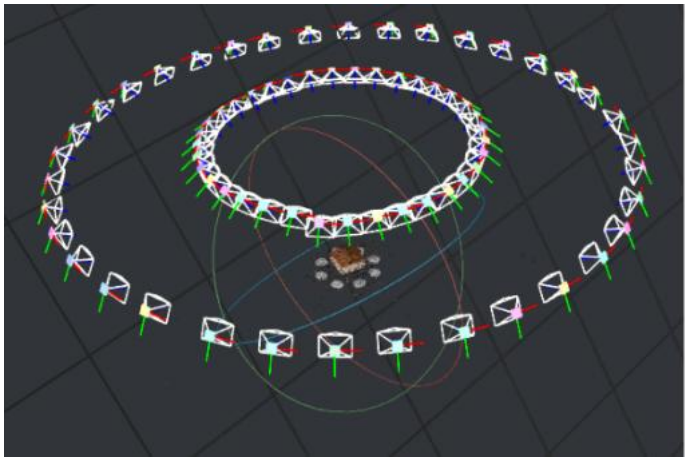

Figure 7.2 Camera positions detected by Meshroom for the painted sample 3D model reconstructed by masked VIS acquisitions.

For the painted sample, using VIS masked images Meshroom, was able to complete the 3D reconstruction pipeline and successfully identify all 72 camera positions (Figure 7.2). However, the final model showed limited detail and mesh density. The total number of mesh faces, including the acquisition platform and markers, was 642,583. In contrast, the equivalent model reconstructed using Metashape, after post-processing and removal of the outliers, consisted of 1,268,791 faces, nearly twice as Meshroom, with noticeably higher detail.

In the case of the IRR reconstruction, the application of image masks did not yield a sufficient number of image correspondences to enable the generation of the 3D model.

Due to the limited reconstruction capabilities and the reduced model quality achieved with Meshroom, the software selected for the 3D reconstruction of the models was Metashape. A more detailed analysis of the models reconstructed by Metashape is provided in the following sections.

7.1.2 Multi-band 3D models

This section presents the results obtained from the reconstruction of 3D models of two samples, acquired both before and after the aging process. The models were generated using a combination of multi-band imaging and photogrammetry. Each 3D reconstruction integrates data acquired from several multi-band imaging techniques. In particular, the imaging techniques used include VIS-reflected imaging, polarized VIS-reflected imaging, IR-reflected imaging, and UV-reflected imaging, UV-induced luminescence imaging was applied exclusively to the painted sample to assess the surface distribution of added materials, since no luminescence was detected on the wooden sample. Furthermore, false-color processing was applied to produce IR-reflected false-color and UV-reflected false-color images. The summary of all the acquisitions performed is illustrated in Figure 7.3.

All images were acquired using the setup described in Chapter 5. The acquisition parameters, summarized in Table 7.1, refer to Epoch 0 and Epoch 1, corresponding to the images acquired before and after the aging process, respectively, and were kept constant throughout the data collection. Among the reported acquisition parameters, the ISO values were set to a notably higher value for the UVL and UVR bands. Although this adjustment increased digital noise, a sensitivity well above the native value was selected to reduce the shutter speed and facilitate the acquisition process. Nevertheless, the UVL and UVR bands still required the longest shutter speeds due to their inherently low emitted signal.

To ensure complete coverage of the sample surfaces, each sample was acquired in two different orientations: one with the camera tilted at 45° and another with the camera tilted at 30°. Images were captured at 10° horizontal intervals, yielding a total of 72 images for each multi-band imaging technique.

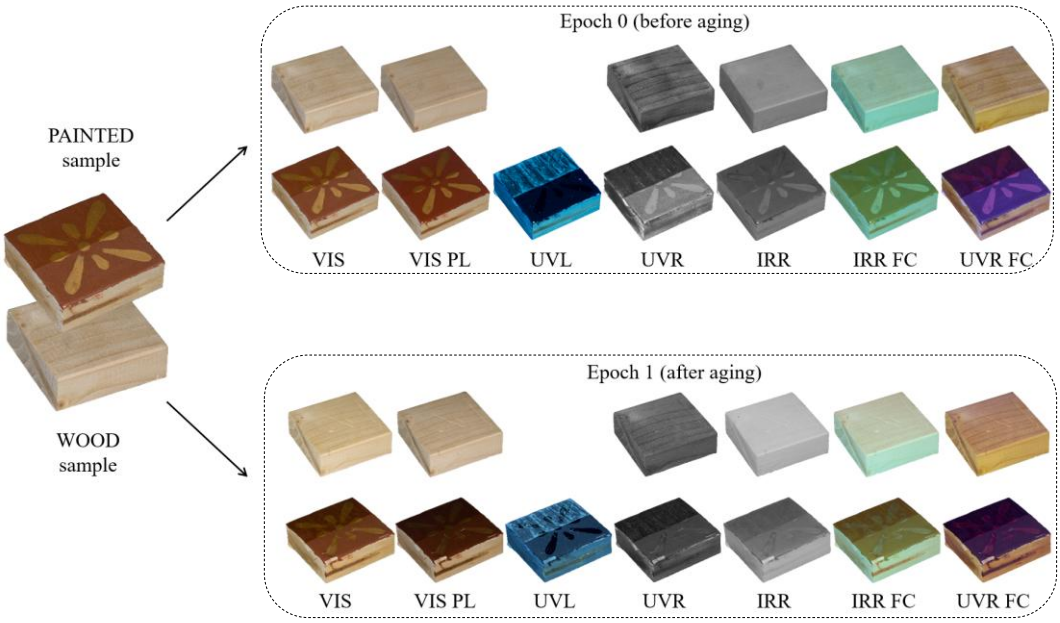

Figure 7.3 Representative scheme of all acquisitions performed in the different spectral bands, for both the wood and painted samples, before (Epoch 0) and after (Epoch 1) the aging process.

It should be noted that, to optimize the acquisition process, the bottom of each sample, namely the face in direct contact with the rotating platform, was not acquired. As a result, only five out of the six faces were photographed for each sample. The reconstruction of the 3D models was performed using the photogrammetric pipeline embedded in Metashape, as described in Section 5.5.2. Then, the models were scaled using the reference markers as outlined in Section 5.4.

Table 7.1 Parameters used during image acquisition.

WOOD																
	Before aging (Epoch 0)								After aging (Epoch 1)							
Parameter	Value								Value							
	VIS		**VIS PL**		**UVR**		**IRR**		**VIS**		**VIS PL**		**UVR**		**IRR**	
Camera Tilt (°)	45	30	45	30	45	30	45	30	45	30	45	30	45	30	45	30
Shutter Speed (s)	3	6.5	4	8	15	30	1.5	2.5	10	10	10	10	15	15	2.5	2
N° of Acquired Images	72 (36x2)		72 (36x2)		72 (36x2)		72 (36x2)		72 (36x2)		72 (36x2)		72 (36x2)		72 (36x2)	
ISO	80		80		800		80		80		80		800		80	
Image Size (pixels)	6240x4160								6240x4160							
Image Format	RAF								RAF							
Focal Length	50 mm								50 mm							
Aperture	f/16								f/16							
Horizontal Step Angle	10°								10°							
Camera-object distance	~48 cm and ~52 cm								~48 cm and ~52 cm							

PAINTED																				
	Before aging (Epoch 0)										After aging (Epoch 1)									
Parameter	Value										Value									
	VIS		**VIS PL**		**UVL**		**UVR**		**IRR**		**VIS**		**VIS PL**		**UVL**		**UVR**		**IRR**	
Camera Tilt (°)	45	30	45	30	45	30	45	30	45	30	45	30	45	30	45	30	45	30	45	30
Shutter Speed (s)	8	10	10	13	30	30	30	15	4	1.5	8	10	8	10	20	20	15	13	2	2
N° of Acquired Images	72 (36x2)		72 (36x2)		72 (36x2)		72 (36x2)		72 (36x2)		72 (36x2)		72 (36x2)		72 (36x2)		72 (36x2)		72 (36x2)	
ISO	80		80		800		800		80		80		80		800		800		80	
Image Size (pixels)	6240x4160										6240x4160									
Image Format	RAF										RAF									
Focal Length	50 mm										50 mm									
Aperture	f/16										f/16									
Horizontal Step Angle	10°										10°									
Camera-object distance	~32 cm and 43 cm										~32 cm and ~43 cm									

Table 7.2 Metashape processing parameters and results.

	WOOD		PAINTED	
	Epoch 0	**Epoch 1**	**Epoch 0**	**Epoch 1**
Parameter	**Value**		**Value**	
Number of Images	72	72	72	72
Aligned images	72	72	72	72
Camera stations	72	72	72	72
GSD (mm/pix)	0.0448	0.0303	0.0315	0.0300
Reprojection error (pix)	0.661	0.334	0.350	0.403
Max reprojection error (pix)	15.123	2.341	2.668	4.205
Faces	910,972	1,410,255	1,268,791	1,489,792
Vertices	456,558	706,363	635,515	746,183

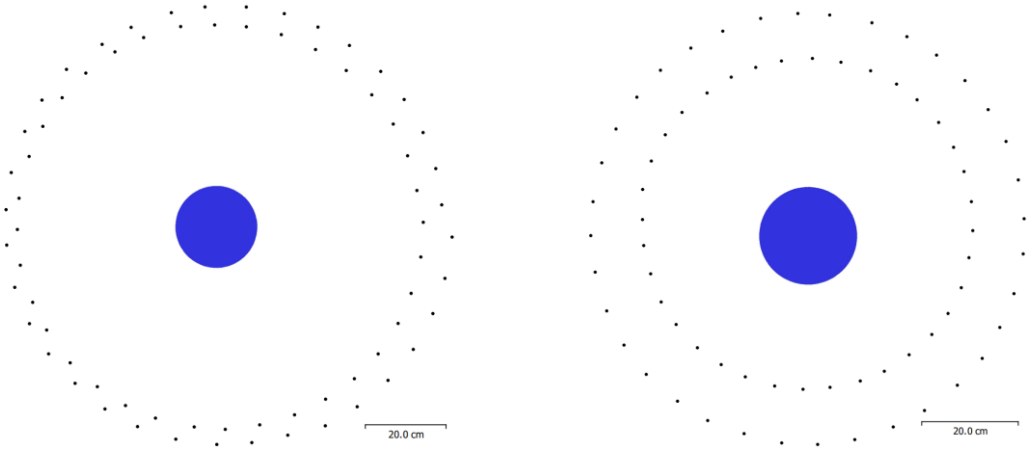

(a) Wood sample at Epoch 0 (b) Painted sample at Epoch 0

Figure 7.4 Black dots are representative of the camera locations of the wood sample (a) and the painted sample (b) before the aging process. In blue, the virtual reconstruction of the acquired objects, located on the platform used for the acquisition setup is presented.

Figure 7.4 illustrates the distribution of the camera positions, showing two concentric acquisition paths around each sample. Figure 7.5 and Figure 7.6 present the results for the wooden and painted samples, respectively, before the aging process. In particular, Figure 7.5a and Figure 7.6a display the corresponding sparse point clouds. It is important to note that all images were successfully aligned.

Following image alignment, a polygonal mesh is generated (Figure 7.5b and Figure 7.6b). The mesh does not contain realistic color information, as seen in Figure 7.5c and Figure 7.6c. The next step involves the application of the relative texture using the original image data to produce the photorealistic appearance in the 3D model (Figure 7.5d and Figure 7.6d). The result is a textured, multi-band 3D model used as a virtual replica of each sample. The final reconstructions are shown in Figure 7.7, Figure 7.8Figure 7.9, Figure 7.10.

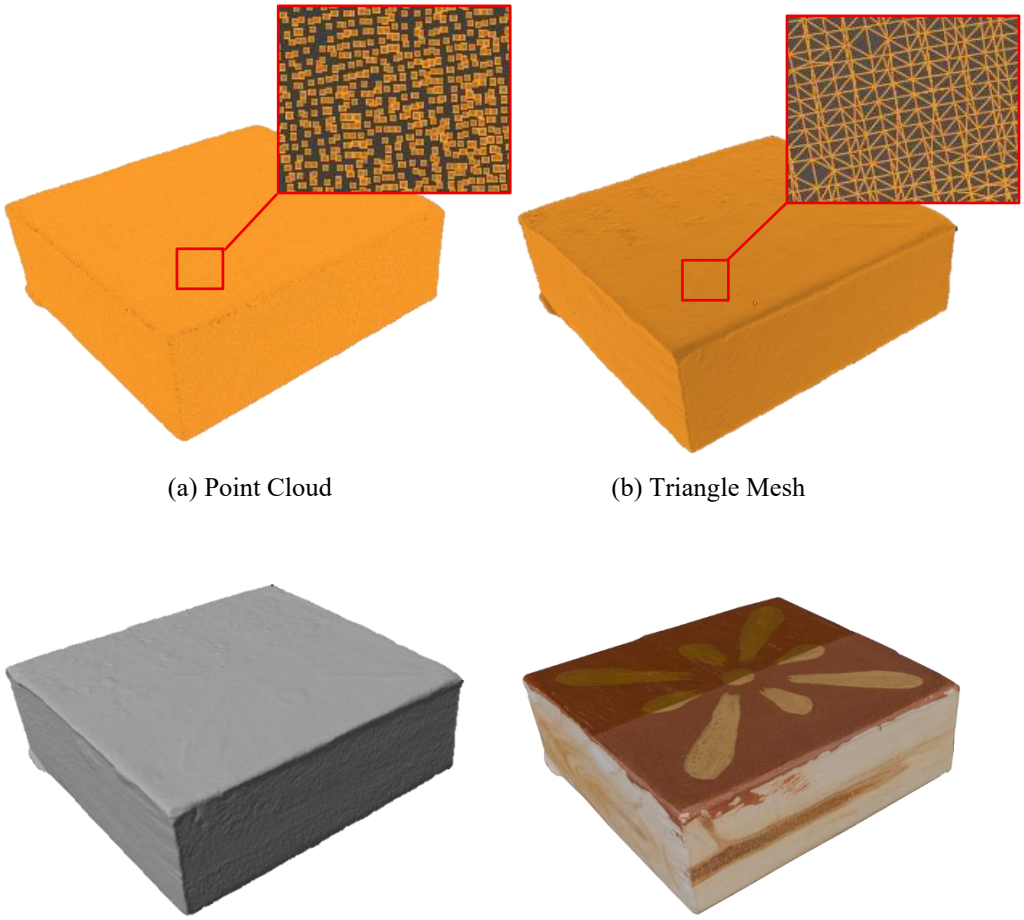

(a) Point Cloud (b) Triangle Mesh

(c) Untextured Mesh (d) Textured 3D model

Figure 7.5 Results of the several processing steps due to the reconstruction of the 3D model of the painted sample before the aging process in Metashape

The image processing parameters used in Metashape for each acquisition are reported in Table 7.2. The number of faces and vertices remained consistent across all models, except for the wood sample acquired before aging, which showed a lower mesh density. This model also displayed higher resolution and reprojection errors. These differences are mainly attributed to a larger camera-to-object distance, imposed by the lens focal length. Due to the small size of the samples, shorter working distances were not feasible, resulting in images where the object occupied only about one-quarter of the frame.

In this context, the use of markers was essential. In addition to their primary role in model scaling, they significantly contributed to image alignment and feature matching. The reduced number of vertices and faces, along with the higher reprojection error and resolution observed in the wood sample before aging, are due to the increased camera-to-object distance. Despite the reflective nature of both sample surfaces, more pronounced in the varnished area of the painted sample, Metashape proved to be effective in reconstructing the geometry of both models.

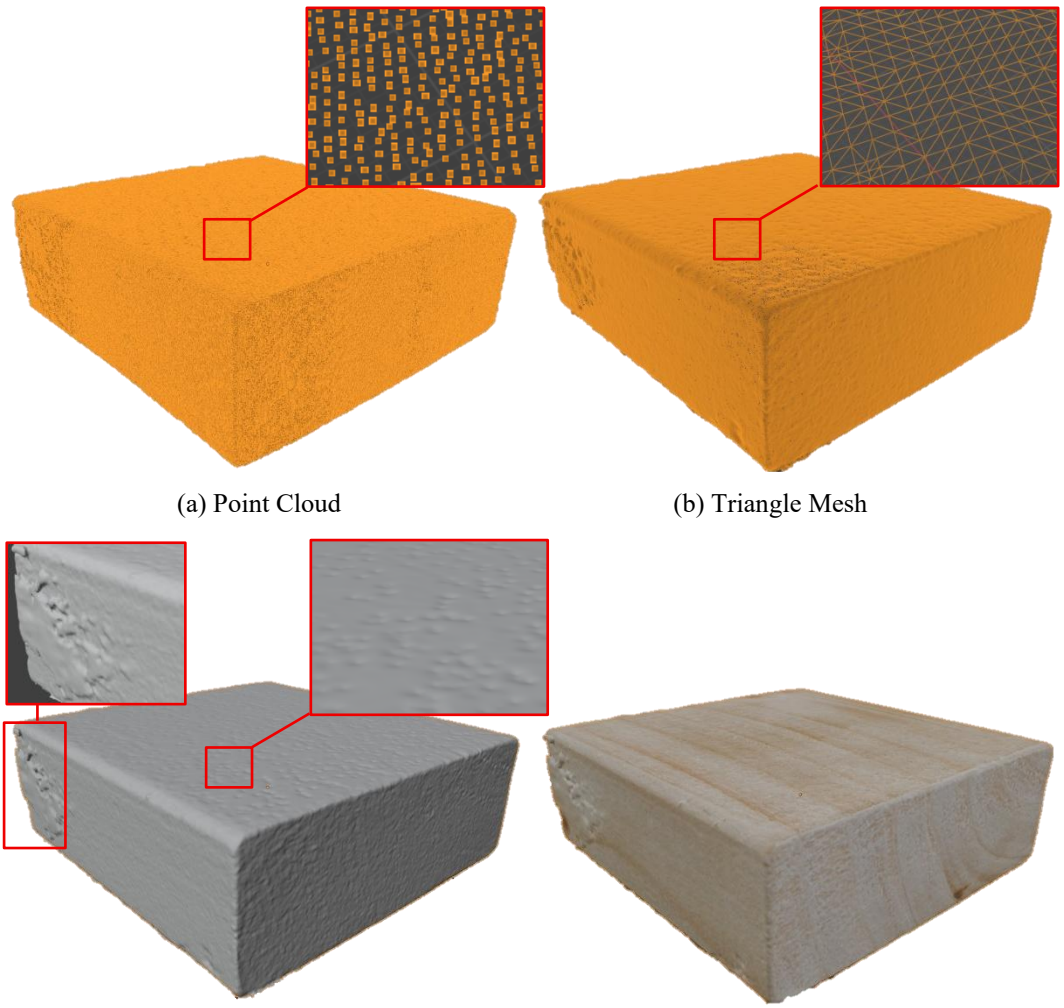

(a) Point Cloud (b) Triangle Mesh

(c) Untextured Mesh (d) Textured 3D model

Figure 7.6 Results of the several processing steps due to the reconstruction of the 3D model of the wood sample before the aging process in Metashape

Although polarized images were acquired in advance to enable the use of the cross-polarization method, this additional step was unnecessary for a successful 3D reconstruction.

Each final mesh was reconstructed starting from the VIS dataset. The spectral information acquired through the other multi-band imaging techniques was subsequently integrated by applying the corresponding textures. The resulting textured models (Figure 7.7, Figure 7.8, Figure 7.9, and Figure 7.10) can be explored as single 3D files. This approach is comparable to traditional 2D multi-band imaging workflows, in which multiple spectral layers are superimposed within software platforms for image manipulation, such as Photoshop or GIMP. This approach to 3D modeling offers valuable support to conservators and researchers by enabling immediate and intuitive access to both geometric and spectral data. The comparison of multiple multi-band textures provides a significantly enhanced understanding of the object's structure. This includes the spatial distribution of preparatory layers, pigments, varnishes, adhesives, and underdrawings, which are

often less immediately readable and interpretable using traditional 2D imaging methods.

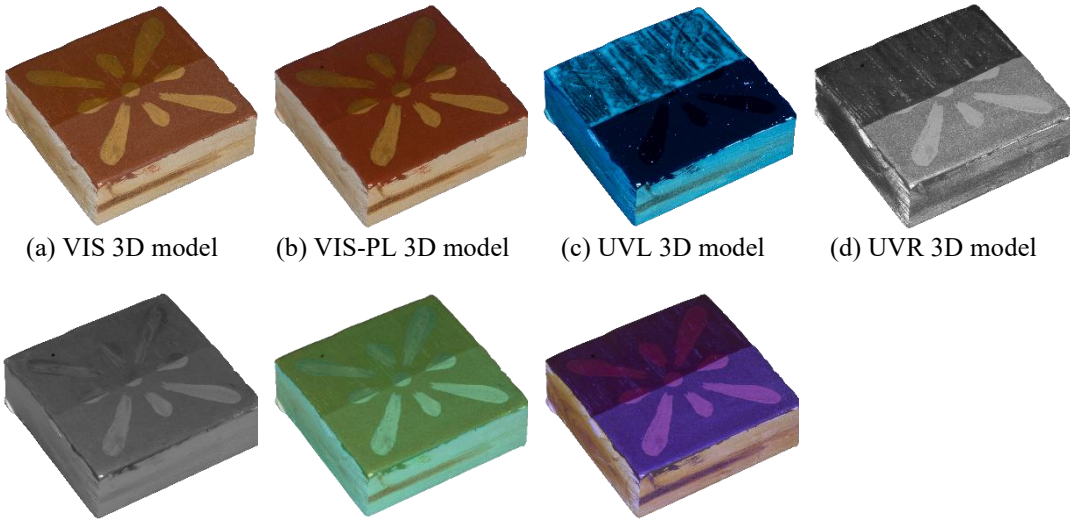

(a) VIS 3D model (b) VIS-PL 3D model (c) UVL 3D model (d) UVR 3D model

(e) IRR 3D model (f) IRR-FC 3D model (g) UVR-FC 3D model

Figure 7.7 Final 3D models of the painted sample before the aging process integrated by the multi-band imaging data.

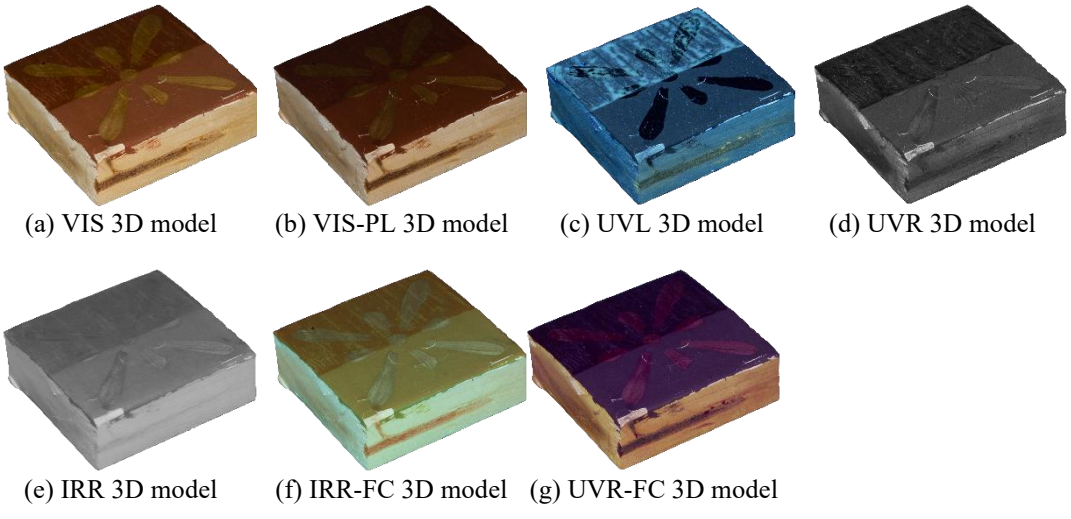

(a) VIS 3D model (b) VIS-PL 3D model (c) UVL 3D model (d) UVR 3D model

(e) IRR 3D model (f) IRR-FC 3D model (g) UVR-FC 3D model

Figure 7.8 Final 3D models of the painted sample after the aging process integrated by the multi-band imaging data.

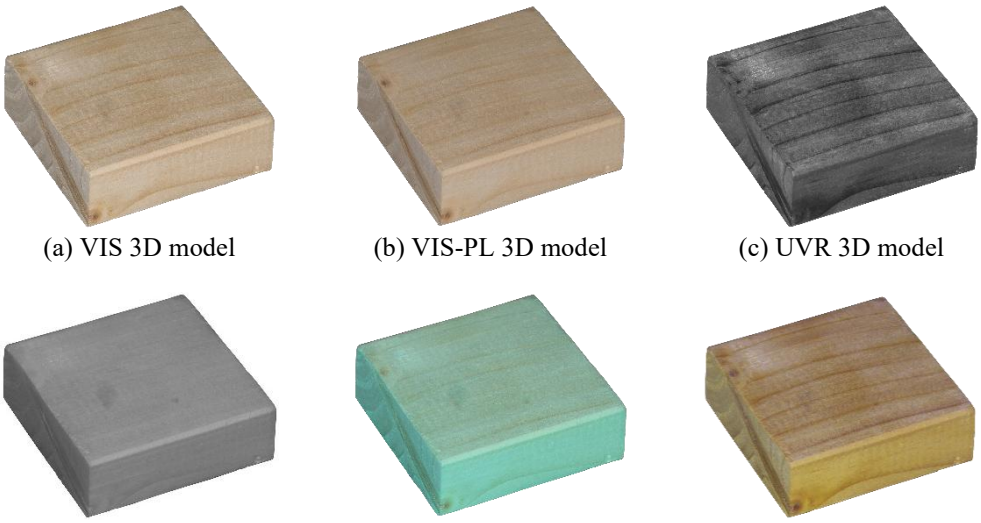

(a) VIS 3D model (b) VIS-PL 3D model (c) UVR 3D model

(d) IRR 3D model (e) IRR-FC 3D model (f) UVR-FC 3D model

Figure 7.9 Final 3D models of the wooden sample before the aging process integrated by the multi-band imaging data.

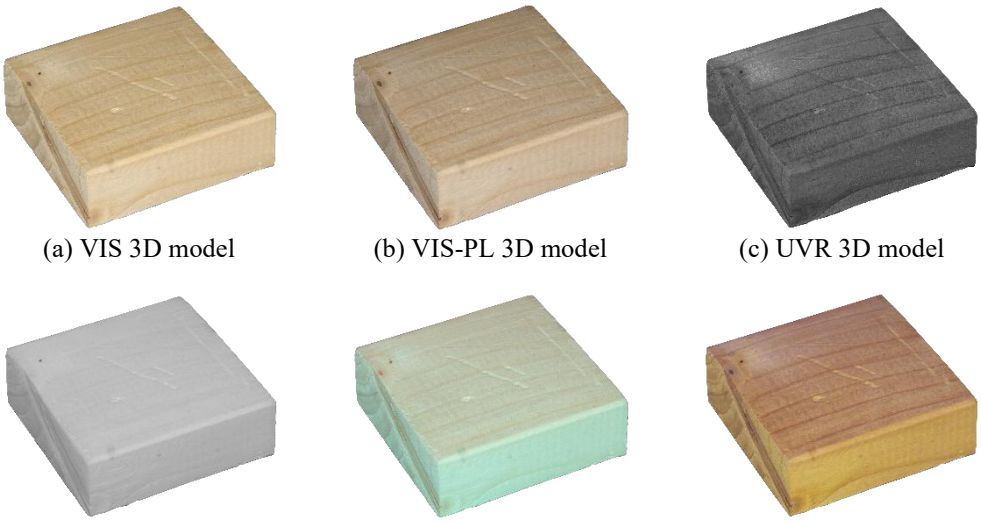

(a) VIS 3D model (b) VIS-PL 3D model (c) UVR 3D model

(d) IRR 3D model (e) IRR-FC 3D model (f) UVR-FC 3D model

Figure 7.10 models of the wooden sample after the aging process integrated by the multi-band imaging data.

7.1.3 Influence of wavelength in 3D reconstruction

This chapter presents an evaluation of the 3D reconstruction results obtained for both the wood and wood painted samples. The main goal was to assess the capability of the software to generate accurate 3D models from image datasets acquired across different spectral bands, and to analyse the geometric consistency and qualitative differences between reconstructions derived from different regions of the electromagnetic spectrum [53].

For the wood sample, Metashape successfully aligned the images and reconstructed a 3D model for each of the spectral bands considered, namely VIS, VIS-PL, IRR, and UVR. It is important to highlight that the markers included in the acquisition setup played a dual role: they were used both for scaling the model and for supporting the identification of homologous points across the image sets. To verify the role of markers in the image alignment and matching process, a reconstruction test was performed by removing the markers from the images. As a result, in the absence of these markers, the software was unable to generate a viable 3D reconstruction in any of the spectral bands for either sample. The processing parameters corresponding to each reconstruction are reported in Table 7.3. The ground sampling distance (GSD), representing the spatial resolution in millimetres per pixel, remained constant across all bands, indicating uniform resolution. The reprojection error, defined as the deviation between the observed image points and the corresponding projected points computed by the software, was below the commonly accepted threshold of 1 pixel [105] in all cases, confirming the reliability of the reconstructions. The model derived from VIS-PL yielded the lowest reprojection error, while the highest value was observed in the VIS model. The RMS reprojection error was stable across all reconstructions, further supporting the consistency of the processing. Regarding mesh density, a notable reduction in the number of faces and vertices was observed in the model reconstructed from IRR.

Table 7.3 Processing parameters comparison of the multi-band 3D model reconstruction of the wood sample before the aging process.

	Wood sample (Epoch 0)			
Parameters	**VIS**	**VIS-PL**	**IRR**	**UVR**
Images	72	72	72	72
Aligned images	72	72	72	72
GSD (mm/pixels)	0.0448	0.0448	0.0444	0.0448
Reprojection error (pixels)	0.661	0.302	0.418	0.399
RMS reprojection error	0.141707	0.119829	0.142661	0.143992
Max reprojection error (pixels)	15.1227	1.76694	3.06032	2.48327
Vertices	1,249,417	1,219,543	650,770	1,965,782
Faces	2,496,187	2,436,976	1,300,869	3,925,897

Table 7.4 Processing parameters comparison of the multi-band 3D model reconstruction of the painted sample before the aging process.

	Painted sample (Epoch 0)				
Parameters	**VIS**	**VIS-PL**	**UVL**	**IRR**	**UVR**
Images	72	72	72	72	72
Aligned images	72	72	71	72	71
GSD (mm/pixels)	0.0315	0.0315	-	0.0312	-
Reprojection error (pixels)	0.35	0.379	1.95	0.364	1.36
RMS reprojection error	0.163929	0.140284	0.557482	0.114342	0.469972
Max reprojection error (pixels)	2.66822	2.7303	44.6211	2.37341	57.294
Vertices	3,076,916	2,778,945	-	3,276,696	-
Faces	6,149,560	5,556,647	-	6,551,440	-

On the other hand, the models obtained from VIS and VIS-PL exhibited similar levels of detail, while the UVR reconstruction resulted in the highest number of faces and vertices, suggesting enhanced feature detection in this spectral range.

In contrast, for the painted sample, Metashape could not successfully reconstruct 3D models from all spectral bands. The bands used in this case included VIS, VIS-PL, UVL, IRR, and UVR. The reconstruction parameters are detailed in Table 7.4. While the image alignment phase was generally successful, the dense cloud generation failed for the UVL and UVR bands. In these cases, the software produced sparse point clouds that were insufficient for generating a coherent 3D mesh. For the remaining bands, the results were consistent and comparable.

In conclusion, the results confirm that it is possible to achieve accurate 3D reconstructions from spectral bands other than the visible range. However, the success of such reconstructions is strongly influenced by the optical properties and material composition of the sample. The 3D models reconstructed in the VIS band produced meshes with greater detail for both the wood and painted samples. For this reason, within the context of this research, the 3D models obtained from VIS were adopted as the reference standard for comparative purposes across both sample types.

7.1.4 3D model comparison for aging monitoring

In this section, the shape variation of the samples was assessed by acquiring the wood and painted objects before and after the aging process, and subsequently comparing the corresponding 3D meshes. The comparison was carried out using CloudCompare, version 2.14.alpha.

For this analysis, the distance between the pre- and post-aging models was computed using the cloud-to-mesh tool. As for the comparison of the dimensional reference in Section 6.4, before the calculation of the distance between the 3D

models, the virtual replicas of each sample were preliminarily registered based on their geometric features. Without the need for additional scaling operations, the registration was performed using the model acquired before aging as the reference. Corresponding points were firstly manually selected on the surfaces of the two models, and then a more accurate registration was performed using the ICP algorithm. In this case, ICP registration yielded an RMS error of 0.185233, calculated over 49,842 points for the wood sample, and an RMS error of 0.111747, calculated over 49,797 points for the painted one.

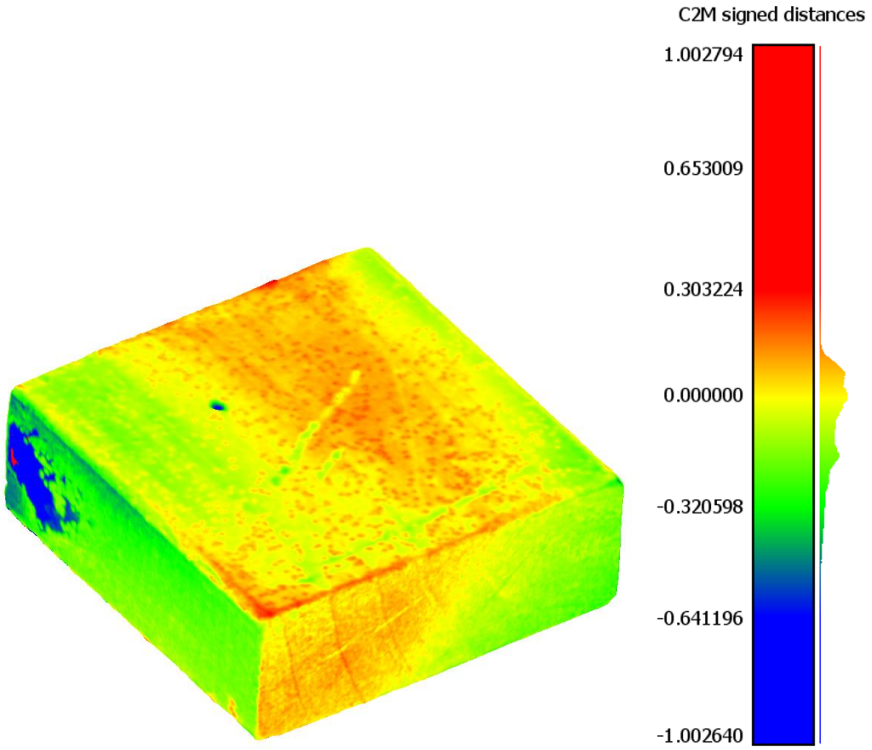

Figure 7.11 Cloud-to-mesh signed distances map (mm) between the photogrammetric models of the wood sample before and after the aging process; computed in CloudCompare.

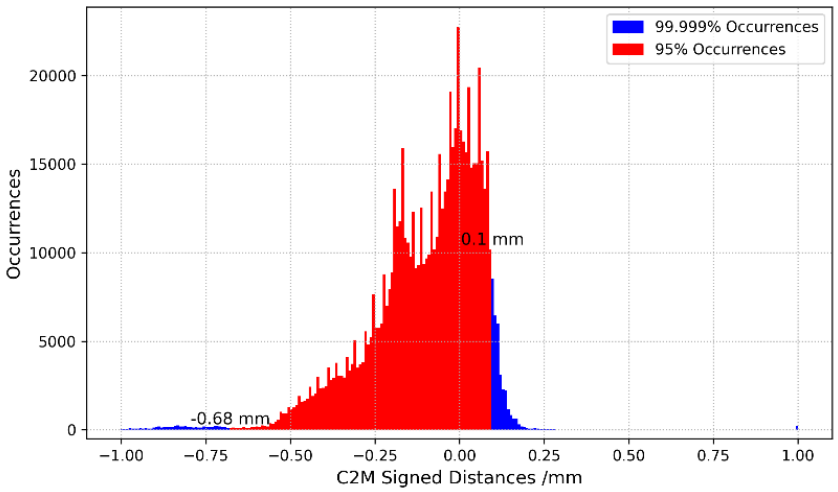

Figure 7.12 Histogram of computed distances (mm) from the 3D surface comparison for deformation monitoring of the wood sample; computed in CloudCompare.

Dimensional changes in the samples before and after aging were evaluated using comparative analysis of their 3D reconstructions. Signed distance maps and histograms reveal spatial insights into geometric variations over time and can indicate material degradation. Results are considered quantitative only if compared with data from another 3D acquisition technique with a known instrumental error, such as 3D scanning [106]. Therefore, this dissertation includes such a comparison to assess the accuracy and reliability of the photogrammetric measurements. The results of the comparison are presented in Figure 7.11 for the wood sample and in Figure 7.13 for the painted one, as color-coded signed distance maps. The results are visualized using a scalar field mapped onto the surface of the model, where color gradients represent the distribution and magnitude of the detected shape changes. The signed scalar field of the wood sample shows both localized and global changes in surface geometry. Yellow areas mark minimal or no deviation, indicating long-term structural stability. Green and blue are representative of negative deviations, where the surface of the model acquired after aging lies below the reference surface, indicating surface losses due to scratches and cracking, Red regions on the sample's upper face shows a positive deviation, due to the slight warping of the wood.

Regarding the wooden sample, based on the statistical values computed in CloudCompare, the mean distance is -0.100257 mm, indicating a general tendency toward material loss or shrinkage. The associated standard deviation is 0.164401 mm, which is of the same order of magnitude as the mean distance, reflecting the variability of the deformations across the surface.

According to the histogram shown in Figure 7.12, 95% of the surface exhibits deformation in the range of approximately -0.68 mm to 0.10 mm.

The most significant negative deformation, ranging from about -0.68 mm to -1 mm, are concentrated in correspondence of a deeper surface scratch, and the left corner of the sample. As noted in the previous Section 7.1.2, the deviation in the left corner area is not only due to physical degradation, but also to artefacts created during the 3D reconstruction of the pre-aging model. These artefacts were not

present in the post-aging model. Similarly, small red zones on the upper face of the sample correspond to mesh holes or missing data in the pre-aging model, which were resolved in the post-aging acquisition.

The comparison of the painted sample, represented in Figure 7.13, also reveals shape changes consistent with material degradation. Areas with negligible or very small variations are represented in green, indicating preservation of surface geometry in those areas. The mean distance is -0.035982 mm, with a standard deviation of 0.108343 mm. This lower variability, compared to the wood sample, likely reflects a more stable acquisition process, attributable to the richer texture of the painted surface, and the absence of significant reconstruction artifacts in both models. As shown in Figure 7.14, 95% of the surface shows deformations between approximately -0.45 mm and +0.12 mm. Positive deviations, represented in red (values ranging from +0.12 mm up to approximately 1 mm), are primarily associated with the lifting of the paint film and localized accumulation of the varnish. These features are typical of surface alteration due to solvent evaporation and subsequent shrinkage during the aging process.

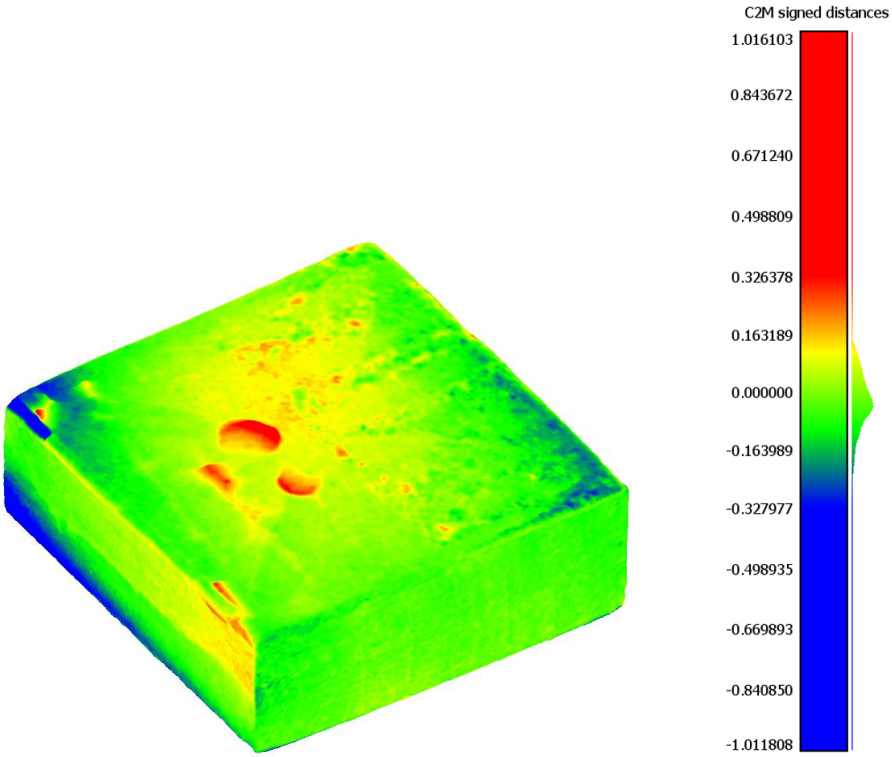

Figure 7.13 Cloud-to-mesh signed distances map (mm) between the photogrammetric models, before and after the aging process of the painted sample; computed in CloudCompare.

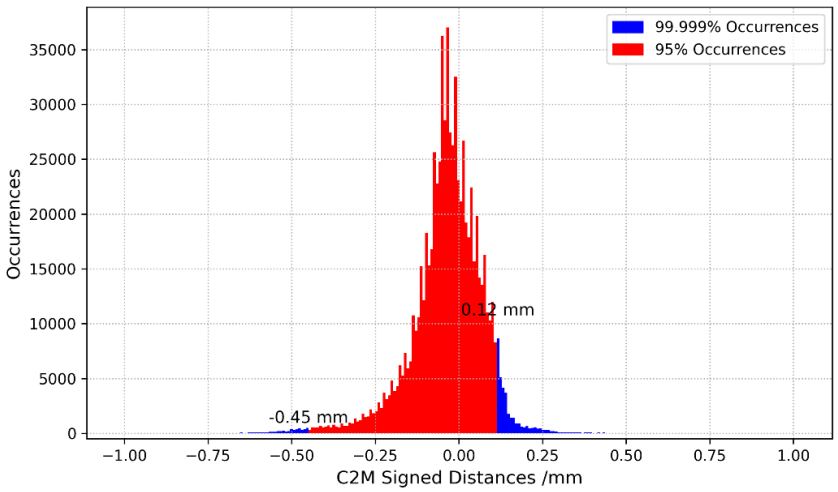

Figure 7.14 Histogram of computed distances (mm) from the 3d surface comparison for deformation monitoring of the painted sample; computed in CloudCompare

Negative deviations, shown in blue (approximately -0.30 mm to -1 mm), indicate material loss or shrinkage. These include losses of the preparation and paint layers, or the paint layer alone, and shrinkage of the varnish, resulting from solvent evaporation.

The use of signed distance analysis in this context enables a detailed quantitative assessment of micro- and macro-deformations, with spatial resolution limited only by the ground sampling distance of the photogrammetric models. The reported mean distances, standard deviations, and distance ranges offer objective metrics for evaluating material stability over time.

Furthermore, the color-mapped scalar field provides an intuitive visualization of the spatial distribution of degradation, facilitating the identification of patterns linked to mechanical stress and material heterogeneity. The integration of these results with anatomical and material information supports a comprehensive interpretation of the observed deformation phenomena.

7.2 Laser scanning models

The laser scanning acquisitions were carried out with the main aim of validating and comparing the deformation detected in the samples before and after the aging process, as identified through photogrammetric reconstruction. For each sample, a corresponding 3D model was acquired using laser scanning at the same time as the photogrammetric acquisition. This allowed for a direct comparison of the geometric variations measured by two different 3D acquisition techniques.

For detailed information regarding the instrument specifications and acquisition setup, refer to Section 6.4, which applies equally to the scans performed in this part of the study, as the setup remained consistent with that used for acquiring the dimensional reference described in Chapter 6.

7.2.1 3D comparison for aging monitoring

This section reports on the shape variation of both the wood and painted samples, determined by comparing the laser scans acquired before and after the aging process. In contrast to photogrammetry, the output of laser scanning consists of raw point clouds, where each point represents specific coordinates in the three-dimensional space.

Before data evaluation, all point clouds were manually cleaned to remove extraneous points not belonging to the object surface, for example, points corresponding to the support base. After cleaning, the point clouds for the painted sample consisted of 8,035,059 points before aging, and 6,076,083 points after the aging process. For the wood sample, the point clouds included 3,523,141 points before the aging process and 3,014,155 points after aging.

As with the photogrammetric comparison, the analysis was performed using the CloudCompare software. However, considering the laser scanning output, the cloud-to-cloud distance tool was used in this case. The pre-aging scan was used as the reference model for the initial rough registration, which was then refined using the ICP algorithm. This procedure resulted in an RMS registration error of 0.374645 mm for the wood sample and 0.305464 mm for the painted sample, each calculated over 50,000 sampled points.

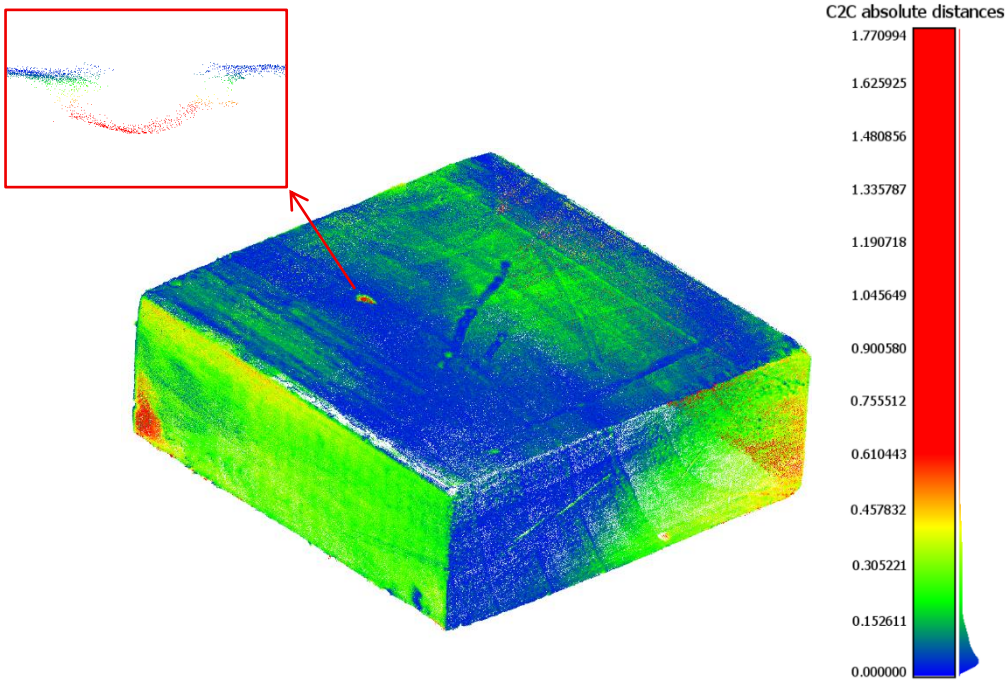

Figure 7.15 Cloud-to-cloud absolute distance map (mm) computed in CloudCompare between the point clouds acquired by laser scanning, before and after the aging process of the wood sample. In particular, the section of the point cloud in correspondence of a wooden deformation is presented.

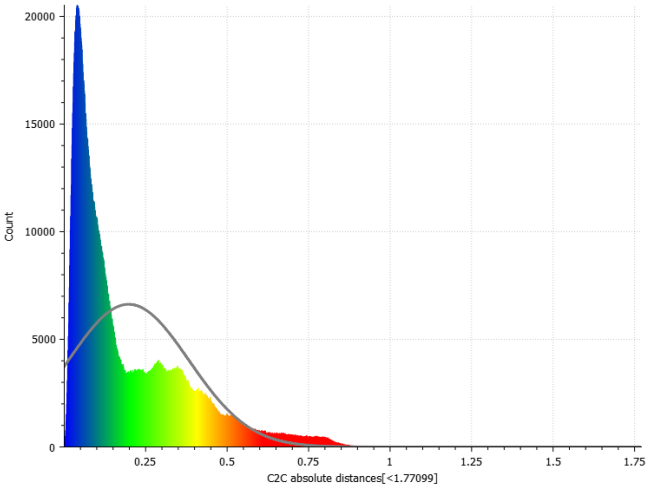

Figure 7.16 Histogram of computed absolute distances (mm) extracted in CloudCompare from the cloud-to-cloud distance comparison for deformation monitoring of the wooden sample.

The laser scanner provides directly scaled data, avoiding the need for any further scaling operations during post-processing.

Due to the nature of the cloud-to-cloud comparisons in CloudCompare, only the absolute distances can be computed, meaning that all the deviations are reported as positive values starting from 0. While the absence of signed values reduces the immediacy of interpretation compared to signed distance maps, the resulting color-coded absolute distance maps still effectively highlight regions affected by geometric variation.

The absolute distance map generated from the comparison of the wooden sample before and after aging is shown in Figure 7.15. Areas shown in blue correspond to minimal deviations, close to 0 mm, indicating stable geometry. Regions rendered in green indicate increased surface variation, which is consistent with deformation due to wood warping when compared with photogrammetric results. The presence of surface cracks along the right cross-section is also highlighted in green. Larger deviations are shown in red, particularly around the deepest scratches, and the left corner of the sample. These areas likely correspond to more pronounced warping in the sample's shape that were not as evident as in the photogrammetric comparison, potentially due to the artefacts generated in the photogrammetric 3D model creation process.

The maximum detected deviation is approximately 1.8 mm; however, this value reflects the presence of outlier points rather than the true geometric features of the sample. The computed mean distance is 0.198359 mm, with a standard deviation of 0.184979 mm. Figure 7.16 presents the histogram of the absolute distances.

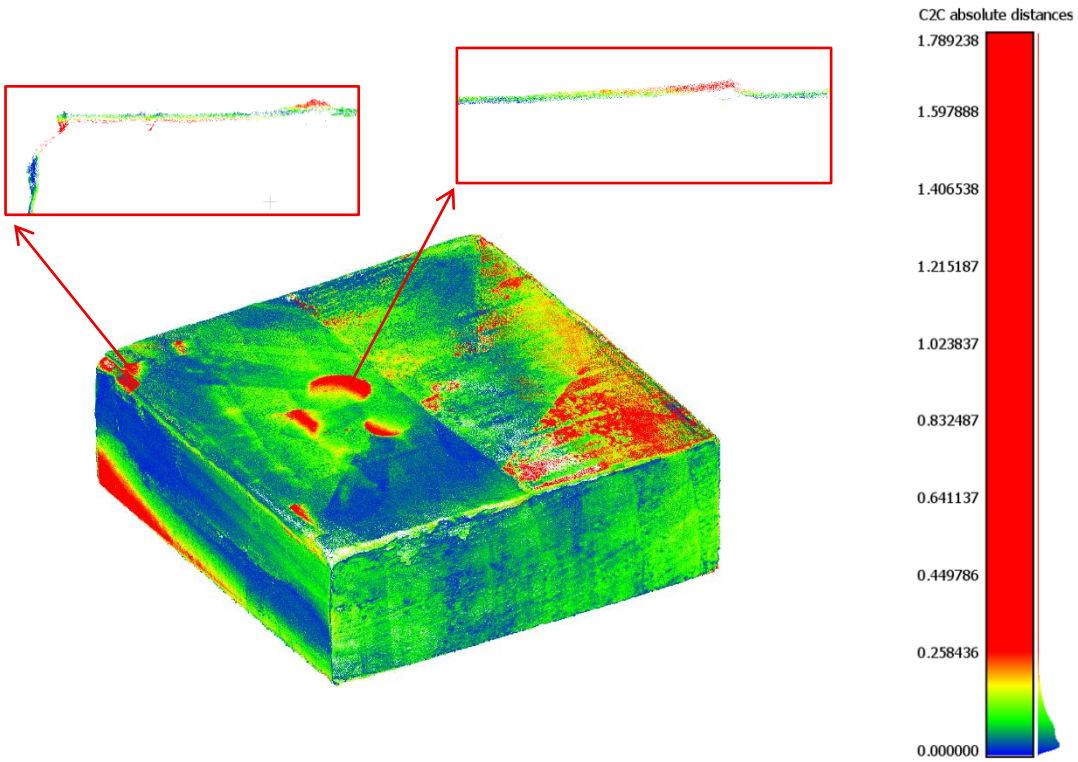

Figure 7.17 Cloud-to-cloud absolute distance map (mm) between the point cloud acquired by laser scanning, before and after the aging process of the painted sample, calculated with CloudCompare. In details, sections in correspondence of deeper deformations between the point clouds considered: a paint and preparation layer loss (left) and a paint layer lifting (right).

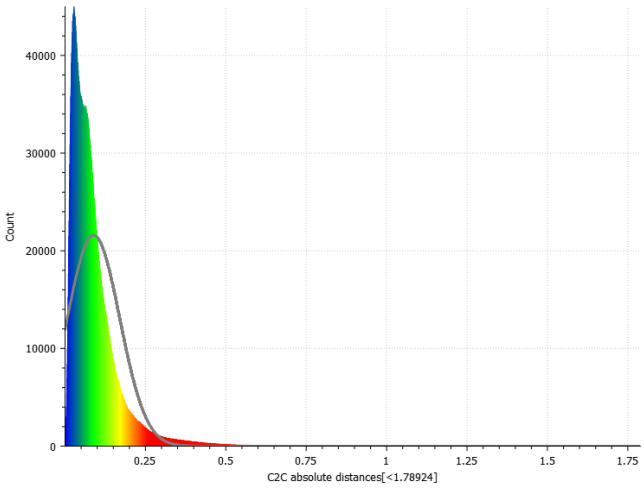

Figure 7.18 Histogram of absolute computed distances (mm) from the cloud-to-cloud distance comparison for deformation monitoring of the painted sample; computed in CloudCompare

As described before, a cloud-to-cloud comparison was conducted for the painted sample. The resulting absolute distance map highlights in red the areas exhibiting the most significant deformation, primarily corresponding to the losses and lifting areas of the preparation and painted layer, shown in details in Figure

7.17. These are likely the result of mechanical stresses and material shrinkage caused by the aging process. The right corner of the sample reveals limitations in the performance of the laser scanner. Specifically, both the scans taken before and after the aging process show less point density in areas of high surface reflectivity, namely the half-varnished surface of the sample. Although the scans were performed from multiple angles, the instrument struggled to acquire more dense point clouds from the reflective surface. This is particularly evident in the pre-aging scan, where the lack of data results in localized discrepancies when compared to the denser point distribution in the post-aging scan. The red-highlighted region in this case reflects these acquisition limitations rather than actual material deformation. The computed mean distance for the painted sample is 0.088899 mm, with a standard deviation of 0.081398 mm, indicating lower overall variability compared to the wooden sample. Figure 7.18 shows the histogram of absolute distances for this comparison.

7.3 Cross-technique comparison

This section presents a direct comparison between the two 3D acquisition techniques employed in this study: photogrammetry and laser scanning. Since both the wooden and painted samples were acquired the same number of times at the same stage, it was possible to assess the consistency between the virtual replicas produced by the two methods. Specifically, the acquisition of each sample before the aging process was considered.

To perform this analysis, the point cloud acquired through laser scanning was compared with the mesh generated by photogrammetry. Although it was possible to extract a point cloud from the photogrammetric model, the mesh was preferred for photogrammetry while retaining the point cloud for laser scanning, in order to compute the signed distance map in CloudCompare, which provides more informative visual feedback than absolute distances.

For this reason, a cloud-to-mesh comparison was conducted, where the photogrammetric mesh was considered as the reference geometry. This was necessary due to CloudCompare's limitation that prevents assigning a point cloud as the reference in cloud-to-mesh operations. As a result, signed distances were computed on the point cloud in relation to the mesh, resulting in a signed scalar field map for a better intuitive interpretation of positive and negative deviations.

The comparison between the laser point cloud and the photogrammetric mesh of the wood sample shows geometric deviations ranging from approximately -0.8 mm to +0.3 mm, as represented in Figure 7.19. However, some of these deviations are due to the creation of some unwanted artefacts in the photogrammetric mesh reconstruction, observed and discussed in the previous sections. The histogram in Figure 7.20 shows that 95% of the surface deviations fall within the range of -0.64 mm to +0.05 mm, suggesting that the majority of the model surface lies within a deviation range of about 0.7 mm. The computed mean distance is -0.030825 mm, and the standard deviation is 0.078387 mm. These results suggest a good

correspondence between the two methods for this sample, characterized by limited discrepancies.

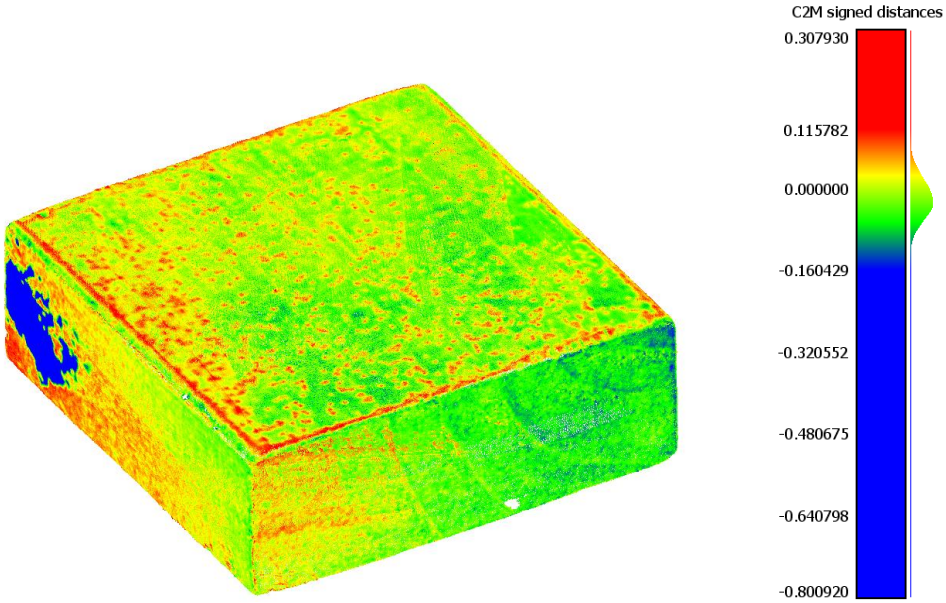

Figure 7.19 Cloud-to-mesh signed distance map (mm) between the photogrammetric mesh and the laser point cloud acquired before the aging process of the wood sample, computed in CloudCompare.

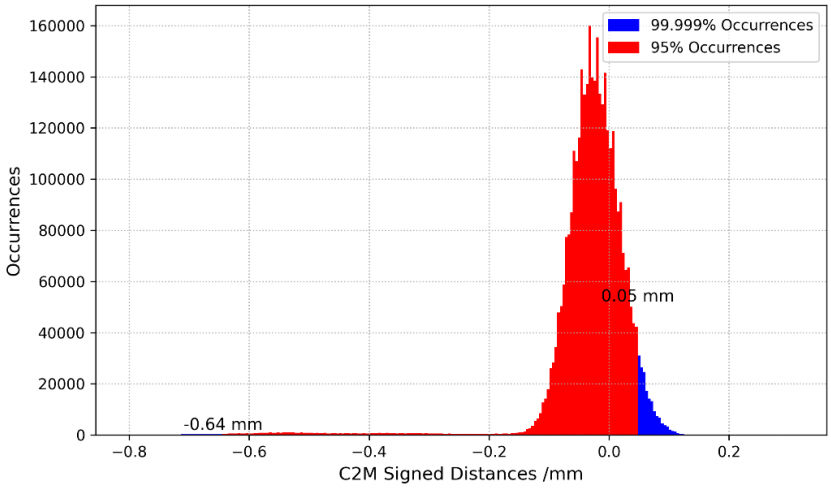

Figure 7.20 Histogram of computed distances (mm) from the 3D surface comparison between the photogrammetric and laser scanning technique of the wood sample, acquired before the aging process, computed in CloudCompare

The same comparison procedure was applied to the painted sample. The resulting signed distance map (Figure 7.21) shows a wider range of deviations, from approximately -6.24 mm to +6.29 mm. However, this range is influenced by the presence of isolated points in the laser-scanned point cloud, which do not represent meaningful features of the object's surface and are not relevant for dimensional evaluation. According to the histogram in Figure 7.22, 95% of the point deviations

fall within -4.05 mm to +0.03 mm. Nevertheless, the actual distribution is heavily concentrated around a narrower range. The calculated mean distance is -0.020867 mm, and the standard deviation is 0.056272 mm, suggesting a good level of correspondence between the two models.

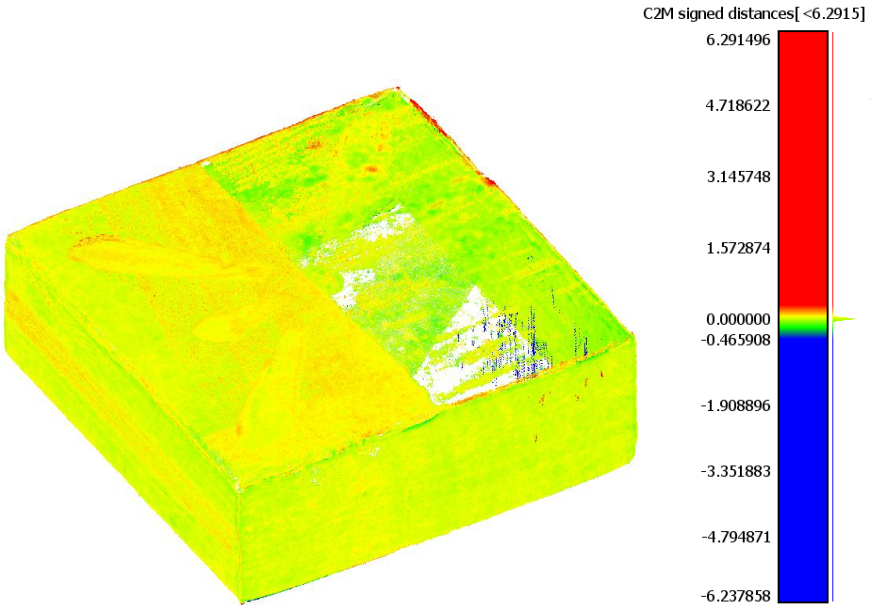

Figure 7.21 Cloud-to-mesh signed distance map (mm) between the photogrammetric mesh and laser scanned point cloud acquired before the aging process of the painted sample, computed in CloudCompare.

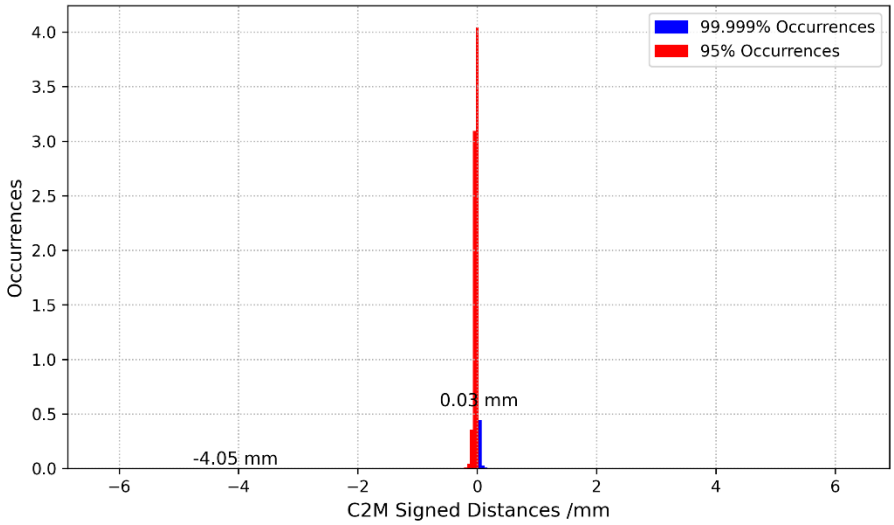

Figure 7.22Histogram of computed distances (mm) from the 3D surface comparison between the photogrammetric and laser scanning technique of the painted sample, acquired before the aging process, computed in CloudCompare.

For each sample, the observed standard deviation values below 0.1 mm between the photogrammetric and the laser scanning datasets confirm that

photogrammetry is capable of detecting millimetric and sub-millimetric deformations when performed under these specific conditions. This level of accuracy is generally considered acceptable in the field of cultural heritage, particularly for the monitoring of dimensional changes in wooden artifacts and painted surfaces. Specifically, for applications involving the detection of paint film lifting, losses in the preparation layer, or localized shrinkage due to aging, this resolution is able to capture changes on the order of millimetres or less. Similarly, regarding wood deformation, sub-millimetric changes are critical for understanding the mechanical behaviour of wood in response to environmental variations and can provide meaningful indicators of early-stage structural instability. The accuracy could be further increased by using cameras with higher-resolution sensors and improved optical performance; however, the current low-cost configuration already provides reliable results for cultural heritage documentation and monitoring. Unlike laser scanning systems, which are typically calibrated and characterized by a manufacturer-declared measurement uncertainty, photogrammetric reconstructions are not associated with an intrinsic instrumental error. Consequently, in order to regard photogrammetric data as quantitative, their dimensional accuracy must be validated against a reference technique such as laser scanning, which provides metrological traceability through its known measurement uncertainty.

Chapter 8

Case studies

This chapter presents some case studies in which 3D photogrammetry and multi-band imaging were applied to support multi-analytical diagnostic campaigns and related conservation and restoration interventions.

Some of the works described in this chapter have been previously published in [59].

8.1 Gilded and ungilded bronze sculptures from Museo delle Civiltà of Rome

The present study is part of amultisciplinary cooperation between the Politecnico di Torino, the Centro per la Conservazione ed il Restauro dei Beni Culturali "*La Venaria Reale*", the Museo di Arte Orientale (MAO) of Turin and the Museo delle Civiltà of Rome, aimed to evaluate the conservation state of a set of metallic artefacts by means of non-destructive and non-invasive analyses in order to design tailored preservation strategies. In particular, this section is focused on the chemical-physical characterization of ten gilded and ungilded Chinese small bronze sculptures of the Museo delle Civiltà (MuCiv) in Rome, dated back to the fifth and sixth centuries.

As objects made of metallic material, monitoring the state of preservation and the corrosion products' progression on artifacts, especially the gilded ones, is particularly important. The advancing growth of corrosion products at the interface of the metal/gold layers, with the subsequent formation of the characteristic corrosion craters, can lead to blistering or cracking of the gold layer, up to its total loss [107].

X-ray fluorescence spectroscopy (XRF), has been employed to analyze the Buddish gilded and ungilded sculptures to obtain information about their chemical composition and the gilding technique utilized. Moreover, Raman spectroscopy was employed to investigate the degradation condition of some sculptures through the identification of the corrosion products. Finally, a 3D model of one of the gilded

sculptures was acquired using the cross-polarization technique, which enables the generation of virtual replicas of objects characterized by reflective metallic surfaces, which is not possible with traditional photogrammetric approach.

8.1.1 The artifacts

This section presents the study of a group of Chinese bronze sculptures from the Museo delle Civiltà (MuCiv) in Rome, dated back to the fifth–sixth centuries. Specifically, the group of artifacts identified with their inventory numbers consists of six gilded bronze small sculptures shown in Figure 8.1 (INV. 625, INV. 631, INV. 659, INV. 667, INV. 669, INV. 670), and four ungilded sculptures (INV. 650, INV. 695, INV. 708, INV.710), shown in Figure 8.2.

(a) INV. 625 (b) INV. 631 (c) INV. 659

(d) INV. 667 (e) INV. 669 (f) INV. 670

Figure 8.1 Images of six small gilded bronze sculptures from the Auriti's collection of the Museo delle Civiltà of Rome: (a) INV.625, Bodhisattva Padmapani, VI Century, East Wei Dynasty; (b) INV.631, Standing Bodhisattva Avalokitesvara, VI Century, North Wei Dynasty; (c) INV.659, Seated Maitreya, VI Century, Unknown Dynasty; (d) INV. 667, Seated Buddha, VI Century, Wei Dynasty; (e) INV. 669, (f) INV. 670, Buddha with assistants, VI Century, North Qi/Su Dynasty

(a) INV. 650 (b) INV. 695 (c) INV. 708 (d)INV. 710

Figure 8.2 Images of four small ungilded bronze sculptures from the Auriti's collection of the Museo delle Civiltà of Rome: (a) INV.650 - Standing Bodhisattva Avalokitesvara, VI Century, Wei Dynasty; (b) INV.695 - Standing Bodhisattva Padmapani, VI Century, North Wei Dynasty; (c) INV. 708 - Bodhisattva in the attitude of "prince through" VI Century, East Wei Dynasty; (d) INV. 710- Buddha in Dyanamudra, V Century, North Wei Dynasty.

The bronze sculptures belonging to the Auriti collection, a group of more than 90 artifacts gathered by Japanese collectors and dealers and taken to Italy via diplomatic channels by the Ambassador Giacinto Auriti during his diplomatic mission in Japan (1933-1940) [108]. Several small bronze sculptures, similar to the ones of the Aurit's collection, were produced in China from the fourth century, with the function of talismans for the protection of travellers or as protectors of the house where they were placed on an altar or in temples. They were often grouped according to different types of Buddhist representations, such as Bodhisattvas, disciples, guardians and donors located around the Buddha.

Only six of the sculptures considered was gilded, but gilding techniques are many and varied: from plating to leaf gilding to gilding techniques involving a mercury-gold amalgam. Indeed, since the Third century B.C.E., in China, the use of mercury (also formerly called "quicksilver") in amalgam with gold, spread rapidly and soon replaced leaf gilding [109]. As a matter of fact, leaf gilding is more complex since involves the production and application of the gold leaves themselves. In addition, the increased use of mercury techniques could be due to its increased availability [110]. Mercury was extracted by sublimation from cinnabar, and heated to a temperature of 500 – 600°C. Today, it is impossible to say when this practice was introduced even if there is written evidence from the first century C.E. documenting a significant use of mercury from the Fifth century B.C.E. [109]. Starting from China, the use of fire-gilding spread all over the world [111], until the invention of electroplating in the middle of the nineteenth century C.E. [112]. Historically, two different techniques are mentioned: cold mercury gilding and fire gilding. The first one, mentioned by Pliny, consists of spreading mercury on the metal surface as an adhesive for the application of the gold leaves. Then, mercury was allowed to evaporate by dissipation [109]. Far more widespread is the fire

gilding technique: firstly, fragments of gold were dissolved in mercury at moderate temperatures to obtain the amalgam, and then spread over the clean metal surface of the object. Finally, the surface was heated to high temperatures to allow mercury to evaporate (melting point of Hg = 356.5°C), leaving a tightly bonded layer of gold [107], [113], [114]. Therefore, the process is characterized by the presence of residual outward mercury, easily detectable by different techniques, such as the XRF analyses [107], [109]. However, it is difficult to discriminate between hot and cold mercury gilding: the percentage of residual mercury is both remarkable, but also very similar. Finally, the resultant gold layer was "burnished" by an ultra-smooth and hard tool, usually an agate stone, to achieve a shiny, bright surface [115]. In some cases, the layer obtained by fire gilding shows different golden shades. This behavior is due to the variation in the amount of silver present, not only as an inclusion of the gold but directly within the amalgam [111]. On occasion, the fire gilding technique was used in combination with other gilding techniques [109]; the presence of small gold leaf details added using a resin as an adhesive, probably a lacquer, was testified [116]. The main difference is that the fire gilding technique, because of the flow of the amalgam, does not always allow for sharp edges to be defined. In contrast, leaf gilding allows areas of gilding to be perfectly outlined. The most important Chinese substrates used for gilding were by far the copper alloys, followed by silver, and brass, used from the 16th century onward to strike coins [111]. Because of the extensive production of bronze objects, it is likely that China had access to several mines for extracting copper, tin, zinc, and lead [117]. While the technique of fire gilding remained unchanged over time, a modification in the composition of copper alloys is attested. The earliest substrates noted are marked by a low tin and lead content, quantitatively higher from the Fifth century CE onward, until the 20th century [111]. On the other hand, casting techniques are a really discussed and controversial field in China [118], [119]; no ancient foundry employed for casting Buddhist works has ever been found, so all notions are obtained by deduction by observing existing objects. In China, it is attested that piece-mold casting was the most widely used, and probably the only known, technique employed for the production of metal Buddhist images until the late 6th century and early 7th century. In this period, the lost-wax casting technique spread in northern China. However, it is often very complicated to distinguish which of the two techniques was used, since they were sometimes employed together in the making of the same sculpture [116].

8.1.2 Measurement campaign

8.1.2.1 X-Ray Fluorescence Spectroscopy

X-ray fluorescence spectroscopy has been employed to analyze the Buddhist gilded and ungilded sculptures and to obtain information about the gilding technique. Analyses were performed on all sculptures, using a portable XRF Bruker Tracer 5i spectrometer, equipped with a 20 mm2 CCD detector and Rhodium (Rh) anode. In the present case, the analyses were performed by setting voltage and

current to 40 kV and 30 μA, respectively, using a 3 mm collimator and a Cu 75 μm/Ti 25 μm/Al 200 μm filter. The recorded spectra were processed using Artax Spectra 8.0.0.476 software. Under these operating conditions, without standard samples and calibration models, the data collected are not quantitative but allow for semi-quantitative determination of the elements present in the alloys.

The analyses were carried out in several area on each sculpture, to investigate the composition of the main body and of the separated or decorative elements, when present. In order to investigate the gilding technique, spectra were acquired on the gilded surface and in areas where the gold layer was missing and the metal surface was exposed. In addition, analyses were carried out in correspondence of corrosion products to gather information on their composition.

Table 8.1 Artifacts in the Auriti's Collection: Inventory number (INV. N°), Century, Dynasty, height and Surface treatment.

Inv. N°	Century	Dynasty	Heigth (cm)	Surface
INV.650	VI Century	Wei	27.4	ungilded
INV.695	VI Century	North Wei	15.8	ungilded
INV.708	VI Century	East Wei	7.9	ungilded
INV.710	V Century	North Wei	10.9	ungilded
INV.625	VI Century	East Wei	22.0	gilded
INV.631	VI Century	North Wei	11.0	gilded
INV.659	VI Century	Unknown	10.4	gilded
INV.667	VI Century	Wei	29.8	gilded
INV.669	VI Century	North Qi	15.0	gilded
INV.670	VI Century	North Qi/Su	19.0	gilded

Results

The X-ray fluorescence spectroscopy (XRF) allowed the determination of the elemental composition of the alloys of all the artifacts of the Auriti's Collection.

The XRF data obtained on the ungilded sculptures are analogous among the overall set. The ungilded artifacts are composed of a bronze alloy, with Cu, Pb, Zn, Sn, with minor traces of As, Ag, Sb, Fe, Zn, Hg. No major differences have been detected in the composition either among the different sculptures or among several areas within the same sculpture. Representative XRF spectra acquired on INV. 708 are shown in Figure 8.3. The spectra were acquired on several areas of black, red, bright green, and green colors.

In particular, the alloy is characterised by the presence of major elements such as copper (Cu), zinc (Zn), iron (Fe), nickel (Ni), and tin (Sn) demonstrated by the presence of peaks at 8.05 keV (Cu-Kα), 8.9 keV (Cu-Kβ), 9.57 keV (Zn-Kβ), 6.4 keV (Fe Kα) and 7.05 keV (Fe-Kβ), 7.48 keV (Ni-Kα), and 3.44 keV (Sn-Lα), 3.66 keV (Sn-Lβ), 25.27 keV (Sn-Lα), 28.44 keV (Sn-Kβ), 29.11 keV (Sn-Kβ). Also, arsenic is present, as can be seen from the presence of the peaks at 10.54 keV (Kα) and 11.72 keV (Kβ). The peak at 10.54 keV could also be assigned to the Lα of Pb.

Indeed, the K shell intensity ratio (Kβ/Kα) is not respected for As *[120]*, thus the peak at 10.55 keV is due to the overlapping of both the Pb-Lα and As-Kα lines. The presence of Pb is furthermore confirmed by the peaks at: 12.32 keV (Lβ), 12.61 keV Lβ, 13.00 keV (Lβ5), 14.76 keV (Lγ), and 15.09 keV (Lγ). It is possible to identify other elements in the alloy, such as manganese (5.88 keV, Kα), mercury (9.98 keV, Lα), Zr (15.77 keV, Kα), Ag (22.16 keV, Kα), and Sb (26.36 keV, Lα and 29.72 keV, Kβ). The peaks at 16.06 keV Cu(Kα+Kα) and 16.97 keV Cu(Kα+Kβ) can be attributed to copper sum peaks. The peaks of Kα and the Kβ lines related to the rhodium anode are present at 20.22 keV and 22.72 keV, respectively. The broad peak at 19.06 keV can be attributed to the Rh Compton scattering and the peak at 1.48 keV to the Kα of Al. These peaks are due to instrument contribution. Chlorine (2.62 keV, Kα) has been identified in correspondence of green areas of the surface.

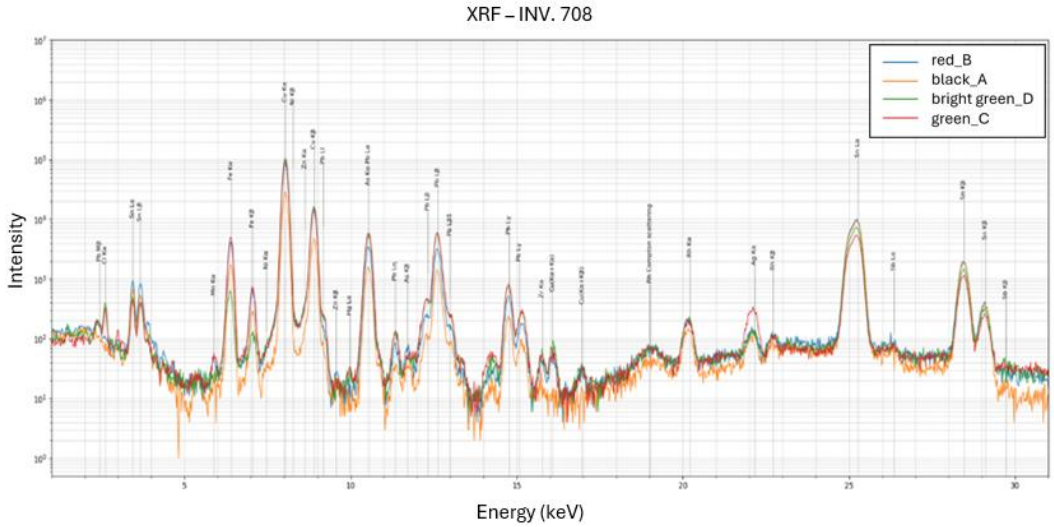

Figure 8.3 XRF spectra of the ungilded artifact INV. 708. Spectra recorded on different areas of the sculpture, i.e. black, red, bright green, and green.

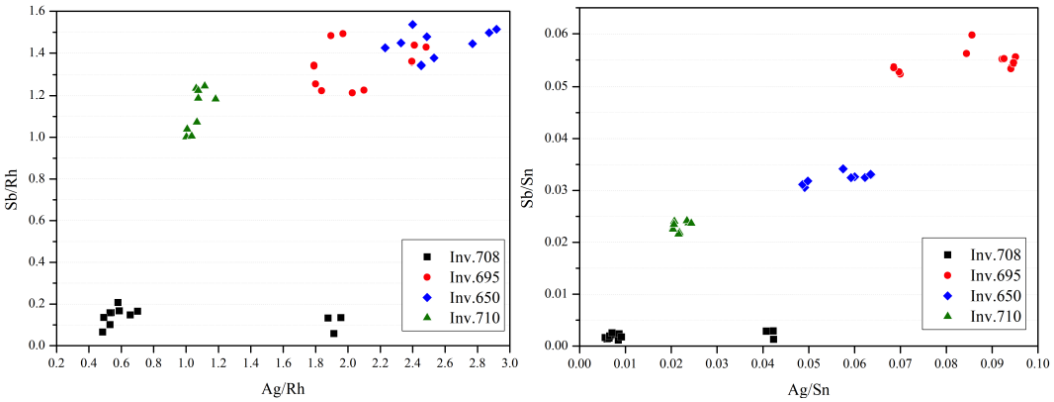

(a) (b)

Figure 8.4 XRF Analysis of ungilded artifacts (INV. 708, INV. 695, INV. 650, INV. 710): scatterplot of net-rates of (a) Sb/Rh vs. Ag/Rh; (b) Sb/Sn vs. Ag/Sn. See the legend for color information.

Compared to all the artifacts in the collection, sculpture INV. 708 (Figure 8.3) presented a more extensive corrosion products distribution of the bronze surface. Therefore, the analysis points were located in correspondence with areas marked by different color and morphology (black, green, greenish-blue, and red) to have more insights into the chemical composition. The areas affected by greenish and light-blue hues are characterized by a higher concentration of copper (Cu) and chlorine (Cl).

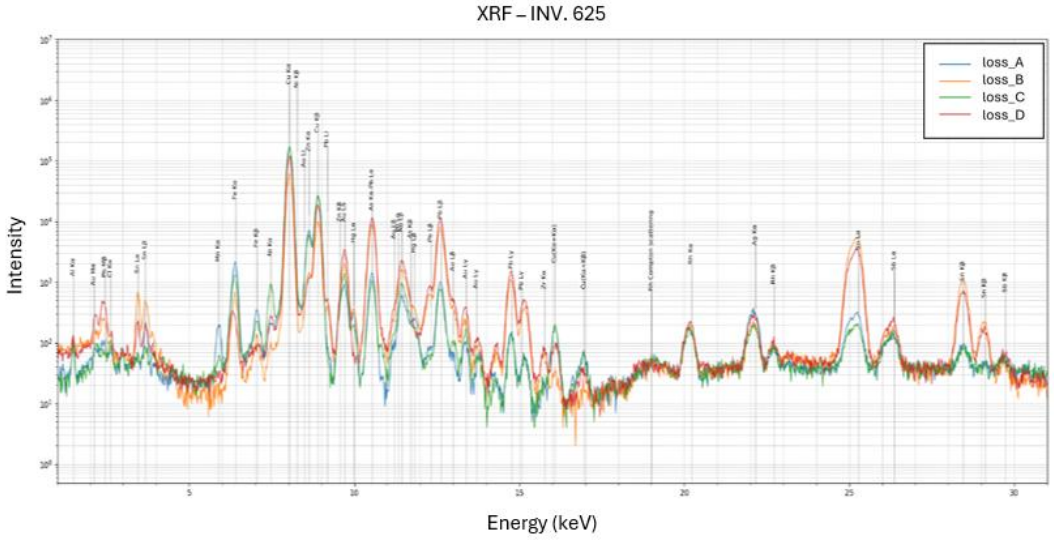

(a)

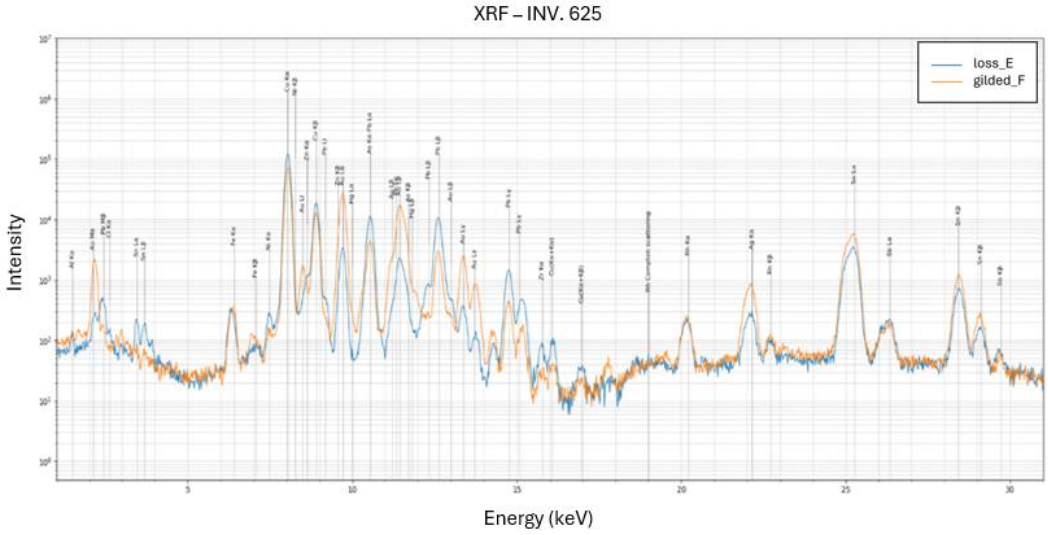

(b)

Figure 8.5 XRF spectra of the ungilded artifact INV. 625. Spectra recorded in correspondence of gold losses (a), and in presence of gold, showed in comparison with a gold loss (b)

The gilded sculptures group is characterised by a bronze alloy of copper, tin, and lead, with traces of iron, silver, and zinc. In the case of the gilded artifacts is not possible to confirm or exclude the presence of As, since the characteristic lines of arsenic overlap with the ones of Au and Hg.

In addition, in the case of the sculptures made of separated elements, there was no evidence of major differences in the chemical composition of the different parts, but a difference in the relative concentration of specific elements was found. In particular, a different amount of tin, copper, and/or lead of the bronze alloy was found. For example, in the INV. 625 bronze sculpture, the concentration of the metals' alloy changed between the mandorla, the basement, and the body of the artifact. In general, the artifacts with decorative or applied elements exhibit a variation in the concentration of the constituent metals of the alloy. This is evident both in artifact INV. 669, which shows a difference between the halo and the rest of the body, and in artifact INV. 670, in which the gold decorative element is distinguished from the metal support plate, applied on the back.

Regarding the gilding technique, the XRF data collected in correspondence with the 21 gilded areas highlighted the presence of gold (Au) and mercury (Hg). These elements have been identified even in the ungilded areas, gathering useful information concerning the artistic technique of the works of art. Indeed, the presence of mercury, which is absent in the other gilding techniques, suggest the use of an amalgam gilding. Figure 8.5 shows the XRF data collected on the artifact INV. 625, representative of the gilded sculptures group.

In conclusion, XRF analyses allowed the identification of the elemental composition of the sculptures investigated. In particular, it was possible to highlight the use of different copper-based alloys employed for manufacturing entire sculptures or parts of them, as some decorative or supporting elements. In detail, the bronze artworks are made with copper (Cu), tin (Sn), and lead (Pb) based alloys, with traces of iron silver (Ag) and zinc (Zn). This composition agreed with the typical artistic technique of coeval Chinese sculptures, noted from the Fifth century C.E. forward by the predominant use of bronze in metal manufacturing, marked by high percentages of lead and tin (≈ 10 to 20 wt%). Concerning the six gilded sculptures (INV. 625, INV. 631, INV. 659, INV. 667, INV. 669, INV. 670), XRF analyses were fundamental for the characterization of the gilding technique. In particular, in the overall group of gilding artifacts, the surface presence of mercury (Hg) was detected in correspondence with the gilding losses. The detection of mercury is clear evidence of the fire-gilding technique, consisting of a mercury and gold amalgam applied on the bronze surfaces. Then, most of the mercury slowly evaporates, inducing a thin superficial gold layer creation, denoted by residual Hg. In addition, further details about the gilding technique were provided by Raman spectroscopy analysis and the detection of rouaite, found on the artifacts INV. 667. Rouaite owes its formation to the exposure of the metal surface to high heating [117], confirming the hypothesis of the fire-gilding technique. The amalgam was applied to the metal surface and then heated to complete the evaporation of mercury, resulting in a glossy and shiny surface [111].

8.1.2.2 Raman Spectroscopy

Raman spectroscopy, an efficient analytical technique that allows the identification of the corrosion products in a non-destructive, non-invasive manner,

was employed to investigate the degradation condition of some sculptures. The analyses were performed using three different portable instruments equipped with lasers with excitations of 532 nm, 785 nm, and 1064 nm, respectively, and CCD sensors. Details on the instrument specifications are reported in Table 8.2. The non-invasive analyses were carried out directly on the surface of the artifacts by connecting the instruments to the BAC151® portable microscope, equipped with different lenses (20x, 40x, 80x) capable of focusing the signal with a diameter' spot of about 300 µm, 90 µm, 50 µm, and 20 µm, depending on the lens used. The microscope also allows the image acquisition of the analyzed areas through a video camera.

Table 8.2 Specifications of portable Raman spectrometers: Laser wavelength, laser power, spectrometer model, resolution and spectral range of acquisition.

Laser wavelength (nm)	Laser power (mW)	Spectrometer	Resolution (FWHM) (cm^{-1})	Spectral Range (cm^{-1})
785	270	BTC675N	6.39	65-3350
532	44	BWS465-532S	6.17	65-4200
1064	375	BTC284N	10.56	100-2500

Results

Raman spectroscopy was employed to perform a molecular characterization of the corrosion products present on the surface of the sculptures. The technique allows for the detection of both crystalline and amorphous or poorly crystalline phases and allows for the analysis of different spots and crystals. Several areas were analysed, chosen based on their morphology and color.

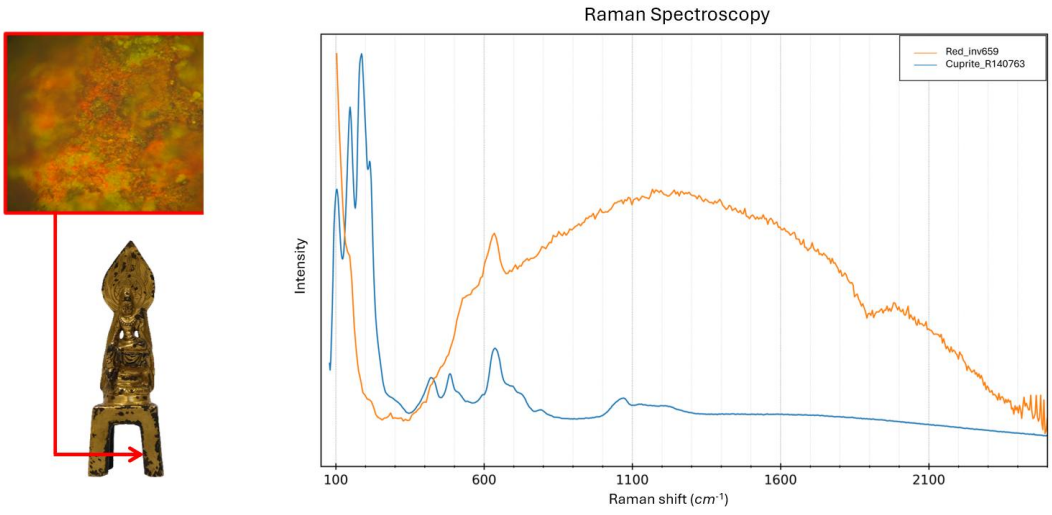

Figure 8.6 Raman spectra of artifact INV. 659 acquired in correspondence of reddish compared to the RRUFF reference (database RRUFF, R140763).

The technique is not straightforward, and not all the areas can be analysed on all artifacts since the fluorescence contribution could cover the peaks of interest.

The artifacts presented corrosion products of different aspects: red, green, and black areas.

The spectra of the reddish areas were consistent with the presence of cuprite, (Cu2O) (Figure 8.6), and cassiterite. The band at 202 (a shoulder), 217, 621, 285, 408 and 331 cm-1, clearly indicate the presence of cuprite. The presence of Cuprite was identified in the sculpture INV. 659 (Figure 8.6), 667, and 710. Another Cu oxide corrosion product, tenorite (CuO) and amorphous carbon [121], was identified (Figure 8.7). The spectrum was detected in correspondence with a black area on the artifact INV. 710, identified by the peaks at 291, 339, and 626 cm-1. The presence of tenorite was detected by comparison with the reference RRUFF database spectra (RRUFF ID: R120076).

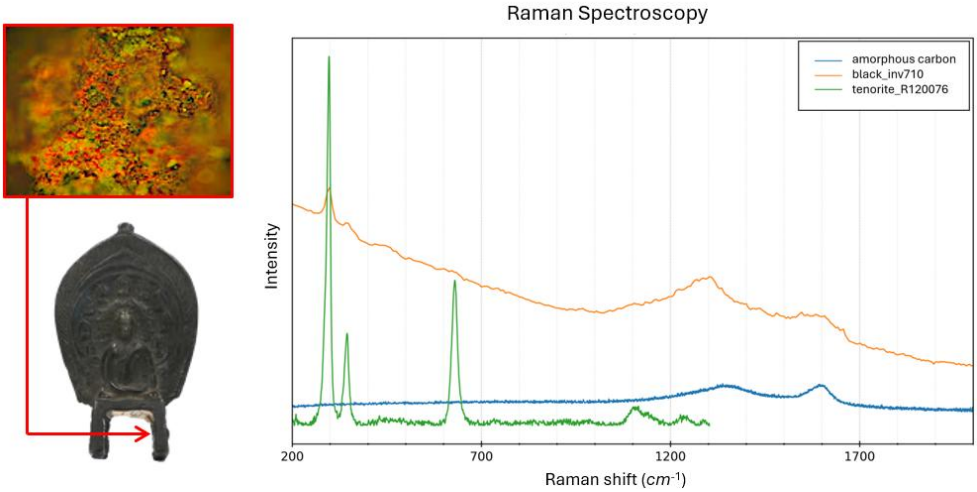

Figure 8.7 Raman spectra of the artifact INV. 710. Comparison of the tenorite combined with the amorphous carbon spectra acquired in correspondence with a black area with the RRUFF reference (database RRUFF, R120076).

In correspondence with the greenish areas, common copper corrosion patinas were identified: the peaks at 392, 485, and 974 cm-1 allow the identification of brochantite (Cu4SO4(OH)6) [122], and the major bands at 515, and 3348 cm-1, are associated with atacamite Cu2Cl(OH)3 [123], found in the sculpture INV. 625 and 650. In particular, from the analyses performed on the artifact INV. 667 the presence of atacamite was identified in co-existence with rouaite (Cu2(NO3)(OH)3), characterized by the mean peaks at 1322, and 3550 cm-1, shown in Figure 8.8. In particular, Rouaite owes its formation to the exposure of the metal surface to high heating [117], confirming the hypothesis of the fire-gilding technique. The amalgam was applied to the metal surface and then heated to complete the evaporation of mercury, resulting in a glossy and shiny surface [111].

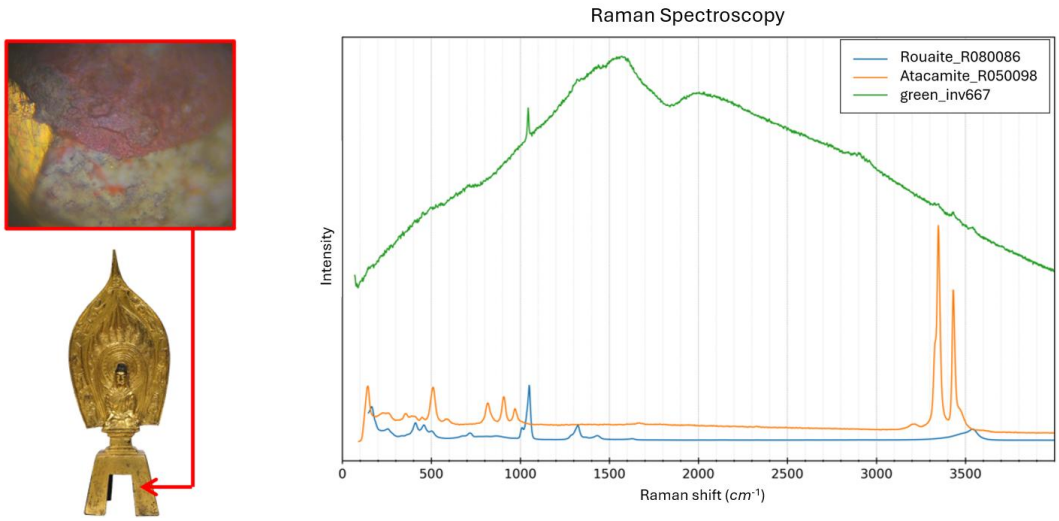

Figure 8.8 Raman spectra artifact INV. 667. Comparison of the rouaite in combination with atacamite spectra acquired in correspondence with a green area with the RRUFF references (database RRUFF, rouaite R080086, and atacamite R050098).

Another greenish copper-based corrosion patina detected is clinoatacamite (Cu2(OH)3Cl) [123]. It was identified by comparison with the RRUFF database spectra (R061066) shown in Figure 8.9, and characterized by the peaks at 521.19, 909, 969, and 3354 cm-1 [122]. In particular, it was detected in correspondence of the artifact INV. 708.

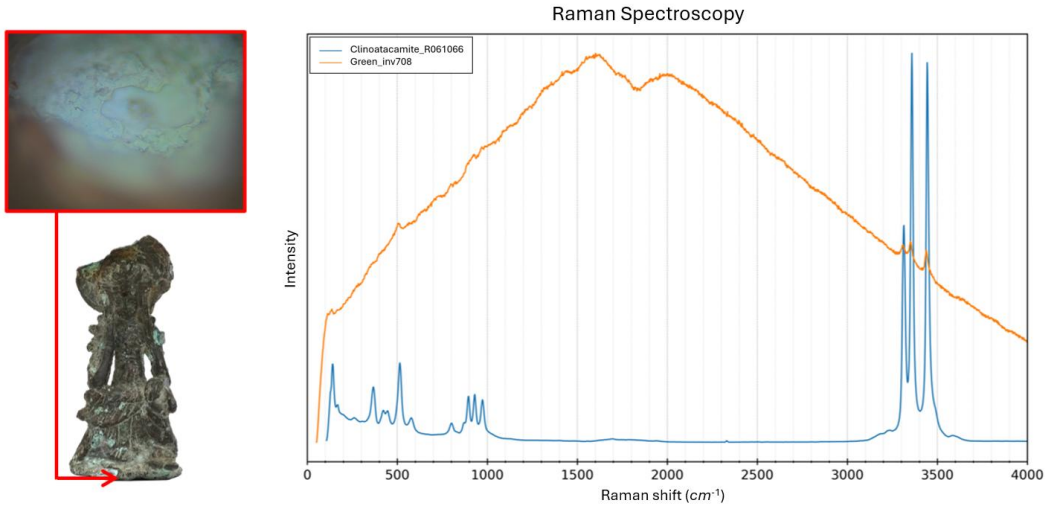

Figure 8.9 Raman spectra of the areas indicated in the optical images of the artifact INV. 708: Red area of the sculpture; Green area of the sculpture. For comparison purposes, spectra of cuprite from database RRUFF, R140763 and of clinoatacamite from database RRUFF, R061066; spectrum of amorphous carbon.

To summarize, Raman spectroscopy enabled the corrosion products identification as mainly copper oxides with small quantities of chlorides, hydroxy-chlorides, and copper sulfates, representing a good overall preservation status. The artifacts are generally in good condition, given the prevalence of stable corrosion products such as oxides and sulfates. The presence of corrosion products containing

chlorides was found only in some works, limited to some areas under analysis, for which monitoring in time to highlight the possible emergence of critical degradation processes for the preservation of the works themselves was recommended.

8.1.2.3 Photogrammetry

In this study, an experimental approach to photogrammetry is presented, aimed at integrating visible and UVL imaging into a single 3D digital model. In addition, to improve the reconstruction of these metal artifacts, characterised by reflective metal surfaces, the cross-polarization technique was employed. This approach allows to reconstruct a single mesh while VIS and UVL textures are generated.

For each shooting position, the acquisition is composed of three images recorded in the visible spectrum: in visible and polarized light (VIS and VIS-PL) to capture the maximum and minimum degree of reflection of the surface, and one in UVL. At first, the different datasets are aligned and then processed together to obtain the final model with its textures. In the case of the two datasets in visible light, a third texture called "specular map" was obtained in post-production The specular map is obtained by subtraction of the VIS-PL from the VIS textures and employed to modify the final surface appearance. The result is a replication of a correct degree of reflection, highlighting the characteristics of shiny materials.

Given the experimental approach, one of the artifacts, i.e. INV. 667, was acquired for preliminary purposes.

Images were acquired with a Canon EOS 6D camera with an image size of 5472 × 3648 pixels, 20.1 megapixels, and a CMOS full-frame sensor with a pixel size of 6.54 µm. The ISO working range is 100–6400. It is paired with a Canon EF 50mm f/1.8 II STM prime lens, which has a fixed focal length of 50mm, a maximum aperture of f/1.8, and a minimum aperture of f/22.

VIS light sources (Led panel 19.5 W CRI 95) and a UV lamps (3x Led 5 W centered at 365 nm) were employed, together with two polarisers, namely a Hoya HD Circular polarizer mounted on camera and a Linear polarizing sheet (20 x 30 cm) placed in front of the light source.

The camera was fixed on a tripod, and the object on a controlled rotating platform, with an acquisition distance of 1.5 m. In this way, the imaging acquisition allows the comparison and the images to overlap when acquired by the different multiband imaging techniques. Thanks to the rotating platform, the subject was acquired with a 5° step angle, resulting in 72 images for each rotation. In the end, 4 different rotations were acquired: 2 rotations with the subject in vertical position with the camera tilted at 15° and 30° angle, and 2 rotations with the sculpture horizontally placed with the camera tilted at 15° for each side (front and back view), for a total amount of 576 (288x2) images for the VIS and VIS-PL datasets. On the other hand, half of the images were taken for UVL imaging acquisitions, with a 10° step angle and 144 images to significally reduce the acquisition time, in fact, only the VIS and VIS-PL images were used for the 3D reconstruction. Instead, UVL photographs were used just for relative texture generation, replacing the visible ones after the generation of the two visible textures.

Figure 8.10 Acquisition strategy of the gilded sculpture INV. 667.represents the acquisition strategy of the artifact INV. 667, and Table 8.3 summarises the acquisition parameters.

Table 8.3 Parameters used during image acquisition.

Parameter	VIS	VIS-PL	UVL
Shutter speed	1s	5s	5s
Step angle	5°	5°	10°
Number of images	288	288	144
Image size	5472 x 3648	5472 x 3648	5472 x 3648
Image Format	RAW	RAW	RAW
Focal Length	50mm	50mm	50mm
Aperture	f/11	f/11	f/8
ISO	100	200	3200

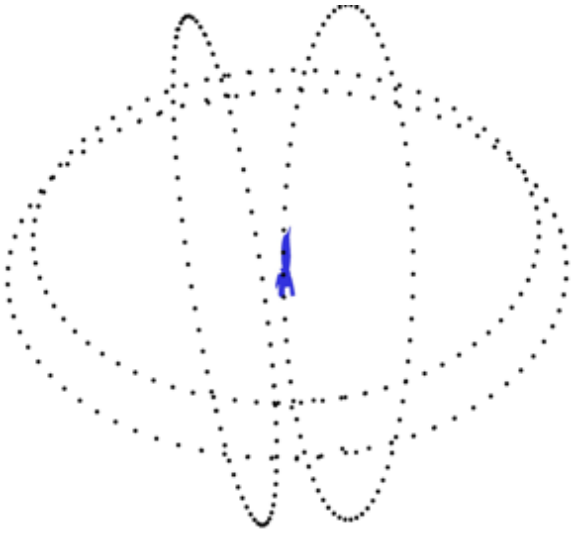

Figure 8.10 Acquisition strategy of the gilded sculpture INV. 667.

Results

The 3D model obtained by photogrammetry is a useful tool for documenting the conservation state of the artwork. This approach allows to obtain information relating to the specular aspect of the object, resulting in a more photorealistic model. It is noted that only one of the sculptures from the Auriti Collection was acquired (INV. 667), for pre-liminary purposes. The generated model of the artifact consists of 1,002,078 triangles and a texture with a resolution of 4076 x 4076 pixels. It is characterized by three different textures: the first one is the VIS texture (Figure 8.11a), modified by the specular map (Figure 8.11c) created by subtracting the polarized texture (Figure 8.11a) to the visible one (Figure 8.11b), and the third is the UVL texture (Figure 8.11d).

Details of the INV. 667 virtual replicas are shown in Figure 8.12 and Figure 8.13. It highlights details that are not easy to detect at a macroscopic level. In contrast, the UVL model provides information that cannot be observed with visible radiation; indeed, the combination of the UV wavelengths with photogrammetry highlights the exterior layers of the surface sculpture (Figure 8.13).

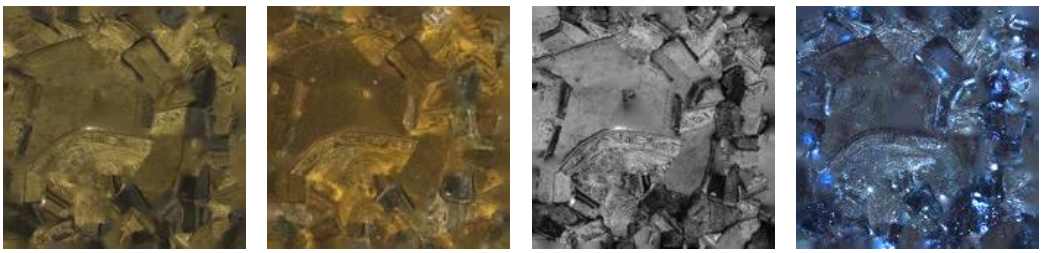

(a) (b) (c) (d)

Figure 8.11 Texture generated for the VIS and UVL 3D model: (a) Visible texture, (b) Polarized texture, (c) Specular Map, (d) Ultraviolet Luminescence texture.

In correspondence with the 3D visible light digital model, the presence of surface losses where the gilding is missing, signs of manufacturing or surface engravings, and corrosion patinas, are discriminated. However, the UV luminescence highlights a transparent and colorless protective coating, not visible to the naked eye and probably due to a thin protective layer applied in past restoration. In detail, the film was applied by brush and distributed in a not homogeneous way over the whole bronze surface. In addition, the presence of drips is denoted.

Figure 8.12 3D VIS model of the artifact INV. 667. Starting from left: front view, left view, right view, back view.

Figure 8.13 3D UVL model of the artifact INV.667. Starting from left: front view, left view, right view, back view.

8.2 Human remains of an Egyptian mummy from the Museo Egizio of Turin

The case study concerns an Egyptian mummy from the Roman Period, from the Museo Egizio in Turin (Italy). The mummy underwent conservation and restoration treatment at the Centro per la Conservazione e il Restauro dei Beni Culturali "*La Venaria Reale*". To enable the restoration activity, the cartonnage mask and the skull inside it, already detached from the body as a result of theft, were temporarily separated.

This activity was part of a broader collaborative project among the Centro Conservazione e Restauro "La Venaria Reale", the Museo Egizio of Turin, and the Politecnico di Torino. One of the objectives of the project was the design and fabrication of a custom-made support to ensure the correct repositioning of the skull within the mask. The support was developed in collaboration with RobinLab Studio, based on 3D models of the individual components (the skull, mandible, and mask) acquired through 3D scanning.

Within this framework, the present study focused on developing a 3D model of the skull using a low-cost, open-source photogrammetric system. The model was then compared to the reference 3D scan to assess the dimensional accuracy of the photogrammetric reconstruction. While 3D models of the skull, mask, and jaw were generated through photogrammetry, the dimensional comparison discussed below focuses exclusively on the skull. The purpose of this comparison was to verify whether photogrammetry can be used as a reliable alternative to 3D scanning for the creation of custom supports intended for exhibitions [59].

8.2.1 The archaeological remains

The case study examined is part of the collection of the Museo Egizio in Turin. The research was conducted in the context of the study and conservation of an Egyptian mummy (Figure 8.14), characterized by a painted linen shroud and a

gilded cartonnage mask. During the conservation process, the temporary removal of the cartonnage was required to allow the treatment of the inner bandages. The mummy's skull (Figure 8.15a), which had been separated from the bandages in the past, was discovered inside the mask (Figure 8.15b).

Figure 8.14 Remains of an Egyptian human (Provv. 0549) mummy with cartonnage mask and painted shroud of the Roman period (30 B.C.E. – 395 C.E.), from the Museo Egizio of Turin.

(a) (b)

Figure 8.15 The mummy's skull (a) and cartonnage mask (b)temporarily separated from the rest of the body during conservation and restoration activity.

The present study is part of a long lasting multisciplinary cooperation between the Politecnico di Torino, the Centro per la Conservazione ed il Restauro dei Beni Culturali *La Venaria Reale*, and the Museo Egizio of Turin. The main aim of the project was the creation of accurate virtual replicas of both the skull and the cartonnage, supporting the correct repositioning of the elements to design a custom support aimed at correct repositioning of the skull within the mask. Furthermore, the digital replica provided a valuable resource for anthropologists and scholars, facilitating future analyses and documentation of the organic remains.

The mummy, identified with the provisional inventory number Provv. 0549, assigned after the loss of the original documentation, lacks historical information regarding its conservation and acquisition. Based on stylistic analysis, it has been attributed to the Roman Period (30 B.C.E.–395 C.E.). The ensemble includes a human body wrapped in linen bandages, a gilded and painted cartonnage mask, and a painted linen shroud.

8.2.2 Photogrammetric 3D model comparison with Structured Light Scanner

Photogrammetry

The image acquisition setup consisted of a digital camera, visible light sources, and reference targets. A Fujifilm X-T30 camera equipped with an APS-C X-Trans CMOS 26.1 megapixel sensor was used in combination with a Minolta MC Rokkor-PF 50 mm f/1.7 fixed focal length lens. The detailed technical specifications of the camera and the lens are reported in Table 8.4. To optimize the quality of the 3D reconstruction, all image acquisition parameters and illumination conditions were kept constant throughout the process. The main camera parameters (shutter speed, ISO sensitivity, and aperture) were set, respectively, to 2.7 s, ISO 80, and f/22, while the focal length remained fixed. Maintaining these stable acquisition settings is essential to ensure photogrammetric accuracy and to reduce image variability.

The artifact was positioned on a white background and surrounded by reference targets to support image alignment and scaling. The camera was moved around the object at two different heights to capture images from multiple viewpoints, with each image taken at approximately every 30° steps.

Table 8.4 Camera and prime lens specifications; Table from [59].

Camera: Fujifilm XT-30	
Image size (pixels)	6240 x 4160
Effective megapixels	26
Sensor size, type	23.5 mm x 15.6 mm (APS-C) X-Trans CMOS
Pixel size (μm)	4.94
ISO range	160 – 12800

Prime lens: Minolta MC Rokkor-PF 50 mm *f*/1.7	
Focal length	50 mm
Minimum aperture	*f*/1.7
Maximum aperture	*f*/16
Focus type	Manual
Type	Prime

The same procedure was repeated after turning the skull to document the opposite side. Additional close-up photographs were acquired to capture details of the inner surface. In total, 48 images were collected with the camera placed at an average distance of about 100 cm from the object. A tripod was used to stabilize the camera and prevent movement during the shooting, ensuring the images alignment. A 24-patches X-Rite ColorChecker Classic Mini® was included in the scene to allow subsequent color and exposure calibration.

Figure 8.16 Acquisition setup for the reconstruction of the skull's 3D model by photogrammetry; Figure from [59].

The 3D reconstruction was performed using AliceVision® Meshroom. This software provided the generation of a textured 3D model in combination with the CCTag system, enabling the scaling of the model to real-world dimensions. This functionality enhances the dimensional reliability of the reconstructed model, particularly in metrological and heritage documentation applications where scale accuracy is crucial. Figure 8.16 shows the acquisition setup, including the placement of the reference targets at known distances.

The reconstruction process was carried out on a workstation equipped with a 12th Gen Intel® Core™ i9-12900KF (3.19 GHz) processor, 64 GB RAM, and an NVIDIA GeForce RTX 3080 GPU, running on Ubuntu 22.04.3 LTS.

3D Scanner

The 3D scanning acquisition was carried out using an Artec Space Spider device (Artec 3D, Luxembourg). This instrument is a high-resolution 3D scanner that employs blue LED light technology. According to the manufacturer's specifications, the system operates effectively within a working distance range of 0.2 – 0.3 m and is capable of capturing fine geometric details of both small and medium-sized objects. The scanner provides a spatial resolution of up to 0.1 mm and a point accuracy of up to 0.05 mm, and it is equipped with a 1.3-megapixel camera for texture acquisition.

During data acquisition, the scanner was manually moved around the object (Figure 8.17) at an average distance of approximately 30 cm. Data collection and processing were performed using Artec Studio Professional (version 18.0), the proprietary software for managing scanning parameters, alignment, and model reconstruction.

The resulting 3D model was processed on a workstation equipped with a 12th Gen Intel® Core™ i9-12900KF (3.19 GHz) processor, 128 GB RAM, and an NVIDIA GeForce RTX 3090 GPU, running on a 64-bit Windows operating system.

Figure 8.17 Acquisition setup Acquisition setup for the reconstruction of the skull's 3D model by 3D scanning.

Results

A metric assessment of the 3D model quality was carried out by comparing the virtual replicas obtained through photogrammetry and 3D scanning. The analysis focused on evaluating the distance map and calculating statistical parameters, including the mean distance, standard deviation, and RMS error, between the two models generated using different acquisition systems.

The evaluation was performed using CloudCompare. For this study, a cloud-to-mesh distance computation was applied, considering the 3D scanner model as the reference dataset due to its higher dimensional accuracy. Prior to distance computation, the two models were roughly aligned by selecting corresponding surface points to bring them into the same coordinate system. Since the photogrammetric pipeline in Meshroom enables scaling based on reference targets included in the acquisition scene, no further scaling was required. The alignment was then refined using the ICP algorithm, without adjusting the scale factor.

Both photogrammetry and 3D scanning successfully produced accurate virtual replicas of the skull, capturing its geometry with varying levels of mesh complexity. The 3D scanner generated a model with a higher level of detail, consisting of 2,981,857 vertices, 8,930,151 edges, and 5,948,252 faces. In contrast, the photogrammetric model included 1,029,552 vertices, 3,087,392 edges, and 2,057,976 faces.

However, the photogrammetric model was characterized by a better texture quality. As illustrated in Figure 8.18b and Figure 8.19b, the photogrammetric reconstruction displayed finer surface details and a more photo-realistic appearance compared to the texture acquired by the 3D scanner.

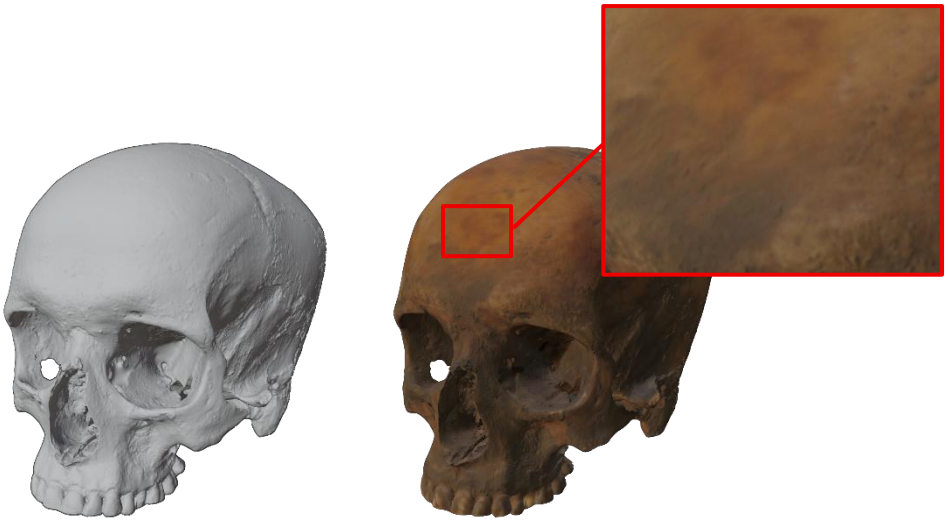

(a) (b)

Figure 8.18 3D models of the skull of the Museo Egizio of Turin by 3D scanner: (a) mesh; (b) textured 3D model; adapted from [59].

(a) (b)

Figure 8.19 3D models of the skull of the Museo Egizio of Turin by photogrammetry: (a) mesh; (b) textured 3D model; adapted from [59].

This difference can be attributed to the higher image quality of the digital camera used for photogrammetry relative to the scanner's built-in camera. This observation highlights one of the main advantages of photogrammetry in the detailed documentation of surface textures, which is particularly relevant in the field of cultural heritage.

The comparison results are presented in Figure 8.20a as a color-coded distance map, where the deviations between the two models are expressed in millimeters. Positive values indicate areas where the photogrammetric surface lies above the reference model, while negative values represent regions below it. Green areas correspond to minimal discrepancies and therefore higher accuracy.

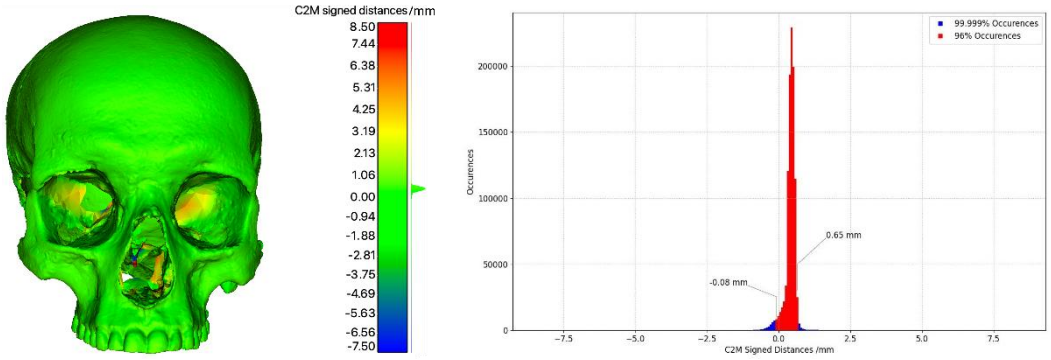

(a) (b)

Figure 8.20 (a) Distance map between the 3D scanner and photogrammetry models (mm); (b): Histograms of computed distances (mm) from the 3D surface comparison computed in CloudCompare; Figure from [59].

The histogram of the computed distances (Figure 8.20b) shows that all measured deviations fall within the 99.999% confidence interval, ranging from -7.75 mm to 8.45 mm, with a mean distance of 0.41 mm, a standard deviation of 0.25 mm, and an RMS distance of 0.48 mm.

Notably, 96% of the points exhibited deviation values between -0.08 mm and 0.65 mm, confirming a high degree of consistency between the two datasets. The distance map revealed that the largest discrepancies occur mainly along sharp edges and in deeper cavities of the skull, such as the eye orbits, nasal and oral cavities, and within the cranial cavity. These variations are likely due to reduced illumination in these areas, resulting in limited image detail and lower reconstruction density in the photogrammetric model.

Overall, despite localized deviations in geometrically complex regions, the results demonstrated that photogrammetry is a reliable, cost-effective, and non-invasive method for 3D documentation. Its high-quality texture reproduction and adequate dimensional accuracy make it particularly suitable for applications in cultural heritage, where detailed surface representation and visual realism are essential for documentation, study, and archiving purposes.

8.3 Polychrome wooden sculptures from the Museo di Arte Orientale of Turin

8.3.1 The artifacts

"Objects pertaining to Buddhist visual and material culture are often studied in relation to their circulation from India throughout the rest of Asia, while, to date, little attention has been paid to understanding their westward migration even though numerous examples are currently preserved in both public and private collections in Europe and the United States. Originating from different geographical areas and cultural contexts within the Asian continent, many of these artifacts traveled to Europe during the last few centuries to be sold as trade commodities and pieces for the art market. As a result of this transition, they lost any devotional value or

purpose in favor of a specific aesthetic sensitivity that was typically adapted to Western taste to appeal to collectors." [124].

The present study is part of a multidisciplinary collaboration among the Politecnico di Torino, the Centro per la Conservazione e il Restauro dei Beni Culturali "*La Venaria Reale*" (CCR), and the Museo di Arte Orientale (MAO) in Turin. It focuses on two of a group of seven polychrome wooden sculptures from the MAO collection, generally catalogued as Chinese works dating to the late Ming – early Qing dynasties (16th–18th centuries), based primarily on stylistic and iconographic criteria. The entire group of seven sculptures underwent an in-depth technical study and conservation treatment at the CCR, with the results published in [124].

In particular, two of these sculptures were documented using photogrammetry, following an analytical approach aimed at creating multi-band 3D models. Specifically, the artifacts examined are INV. 451, representing a Bodhisattva from the Shanxi or Shaanxi region, dated to the 16th century, and INV. 454, representing a Lohan (Arhat) from China, also dated to the 16th century.

The outcomes of this research, together with the studies carried out by the CCR, were presented in the exhibition "Buddha10. A Fragmented Display on Buddhist Visual Evolution", held at the MAO from October 2022 to September 2023. Within this exhibition, all the sculptures were treated, except for Inv. 450, which is iconographically specular to Inv. 451. This curatorial decision allowed visitors to directly compare a conserved sculpture with its untreated counterpart, the latter being documented through a 3D multi-band model. Part of the conservation process was also performed within the exhibition space, offering visitors a unique opportunity to observe the delicate conservation and restoration activity work in progress.

8.3.2 3D models by Photogrammetry combined with Multi-band imaging

To investigate the artifacts and integrate both radiometric and geometric data into a unique 3D model, a specific acquisition setup was employed. For the aim of this study, the camera was fixed on a tripod, while the object was placed on a turntable. This configuration ensured that the relative orientation between the camera and the object remained constant throughout the acquisition process. Consequently, images acquired using different multi-band imaging techniques could be compared and accurately overlapped.

Therefore, the employed set-up was composed of several elements: a modified digital camera, a rotating platform, radiation sources, and filters.

For this study, an off-the-shelf digital camera modified to be sensitive to radiation in the range between 200 nm and 1100 nm has been employed. To this aim, the IR-blocking hot mirror and a transparent UVIR cut filter were removed from the sensor of a mirrorless camera, i.e., the Fujifilm XT-30 (APS-C X-Trans CMOS4 sensor). The camera was coupled with a prime lens with a fixed focal

length (Minolta MC Rokkor-PF 50mm f/1.7). Table 8.5 reports the specifications of the camera and lens employed, respectively.

Table 8.5 Camera and prime lens specifications.

Camera: Fujifilm XT-30	
Image size (pixels)	4608 x 3072
Effective megapixels	26.1
Sensor size, type	23.5 mm x 15.6 mm (APS-C) X-Trans CMOS 4
Pixel size (µm)	4.94
ISO range	160 – 12800

Prime lens: Minolta MC Rokkor-PF 50 mm *f*/1.7	
Focal length	50 mm
Minimum aperture	*f*/1.7
Maximum aperture	*f*/16
Focus type	Manual
Type	Prime

The artifacts were placed on a precision rotation platform, that can continuously rotate from 0° to 360°, enabling accurate positioning of the artifacts (Figure 8.21). In Table 8.6 the acquisition parameters are shown.

Figure 8.21 Acquisition setup the Lohan INV. 454 (left), and the Bodhisattva INV. 450 (right).

Several lighting sources and filters were employed, as required by the specific MBI technique. For VIS images, two halogen lamps (800 W) were placed symmetrically at 45° in respect to the object's position. Furthermore, the HOYA UV&IR Cut visible bandpass filter was employed to limiting the recording in the visible region (400–700 nm), together with an IR cut filter. For UVL and UVR images, two 365 nm UV LED sources (3000 mW AC/battery operated) were used. For UVL images, the HOYA UV&IR Cut visible bandpass filter was employed,

while for UVR images, a Baader U-filter, with a transmission bandwidth of 60 nm (320–380 nm), was exploited to exclude the signal in the visible and IR regions (400–1100 nm). A 24-color X-Rite ColorChecker Classic Mini® was included in the scene to perform chromatic and exposure correction.

Table 8.6 Parameters employed during the acquisitions.

Parameter	VIS	IRR	UVL	UVR
Shutter speed	1s	1s	20s	20s
Step angle	15°			
Image size	6240 x 4160			
Image Format	RAW			
Focal Length	50 mm			
Aperture	f/16			
ISO	200			

For the reconstruction of the 3D model, Meshroom was employed. The pipeline can be used with the default setting by the user, but it can also be modified and configured to meet the user and project needs. Indeed, the pipeline comprises several processing blocks for every reconstruction step.

To create a unique 3D model that carries morphological and geometrical data from photogrammetry and radiometric data from MBI techniques, the pipeline was set as follows. The mesh and point cloud were generated using the embedded default pipeline, starting from the VIS images. Then the point cloud and mesh generated with the above-mentioned step were employed to re-texture the VIS 3D model with the images from UVL, UVR, UVR-FC, IRR, and IRR-FC techniques. In particular, the dense scene node is duplicated, and it is recomputed with a different set of images, i.e., UVL, UVR, UVR-FC, etc. Before starting the 3D reconstruction process, it is necessary to align the images acquired in the different spectral bands, since each wavelength focuses the image on a slightly different plane. This effect results from the use of a lens not optimized for multiband imaging, such as the one employed in this study. The alignment was manually performed in Photoshop, using the VIS dataset as the reference for all other bands.

It is worth underlying that this was possible since all the images were acquired by keeping the relative orientation of the camera and object stable during the acquisition. Consequently, this approach leads to the generation of a multi-band 3D model, which stores different data, with the advantage of keeping all the information in a single co-ordinate system, allowing one to navigate and compare the results as superimposed layers.

Results

Ultraviolet (UV) radiation is useful for highlighting the more superficial layers of an artifact, such as transparent varnishes not visible to the naked eye, and for the identification of non-original pigments.

UV radiation was employed to create the 3D models in UV luminescence (UVL), UV reflectography (UVR), and UV false color (UV-FC).

(a) (b)

Figure 8.22 UVL 3D model Bodhisattva INV.450, front (a) and back view (b).

The digital 3D model obtained under UVL illumination revealed several noteworthy features of the surface materials and their distribution. First, it highlighted the presence of a film-forming layer uniformly applied across the entire surface, with the exception of the base area, which exhibited low luminescence intensity (Figure 8.22). Additionally, preparatory layers were visible, showing a light-yellow luminescence that clearly distinguished them from the surrounding materials (Figure 8.23b). Finally, the model made it possible to identify retouched areas executed with non-original pigments, recognizable by their dark luminescence response (Figure 8.23a).

(a) (b)

Figure 8.23 UVL 3D model Lohan INV.454, front (a) and right view (b).

The UVL 3D model of the Lohan INV. 454 revealed several distinct surface features related to the materials and interventions present on the artifact. A bluish

luminescence was visible across the entire surface, suggesting the presence of a synthetic material, likely applied during a previous restoration campaign. In addition, areas exhibiting a dark luminescence response were observed, corresponding to pictorial retouching areas (Figure 8.23a). Finally, luminescence areas with a red–orange hue were discernible, indicating the presence of a material belonging to the lacquer family, different in composition from the original one (Figure 8.23b).

IR radiation could penetrate the material and therefore see what was underneath the pictorial layer, highlighting features such as the preparatory drawing, pentimenti, retouching, and non-original details.

Infrared radiation was used for the creation of IRR and IRR-FC 3D models. Therefore, it was possible to identify the areas with retouchings of the polychrome surface: indeed, the retouchings were carried out with materials that have the same appearance in visible light but different infrared absorption, due to their different chemical composition.

(a) (b)

Figure 8.24 IRR (a) and IRR-FC (b) 3D model Bodhisattva INV.450.

(a) (b) (c)

Figure 8.25 Detail of retouching on the 3D model of Bodhisattva INV.450 in VIS (a), IRR (b), and IRR-FC (c).

The 3D model of the Bodhisattva INV.450 in IRR highlights the presence of gaps in the pictorial film distinguished by a lighter shade of gray; in this case, the

gaps were visible even if affected by pictorial retouching (Figure 8.24a and Figure 8.25b). The retouches were more evident in the 3D model in IRR and in IRR-FC: the area affected by pictorial retouching presented a red color response, unlike the greenish hue distinctive of the original polychromy (Figure 8.25c).

The 3D model of the Lohan (Inv. 454), integrated with the results of multi-band imaging, allowed not only to identify the presence of surface film-forming layers but also to examine their distribution across the artifact. The IRR-FC model revealed a purplish hue on the monk's robe, indicating an unevenly distributed surface layer that tended to accumulate in areas of greater chromatic intensity (Figure 8.26b). Similarly, the IRR model highlighted the presence of gaps in the pictorial film (Figure 8.26a) and areas of retouching, which appear even more distinctly in the IRR-FC 3D model (Figure 8.26c).

(a) (b) (c)

Figure 8.26 3D model of Lohan INV.454 in VIS (a), IRR (b), and IRR-FC (c).

Chapter 9

Conclusions

Photogrammetry and multi-band imaging have become widely adopted techniques in the field of Cultural Heritage for the documentation and study of artworks. Nevertheless, they are most often applied independently, each providing distinct and complementary types of information. In recent years, there has been growing interest in integrating these approaches to combine spatial and radiometric data within a single three-dimensional model. Such integration enables the extraction of information not only related to the geometry and morphology of the objects, but also to information about their constituent materials.

Within the broader context of preventive conservation, whose goal is to prevent the onset of degradation and prolong the lifetime of cultural assets, this dissertation presented the use of photogrammetry as an active tool for deformation monitoring over time. The proposed methodology supports conservation and preservation strategies by enabling the assessment of structural variations occurring in artworks due to environmental fluctuations. The study focused on wooden and painted wooden artifacts, represented by two custom-made samples that underwent controlled thermo-hygrometric aging to induce measurable deformation phenomena, such as cracking, warping, and shrinkage.

Before the monitoring of the samples, the acquisition setup was validated using a custom dimensional reference object. This reference was measured with several high-precision instruments, including a Coordinate Measuring Machine and a laser scanner, each characterized by a different level of measurement uncertainty. The results confirmed the suitability of photogrammetry, when properly calibrated and scaled, for producing a reliable virtual replica.

Subsequently, the monitoring phase was carried out on the wooden and painted wooden samples, acquired before and after the induced aging process, using both photogrammetry and laser scanning. The photogrammetric workflow was implemented across different spectral bands (VIS, VIS-PL, IRR, UVL, and UVR) to evaluate the influence of wavelength on reconstruction quality. The comparative analysis demonstrated that the proposed multi-band photogrammetric approach

allowed for the detection and quantification of geometric variations comparable to those obtained with the laser scanner.

In addition to the experimental validation and monitoring studies, several case studies were presented to illustrate the versatility of photogrammetry and multi-band imaging in real conservation contexts.

- A set of gilded and non-gilded bronze sculptures from the Museo delle Civiltà (MuCiv)in Rome was analyzed through a diagnostic campaign aimed at identifying alloy composition and gilding techniques. In this context, an innovative workflow for acquiring reflective metallic surfaces using cross-polarization was proposed, successfully enabling the generation of accurate 3D virtual replicas.
- Within a collaboration with the Museo Egizio of Turin and the Centro per la Conservazione e il Restauro dei Beni Culturali (CCR) "*La Venaria Reale*", a dimensional comparison between photogrammetry and laser scanning was performed on an Egyptian mummy skull, with the goal of designing a custom exhibition support based on the 3D virtual reconstruction.
- Finally, a group of Chinese polychrome wooden sculptures from the Museo di Arte Orientale (MAO) of Turin was digitized using multi-band photogrammetry as part of a restoration project conducted at the CCR. The resulting 3D models served not only for conservation purposes but also for the creation of an innovative exhibition concept based on interactive visualization.

The results obtained throughout this research confirm that photogrammetry, supported by multi-band imaging, represents a powerful, versatile, and non-invasive tool for both the documentation and monitoring of cultural heritage artifacts. It can effectively integrate geometric accuracy with material information, supporting both scientific investigation and public dissemination. Moreover, its adaptability to different materials and acquisition contexts makes it a valuable complement to traditional techniques.

Further developments in this field should aim to enhance the automation of the photogrammetric workflow, thereby reducing acquisition and post-processing times. The integration of artificial intelligence represents one of the most promising directions for research, particularly for the automated monitoring of the preservation state of artworks over time. Additionally, future studies could extend the metrological validation to a broader range of materials and surface finishes, as well as include long-term environmental monitoring campaigns on real artifacts.

Another promising direction for future research concerns the implementation of automated image segmentation techniques as a support for the mapping of material distribution and the assessment of preservation conditions. Traditionally, this process is manually performed by conservators to quantify the extent of surface coverage by different materials or degradation patterns. Integrating automated segmentation within photogrammetric workflows could significantly streamline this task, improving efficiency and reducing subjectivity in the documentation of cultural heritage objects.

The strength of photogrammetry lies in its ability to combine multiple imaging techniques into a single integrated 3D model. This multidimensional approach not only enriches the documentation and analysis of artworks but also plays an increasingly important role in preventive conservation, restoration planning, and even museological dissemination, enabling the creation of innovative exhibitions and interactive experiences that bridge scientific research and public engagement.

References

[1] F. I. Apollonio, F. Fantini, S. Garagnani, and M. Gaiani, 'A Photogrammetry-Based Workflow for the Accurate 3D Construction and Visualization of Museums Assets', *Remote Sensing*, vol. 13, no. 3, p. 486, Jan. 2021, doi: 10.3390/rs13030486.

[2] L. E. Sebar, S. Grassini, M. Parvis, and L. Lombardo, 'A low-cost automatic acquisition system for photogrammetry', in *2021 IEEE International Instrumentation and Measurement Technology Conference (I2MTC)*, Glasgow, United Kingdom: IEEE, May 2021, pp. 1–6. doi: 10.1109/I2MTC50364.2021.9459991.

[3] F. Di Iorio *et al.*, 'Violins Unveiled: A Photogrammetric Framework Integrating Multiband and Spectroscopic Data for In-Depth Examination of Two Musical Instruments', *Sensors*, vol. 25, no. 11, p. 3278, May 2025, doi: 10.3390/s25113278.

[4] L. E. Sebar, E. Angelini, S. Grassini, M. Parvis, and L. Lombardo, 'A trustable 3D photogrammetry approach for cultural heritage', in *2020 IEEE International Instrumentation and Measurement Technology Conference (I2MTC)*, Dubrovnik, Croatia: IEEE, May 2020, pp. 1–6. doi: 10.1109/I2MTC43012.2020.9129480.

[5] I. Aicardi, F. Chiabrando, A. Maria Lingua, and F. Noardo, 'Recent trends in cultural heritage 3D survey: The photogrammetric computer vision approach', *Journal of Cultural Heritage*, vol. 32, pp. 257–266, July 2018, doi: 10.1016/j.culher.2017.11.006.

[6] A. Bovero *et al.*, 'Precettoria of Sant'Antonio di Ranverso, an integrated approach for the study and monitoring of the Jaquerian painting cycles. The process for the definition, implementation and verification of conservation strategies'.

[7] F. Menna, E. Nocerino, D. Morabito, E. M. Farella, M. Perini, and F. Remondino, 'AN OPEN SOURCE LOW-COST AUTOMATIC SYSTEMFOR IMAGE-BASED 3D DIGITIZATION', *Int. Arch. Photogramm. Remote Sens. Spatial Inf. Sci.*, vol. XLII-2/W8, pp. 155–162, Nov. 2017, doi: 10.5194/isprs-archives-XLII-2-W8-155-2017.

[8] F. Remondino, 'Heritage Recording and 3D Modeling with Photogrammetry and 3D Scanning', *Remote Sensing*, vol. 3, no. 6, pp. 1104–1138, May 2011, doi: 10.3390/rs3061104.

[9] F. Di Iorio *et al.*, 'The Use of Virtual Reflectance Transformation Imaging (V-RTI) in the Field of Cultural Heritage: Approaching the Materiality of an Ancient Egyptian Rock-Cut Chapel', *Applied Sciences*, vol. 14, no. 11, p. 4768, May 2024, doi: 10.3390/app14114768.

[10] F. Remondino and S. Campana, Eds, *3D Recording and Modelling in Archaeology and Cultural Heritage: Theory and best practices: Theory and best practices*. Ann Arbor, MI: University of Michigan Press, 2014. doi: 10.30861/9781407312309.
[11] M. Pieraccini, G. Guidi, and C. Atzeni, '3D digitizing of cultural heritage', *Journal of Cultural Heritage*, vol. 2, no. 1, pp. 63–70, Jan. 2001, doi: 10.1016/S1296-2074(01)01108-6.
[12] L. Gomes, O. Regina Pereira Bellon, and L. Silva, '3D reconstruction methods for digital preservation of cultural heritage: A survey', *Pattern Recognition Letters*, vol. 50, pp. 3–14, Dec. 2014, doi: 10.1016/j.patrec.2014.03.023.
[13] M. Carmeliti and C. E. Catalano, 'CRMrp: An ontology to support the digital documentation of the conservation and restoration practice', *Journal of Cultural Heritage*, vol. 73, pp. 443–453, May 2025, doi: 10.1016/j.culher.2025.04.021.
[14] P. McInerney and B. O'Neill, 'The Art of Memory: Archiving Street Art using the CIDOC Conceptual Reference Model', *IFAC-PapersOnLine*, vol. 58, no. 3, pp. 357–362, 2024, doi: 10.1016/j.ifacol.2024.07.177.
[15] H. Papworth, A. Ford, K. Welham, and D. Thackray, 'Assessing 3D metric data of digital surface models for extracting archaeological data from archive stereo-aerial photographs', *Journal of Archaeological Science*, vol. 72, pp. 85–104, Aug. 2016, doi: 10.1016/j.jas.2016.05.005.
[16] Q. Chen, T.-N. Chen, Z.-Y. Ouyang, and X.-Y. Wang, 'Virtual reconstruction of Wanfoge in Beijing Zhihua Temple', *Journal of Cultural Heritage*, vol. 73, pp. 382–392, May 2025, doi: 10.1016/j.culher.2025.04.016.
[17] E. Siotto and P. Cignoni, 'Digital methods and techniques for reconstructing and visualizing ancient 3D polychromy – An overview', *Journal of Cultural Heritage*, vol. 68, pp. 59–85, July 2024, doi: 10.1016/j.culher.2024.05.002.
[18] S. Hermon, R. Orabi, V. Vassallo, M. Polig, J. A. MacGillivray, and J. Driessen, 'The death and the (digital) re-birth of a god – 3D virtual refitting of the Palaikastro Kouros', *Journal of Cultural Heritage*, vol. 68, pp. 99–106, July 2024, doi: 10.1016/j.culher.2024.05.011.
[19] L. E. Sebar *et al.*, 'In-situ multi-analytical study of ongoing corrosion processes on bronze artworks exposed outdoors', *Acta IMEKO*, vol. 10, no. 1, pp. 241–249, 2021.
[20] B. Li, Y. L. Lim, and W. Li, 'Systematic review: a bibliometric analysis of building technology and its potential applications to artificial intelligence in the field of cultural heritage conservation from 2013 to 2023', *Journal of Asian Architecture and Building Engineering*, pp. 1–23, Feb. 2025, doi: 10.1080/13467581.2025.2467251.
[21] F. Remondino and A. Rizzi, 'Reality-based 3D documentation of natural and cultural heritage sites—techniques, problems, and examples', *Appl Geomat*, vol. 2, no. 3, pp. 85–100, Sept. 2010, doi: 10.1007/s12518-010-0025-x.
[22] G. Pavlidis, A. Koutsoudis, F. Arnaoutoglou, V. Tsioukas, and C. Chamzas, 'Methods for 3D digitization of Cultural Heritage', *Journal of Cultural Heritage*, vol. 8, no. 1, pp. 93–98, Jan. 2007, doi: 10.1016/j.culher.2006.10.007.
[23] Y. Bok, Y. Jeong, D.-G. Choi, and I. S. Kweon, 'Capturing Village-level Heritages with a Hand-held Camera-Laser Fusion Sensor', *Int J Comput Vis*, vol. 94, no. 1, pp. 36–53, Aug. 2011, doi: 10.1007/s11263-010-0397-8.
[24] A. Muñoz-Muñoz *et al.*, 'Application of photogrammetry and laser scanner on the Bronze Age structures of the Castillejos de Luna cist tomb necropolis

(Pizarra, Spain)', *Virtual Archaeol. Rev.*, vol. 14, no. 29, pp. 26–44, July 2023, doi: 10.4995/var.2023.19126.
[25] P. Tysiac, A. Sieńska, M. Tarnowska, P. Kedziorski, and M. Jagoda, 'Combination of terrestrial laser scanning and UAV photogrammetry for 3D modelling and degradation assessment of heritage building based on a lighting analysis: case study—St. Adalbert Church in Gdansk, Poland', *Herit Sci*, vol. 11, no. 1, p. 53, Mar. 2023, doi: 10.1186/s40494-023-00897-5.
[26] T. Schenk, 'Elements of Analytical Photogrammetry', in *Introduction to Photogrammetry*, 2005.
[27] T. Sheehan and A. M. Zervigón, Eds, *Photography and its origins*. London New York: Routledge Taylor & Francis Group, 2015. doi: 10.4324/9781315740096.
[28] M. Cartolari and M. Visentin, Eds, *Il restauro per immagini: fotografia e restauro dall'Ottocento a oggi*. in Fonti e testi. Raccolta di archeologia e storia dell'arte. Udine: Forum, 2022.
[29] F. Stanco, S. Battiato, and G. Gallo, *Digital Imaging for Cultural Heritage Preservation: Analysis, Restoration, and Reconstruction of Ancient Artworks*, 1st edn. CRC Press, 2017. doi: 10.1201/b11049.
[30] M. Magnani, M. Douglass, W. Schroder, J. Reeves, and D. R. Braun, 'The Digital Revolution to Come: Photogrammetry in Archaeological Practice', *Am. Antiq.*, vol. 85, no. 4, pp. 737–760, Oct. 2020, doi: 10.1017/aaq.2020.59.
[31] K. Kraus, *Photogrammetry: Geometry from Images and Laser Scans*, illustrata edn, vol. 1. Walter de Gruyter, 2011.
[32] M. M. Morita, D. A. Loaiza Carvajal, I. L. González Bagur, and G. M. Bilmes, 'A combined approach of SFM-MVS photogrammetry and reflectance transformation imaging to enhance 3D reconstructions', *Journal of Cultural Heritage*, vol. 68, pp. 38–46, July 2024, doi: 10.1016/j.culher.2024.05.008.
[33] C. Dostal and K. Yamafune, 'Photogrammetric texture mapping: A method for increasing the Fidelity of 3D models of cultural heritage materials', *Journal of Archaeological Science: Reports*, vol. 18, pp. 430–436, Apr. 2018, doi: 10.1016/j.jasrep.2018.01.024.
[34] L. Es Sebar *et al.*, '3D Multispectral Imaging for Cultural Heritage Preservation: The Case Study of a Wooden Sculpture of the Museo Egizio di Torino', *Heritage*, vol. 6, no. 3, pp. 2783–2795, Mar. 2023, doi: 10.3390/heritage6030148.
[35] M. Rahrig, M. Á. Herrero Cortell, and J. L. Lerma, 'Multiband Photogrammetry and Hybrid Image Analysis for the Investigation of a Wall Painting by Paolo de San Leocadio and Francesco Pagano in the Cathedral of Valencia', *Sensors*, vol. 23, no. 4, p. 2301, Feb. 2023, doi: 10.3390/s23042301.
[36] A. Frost, S. Mirashrafi, C. Molina Sánchez, D. Vacas-Madrid, E. Rodriguez Millan, and L. Wilson, 'Digital Documentation of Reflective Objects: A Cross-Polarised Photogrammetry Workflow for Complex Materials', in *3D Reasearch and Challanges in Cultural Heritage III: Complexity and Quality in Digitisation*, vol. 13125, Cham: Springer International Publishing, 2023, pp. 131–156. [Online]. Available: https://link.springer.com/10.1007/978-3-031-35593-6
[37] R. A. Galantucci, A. Musicco, C. Verdoscia, and F. Fatiguso, 'Machine Learning for the Semi-Automatic 3D Decay Segmentation and Mapping of Heritage Assets', *International Journal of Architectural Heritage*, vol. 19, no. 3, pp. 389–407, Mar. 2025, doi: 10.1080/15583058.2023.2287152.

[38] E.-M. Papia and A. Kondi, ‘Quantifying subtle color transitions in Mark Rothko’s abstract paintings through K-means clustering and Delta E analysis’, *Journal of Cultural Heritage*, vol. 72, pp. 194–204, Mar. 2025, doi: 10.1016/j.culher.2025.02.005.
[39] S. Yang, M. Hou, and S. Li, ‘Three-Dimensional Point Cloud Semantic Segmentation for Cultural Heritage: A Comprehensive Review’, *Remote Sensing*, vol. 15, no. 3, p. 548, Jan. 2023, doi: 10.3390/rs15030548.
[40] R. Pierdicca *et al.*, ‘Point Cloud Semantic Segmentation Using a Deep Learning Framework for Cultural Heritage’, *Remote Sensing*, vol. 12, no. 6, p. 1005, Mar. 2020, doi: 10.3390/rs12061005.
[41] F. Matrone *et al.*, ‘A BENCHMARK FOR LARGE-SCALE HERITAGE POINT CLOUD SEMANTIC SEGMENTATION’, *Int. Arch. Photogramm. Remote Sens. Spatial Inf. Sci.*, vol. XLIII-B2-2020, pp. 1419–1426, Aug. 2020, doi: 10.5194/isprs-archives-XLIII-B2-2020-1419-2020.
[42] W.-C. Huang, Y.-S. Luo, W.-C. Liu, and H.-M. Liu, ‘Deep Learning-Based Crack Detection on Cultural Heritage Surfaces’, *Applied Sciences*, vol. 15, no. 14, p. 7898, July 2025, doi: 10.3390/app15147898.
[43] A. Y. Yiğit and M. Uysal, ‘Automatic crack detection and structural inspection of cultural heritage buildings using UAV photogrammetry and digital twin technology’, *Journal of Building Engineering*, vol. 94, p. 109952, Oct. 2024, doi: 10.1016/j.jobe.2024.109952.
[44] A. Karami, F. Menna, and F. Remondino, ‘Combining Photogrammetry and Photometric Stereo to Achieve Precise and Complete 3D Reconstruction’, *Sensors*, vol. 22, no. 21, p. 8172, Oct. 2022, doi: 10.3390/s22218172.
[45] A. Karami, R. Battisti, F. Menna, and F. Remondino, ‘3D DIGITIZATION OF TRANSPARENT AND GLASS SURFACES: STATE OF THE ART AND ANALYSIS OF SOME METHODS’, *Int. Arch. Photogramm. Remote Sens. Spatial Inf. Sci.*, vol. XLIII-B2-2022, pp. 695–702, May 2022, doi: 10.5194/isprs-archives-XLIII-B2-2022-695-2022.
[46] D. Billi, G. Caroti, and A. Piemonte, ‘Metric Error Assessment Regarding Geometric 3D Reconstruction of Transparent Surfaces via SfM Enhanced by 2D and 3D Gaussian Splatting’, *Sensors*, vol. 25, no. 14, p. 4410, July 2025, doi: 10.3390/s25144410.
[47] I. Toschi, A. Capra, L. De Luca, J.-A. Beraldin, and L. Cournoyer, ‘On the evaluation of photogrammetric methods for dense 3D surface reconstruction in a metrological context’, *ISPRS Ann. Photogramm. Remote Sens. Spatial Inf. Sci.*, vol. II–5, pp. 371–378, May 2014, doi: 10.5194/isprsannals-II-5-371-2014.
[48] J.-A. Beraldin, F. Blais, S. F. El-Hakim, L. Cournoyer, and M. Picard, ‘Traceable 3D Imaging Metrology: Evaluation of 3D Digitizing Techniques in a Dedicated Metrology Laboratory’, presented at the Optical 3D Measurement Techniques, Zurich, 2007, pp. 310–318.
[49] G. Guidi, ‘Metrological characterization of 3D imaging devices’, presented at the SPIE Optical Metrology 2013, F. Remondino, M. R. Shortis, J. Beyerer, and F. Puente León, Eds, Munich, Germany, May 2013, p. 87910M. doi: 10.1117/12.2021037.
[50] M. Trombini, G. Maculotti, D. A. Maisano, A. Pagani, and F. Franceschini, ‘Scaling photogrammetry: A comparative evaluation and metrological assessment across small- and meso-scale domains’, *Precision Engineering*, vol. 92, pp. 124–140, Mar. 2025, doi: 10.1016/j.precisioneng.2024.12.002.

[51] D. Andrews, J. Bedford, and P. Bryan, *Metric survey specifications for cultural heritage*, Third edition. Swindon: Historic England, 2015.
[52] L. MacDonald, 'The limits of resolution', in *EVA London 2010: Electronic Visialisation & Arts. Proceedings of a conference held in London 5 - 7 July*, London: A. Seal, July 2010, pp. 149–156.
[53] E. K. Webb, 'Reflected Infrared and 3D Imaging for Object Documentation', *Journal of the American Institute for Conservation*, vol. 56, no. 3–4, pp. 211–224, Oct. 2017, doi: 10.1080/01971360.2017.1359463.
[54] C. Buzi *et al.*, 'Measuring the shape: performance evaluation of a photogrammetry improvement applied to the Neanderthal skull Saccopastore 1', *ACTA IMEKO*, vol. 7, no. 3, p. 79, Oct. 2018, doi: 10.21014/acta_imeko.v7i3.597.
[55] A. Karami, F. Menna, and F. Remondino, 'INVESTIGATING 3D RECONSTRUCTION OF NON-COLLABORATIVE SURFACES THROUGH PHOTOGRAMMETRY AND PHOTOMETRIC STEREO', *Int. Arch. Photogramm. Remote Sens. Spatial Inf. Sci.*, vol. XLIII-B2-2021, pp. 519–526, June 2021, doi: 10.5194/isprs-archives-XLIII-B2-2021-519-2021.
[56] T. P. Kersten, 'Image-Based Low-Cost Systems for Automatic 3D Recording and Modelling of Archaeological Finds and Objects', in *Progress in Cultural Heritage Preservation: 4th International Conference, EuroMed 2012, Limassol, Cyprus, October 29 - November 3, 2012. Proceedings*, vol. 7616, in Lecture Notes in Computer Science, vol. 7616. , Berlin, Heidelberg: Springer Berlin Heidelberg, 2012. doi: 10.1007/978-3-642-34234-9.
[57] F. Remondino, S. Del Pizzo, T. P. Kersten, and S. Troisi, 'Low-Cost and Open-Source Solutions for Automated Image Orientation – A Critical Overview', in *Progress in Cultural Heritage Preservation*, vol. 7616, M. Ioannides, D. Fritsch, J. Leissner, R. Davies, F. Remondino, and R. Caffo, Eds, in Lecture Notes in Computer Science, vol. 7616. , Berlin, Heidelberg: Springer Berlin Heidelberg, 2012, pp. 40–54. doi: 10.1007/978-3-642-34234-9_5.
[58] L. Es Sebar, L. Lombardo, M. Parvis, E. Angelini, A. Re, and S. Grassini, 'A metrological approach for multispectral photogrammetry', *ACTA IMEKO*, vol. 10, no. 4, p. 111, Dec. 2021, doi: 10.21014/acta_imeko.v10i4.1194.
[59] S. Croci *et al.*, 'Dimensional accuracy assessment of 3D models based on photogrammetry and 3D scanner: a case study from the Museo Egizio of Turin', in *2024 IEEE International Instrumentation and Measurement Technology Conference (I2MTC)*, Glasgow, United Kingdom: IEEE, May 2024, pp. 1–6. doi: 10.1109/I2MTC60896.2024.10561005.
[60] A. Gruen and T. S. Huang, *Calibration and Orientation of Cameras in Computer Vision*. in Springer Series in Information Sciences. Springer Berlin Heidelberg, 2001.
[61] U. Jain, 'Characterization of CMOS Image Sensor', Delft University of Technology, Master of Science in Microelectronics, Delft, 2016.
[62] C. Bonifazzi *et al.*, 'Multispectral imaging of paintings: instrument and applications', presented at the Optical Metrology, C. Fotakis, L. Pezzati, and R. Salimbeni, Eds, Munich, Germany, July 2007, p. 661816. doi: 10.1117/12.726113.
[63] C. Jones, C. Duffy, A. Gibson, and M. Terras, 'Understanding multispectral imaging of cultural heritage: Determining best practice in MSI analysis of

historical artefacts', *Journal of Cultural Heritage*, vol. 45, pp. 339–350, Sept. 2020, doi: 10.1016/j.culher.2020.03.004.
[64] E. K. Webb, 'Reflected Infrared and 3D Imaging for Object Documentation', *Journal of the American Institute for Conservation*, vol. 56, no. 3–4, pp. 211–224, Oct. 2017, doi: 10.1080/01971360.2017.1359463.
[65] J. Dyer, G. Verri, and J. Cupitt, *Multispectral imaging in reflectance and photo-induced kuminescence modes: a user manual*. British Museum London, UK, 2013.
[66] P. A. M. Triolo, *Manuale Pratico di Documentazione e Diagnostica per Immagine per i BB.CC.* in Lineamenti di restauro e conservazione dei Beni Culturali. Il Prato, 2020.
[67] E. Marengo *et al.*, 'Development of a technique based on multi-spectral imaging for monitoring the conservation of cultural heritage objects', *Analytica Chimica Acta*, vol. 706, no. 2, pp. 229–237, Nov. 2011, doi: 10.1016/j.aca.2011.08.045.
[68] E. Nocerino *et al.*, 'MAPPING VIS AND UVL IMAGERY ON 3D GEOMETRY FOR NON-INVASIVE, NON-CONTACT ANALYSIS OF A VASE', *Int. Arch. Photogramm. Remote Sens. Spatial Inf. Sci.*, vol. XLII–2, pp. 773–780, May 2018, doi: 10.5194/isprs-archives-XLII-2-773-2018.
[69] R. Fontana *et al.*, 'Multi-spectral IR reflectography', presented at the Optical Metrology, C. Fotakis, L. Pezzati, and R. Salimbeni, Eds, Munich, Germany, July 2007, p. 661813. doi: 10.1117/12.726096.
[70] F. S. Frey, *The AIC Guide to Digital Photography and Conservation Documentation*, 2nd edn. American Institute for Conservation of Historic and Artistic Works, 2011.
[71] A. Cosentino, 'Practical notes on ultraviolet technical photography for art examination', *Cons. Património*, vol. 21, pp. 53–62, 2015, doi: 10.14568/cp2015006.
[72] N. C. Noya, Á. L. García, and F. C. Ramírez, 'Combining photogrammetry and photographic enhancement techniques for the recording of megalithic art in north-west Iberia', *Digital Applications in Archaeology and Cultural Heritage*, vol. 2, no. 2–3, pp. 89–101, 2015, doi: 10.1016/j.daach.2015.02.004.
[73] K. Bartoš, K. Pukanská, Ľ. Kseňak, J. Gašinec, and P. Bella, 'Cross-Polarized SfM Photogrammetry for the Spatial Reconstruction of Challenging Surfaces, the Case Study of Dobšiná Ice Cave (Slovakia)', *Remote Sensing*, vol. 15, no. 18, p. 4481, Sept. 2023, doi: 10.3390/rs15184481.
[74] F. S. Mortazavi and M. Saadatseresht, 'High Resolution Surface Reconstruction of Cultural Heritage Objects using Shape from Polarization Method', *Int. Arch. Photogramm. Remote Sens. Spatial Inf. Sci.*, vol. XLVIII-2/W2-2022, pp. 85–93, Dec. 2022, doi: 10.5194/isprs-archives-XLVIII-2-W2-2022-85-2022.
[75] A. Richmond, A. L. Bracker, Victoria, and A. Museum, *Conservation: Principles, Dilemmas and Uncomfortable Truths*. in Online access with subscription: Proquest Ebook Central. Elsevier/Butterworth-Heinemann, 2009. [Online]. Available: https://books.google.it/books?id=Kng-D5jmoeUC
[76] S. Munoz-Vinas, *Contemporary Theory of Conservation*, 0 edn. Routledge, 2012. doi: 10.4324/9780080476834.
[77] C. Gagliardi, L. Riparbelli, P. Mazzanti, and M. Fioravanti, 'A Critical Review of Methods and Techniques Used for Monitoring Deformations in Wooden

Panel Paintings', *Forests*, vol. 16, no. 3, p. 546, Mar. 2025, doi: 10.3390/f16030546.
[78] R. Zanuttini, *Il legno massiccio. Materiale per un'edilizia sostenibile*. Compagnia delle Foreste, 2014. [Online]. Available: https://books.google.it/books?id=6-O6oAEACAAJ
[79] L. Uzielli and M. Fioravanti, 'Il Comportamento Fisico-Meccanico Del Legno Nei Dipinti Su Tavola', in *Dipinti su Tavola. La tecnica e la Conservazione dei Supporti*, Edifir., Firenze, Italy, 2000, pp. 37–58.
[80] R. B. Hoadley, 'Chemical and Physical Properties of Wood', in *The Structural Conservation of Panel Paintings: proceedings of a symposium at the J. Paul Getty Museum, 24 - 28 April 1995*, Los Angeles: Getty Conservation Institute, 1998, pp. 2–20.
[81] R. Falciai, C. Trono, G. Lanterna, and C. Castelli, 'Deformation monitoring of wooden works of art using FBG sensors', presented at the Photonics Europe, B. Culshaw, A. G. Mignani, and R. Riesenberg, Eds, Strasbourg, France, Sept. 2004, p. 157. doi: 10.1117/12.548267.
[82] N. P. Van Dijk, E. K. Gamstedt, and I. Bjurhager, 'Monitoring archaeological wooden structures: Non-contact measurement systems and interpretation as average strain fields', *Journal of Cultural Heritage*, vol. 17, pp. 102–113, Jan. 2016, doi: 10.1016/j.culher.2015.03.011.
[83] R. A. Galantucci and F. Fatiguso, 'Advanced damage detection techniques in historical buildings using digital photogrammetry and 3D surface anlysis', *Journal of Cultural Heritage*, vol. 36, pp. 51–62, Mar. 2019, doi: 10.1016/j.culher.2018.09.014.
[84] X. Ma *et al.*, '3D structural deformation monitoring of the archaeological wooden shipwreck stern investigated by optical measuring techniques', *Journal of Cultural Heritage*, vol. 59, pp. 102–112, Jan. 2023, doi: 10.1016/j.culher.2022.11.007.
[85] W. Anaf, A. Cabal, M. Robbe, and O. Schalm, 'Real-Time Wood Behaviour: The Use of Strain Gauges for Preventive Conservation Applications', *Sensors*, vol. 20, no. 1, p. 305, Jan. 2020, doi: 10.3390/s20010305.
[86] V. Tornari, E. Bernikola, N. Tsigarida, M. Andrianakis, K. Hatzigiannakis, and J. Leissner, 'Preventive deformation measurements on cultural heritage materials based on non-contact surface response of model samples', *Studies in Conservation*, vol. 60, no. sup1, pp. S143–S158, Aug. 2015, doi: 10.1179/0039363015Z.000000000219.
[87] R. Luo, Z. Zhou, X. Chu, W. Ma, and J. Meng, '3D deformation monitoring method for temporary structures based on multi-thread LiDAR point cloud', *Measurement*, vol. 200, p. 111545, Aug. 2022, doi: 10.1016/j.measurement.2022.111545.
[88] A. Bandiera, C. Alfonso, R. Auriemma, and M. Di Bartolo, 'Monitoring and conservation of archaeological wooden elements from ship wrecks using 3D digital imaging', in *2013 Digital Heritage International Congress (DigitalHeritage)*, Marseille, France: IEEE, Oct. 2013, pp. 113–118. doi: 10.1109/DigitalHeritage.2013.6743720.
[89] *Freecad. Available at https://www.freecad.org/*.
[90] U. Jain, 'Characterization of CMOS Image Sensor', Master Thesis, Delft University of Technology, Master of Science in Microelectronics, Delft, 2016.
[91] C. Griwodz *et al.*, 'AliceVision Meshroom: An open-source 3D reconstruction pipeline', in *Proceedings of the 12th ACM Multimedia Systems Conference*,

Istanbul Turkey: ACM, June 2021, pp. 241–247. doi: 10.1145/3458305.3478443.
[92] J. Tuesta-Guzmán, W. Solórzano-Requejo, G. Grosso-Salazar, C. Ojeda, and A. Díaz Lantada, 'Innovative Methodology for the 3D Reconstruction of Body Geometries using Open-source Software':, in *Proceedings of the 15th International Joint Conference on Biomedical Engineering Systems and Technologies*, Online Streaming, --- Select a Country ---: SCITEPRESS - Science and Technology Publications, 2022, pp. 162–169. doi: 10.5220/0010870200003123.
[93] I. Đuric, I. Vasiljevic, M. Obradovic, V. Stojakovic, J. Kicanovic, and R. Obradovic, 'Comparative Analysis of Open-Source and Commercial Photogrammetry Software for Cultural Heritage', presented at the eCAADe 2021: Towards a New, Configurable Architecture, Novi Sad, Serbia, 2021, pp. 243–252. doi: 10.52842/conf.ecaade.2021.2.243.
[94] L. Es Sebar, S. Grassini, M. Parvis, and L. Lombardo, 'A low-cost automatic acquisition system for photogrammetry', presented at the 2021 IEEE International Instrumentation and Measurement Technology Conference (I2MTC), Glasgow. United Kingdom, 2021, pp. 1–6. doi: 10.1109/I2MTC50364.2021.9459991.
[95] *Agisoft Metashape*.
[96] K. Kingsland, 'Comparative analysis of digital photogrammetry software for cultural heritage', *Digital Applications in Archaeology and Cultural Heritage*, vol. 18, p. e00157, Sept. 2020, doi: 10.1016/j.daach.2020.e00157.
[97] A. Barbasiewicz, T. Widerski, and K. Daliga, 'The analysis of the accuracy of spatial models using photogrammetric software: Agisoft Photoscan and Pix4D', *E3S Web Conf.*, vol. 26, p. 00012, 2018, doi: 10.1051/e3sconf/20182600012.
[98] G. Vacca, G. Furfaro, and A. Dessì, 'THE USE OF THE UAV IMAGES FOR THE BUILDING 3D MODEL GENERATION', *Int. Arch. Photogramm. Remote Sens. Spatial Inf. Sci.*, vol. XLII-4/W8, pp. 217–223, July 2018, doi: 10.5194/isprs-archives-XLII-4-W8-217-2018.
[99] C. Nicolae, E. Nocerino, F. Menna, and F. Remondino, 'Photogrammetry applied to Problematic artefacts', *Int. Arch. Photogramm. Remote Sens. Spatial Inf. Sci.*, vol. XL–5, pp. 451–456, June 2014, doi: 10.5194/isprsarchives-XL-5-451-2014.
[100] D. Cimino, A. Agostino, P. Artoni, M. Molteni, and C. Daffara, 'Beyond the youth smile: Investigating techniques and materials in Caroto's paintings by analytical single-point analyses and IR reflectography in full-field', *Journal of Cultural Heritage*, vol. 71, pp. 370–381, Jan. 2025, doi: 10.1016/j.culher.2024.12.012.
[101] L. E. Sebar *et al.*, 'Metrological validation of a photogrammetry-based technique', in *2022 IEEE International Instrumentation and Measurement Technology Conference (I2MTC)*, Ottawa, ON, Canada: IEEE, May 2022, pp. 1–6. doi: 10.1109/I2MTC48687.2022.9806510.
[102] '08m52e00 - FARO Edge and FARO Laser ScanArm Manual - April 2016'.
[103] S. Ioannidou and G. Pantazis, 'Detection of Deformations and Alterations in Paintings Using a New Industrial Geodetic Methodology', *J Nondestruct Eval*, vol. 44, no. 2, p. 36, June 2025, doi: 10.1007/s10921-025-01170-4.
[104] *https://cloudcompare.org/index.html*.
[105] J. Markiewicz *et al.*, 'The Quality Assessment of Different Geolocalisation Methods for a Sensor System to Monitor Structural Health of Monumental

Objects', *Sensors*, vol. 20, no. 10, p. 2915, May 2020, doi: 10.3390/s20102915.
[106] I. Lunghi, E. Vannini, A. Dal Fovo, V. Di Sarno, A. Rocco, and R. Fontana, 'A Performance Comparison of 3D Survey Instruments for Their Application in the Cultural Heritage Field', *Sensors*, vol. 24, no. 12, p. 3876, June 2024, doi: 10.3390/s24123876.
[107] G. Masi *et al.*, 'Corrosion investigation of fire-gilded bronze involving high surface resolution spectroscopic imaging', *Applied Surface Science*, vol. 366, pp. 317–327, Mar. 2016, doi: 10.1016/j.apsusc.2016.01.101.
[108] G. Auriti, *Compendio di storia della cultura Giapponese dalla età arcaica alla restaurazione del Meigi (1868)*. Vallecchi, 1954. [Online]. Available: https://books.google.it/books?id=IWNgvItXMzgC
[109] A. Oddy, 'A History of Gilding with Particular Reference to Statuary', in *Gilded Metals: History, Technology, and Conservation*, 1st edn, vol. 1, London: Archetype Books, 2000, pp. 1–19.
[110] E. Darque-Ceretti and M. Aucouturier, 'GILDING FOR MATTER DECORATION AND SUBLIMATION. A BRIEF HISTORY OF THE ARTISANAL TECHNICAL KNOW-HOW'.
[111] P. Jett and W. T. Chase, 'The gilding metals in China', in *Gilded Metals: History, Technology, and Conservation*, 1st edn, vol. 1, London: Archetype Books, 2000, pp. 145–155.
[112] A. Giumlia-Mair, 'Plating and Surface Treatments on Ancient Metalwork', *Advances in Archaeomaterials*, vol. 1, no. 1, pp. 1–26, Dec. 2020, doi: 10.1016/j.aia.2020.10.001.
[113] E. Darque-Ceretti, E. Felder, and M. Aucouturier, 'Foil and leaf gilding on cultural artifacts: forming and adhesion', *Matéria (Rio J.)*, vol. 16, no. 1, pp. 540–559, 2011, doi: 10.1590/S1517-70762011000100002.
[114] S. La-Niece, *Metal Plating and Patination: Cultural, technical and historical developments*. Elsevier Science, 2013. [Online]. Available: https://books.google.it/books?id=XgshBQAAQBAJ
[115] S. La Niece and P. T. Craddock, 'Gilding metals in the Old World', in *Metal llating and Patination: Cultural, Technical and Historical Developments*.
[116] D. Strahan, 'Creating Sacred Images of the Buddha. A Technical Perspective', in *Wisdom Embodied. Chinese Buddhist and Daoist Sculpture in The Metropolitan Museum of Art*, New York: The Metropolitan Museum of Art ; New Haven, Conn. : Yale University Press, 2010, pp. 27–45.
[117] A. M. Pollard, P. Bray, P. Hommel, Y.-K. Hsu, R. Liu, and J. Rawson, 'Bronze Age metal circulation in China', *Antiquity*, vol. 91, no. 357, pp. 674–687, June 2017, doi: 10.15184/aqy.2017.45.
[118] A. M. Pollard, P. Bray, P. Hommel, Y.-K. Hsu, R. Liu, and J. Rawson, 'Bronze Age metal circulation in China', *Antiquity*, vol. 91, no. 357, pp. 674–687, June 2017, doi: 10.15184/aqy.2017.45.
[119] A. M. Pollard, R. Liu, J. Rawson, and X. Tang, 'From Alloy Composition to Alloying Practice: Chinese Bronzes', *Archaeometry*, vol. 61, no. 1, pp. 70–82, Feb. 2019, doi: 10.1111/arcm.12415.
[120] R. Yılmaz, 'K β / K α X-ray intensity ratios for some elements in the atomic number range 28≤Z≤39 at 16.896 keV', *Journal of Radiation Research and Applied Sciences*, vol. 10, no. 3, pp. 172–177, July 2017, doi: 10.1016/j.jrras.2017.04.003.
[121] M. C. Caggiani, A. Cosentino, and A. Mangone, 'Pigments Checker version 3.0, a handy set for conservation scientists: A free online Raman spectra

database', *Microchemical Journal*, vol. 129, pp. 123–132, Nov. 2016, doi: 10.1016/j.microc.2016.06.020.
[122] H. Kwon and L. Kim, 'On-Site Identification of Corrosion Products and Evaluation of the Conservation Status of Copper Alloy Artworks Using a Portable Raman Spectrometer', *Materials*, vol. 18, no. 5, p. 924, Feb. 2025, doi: 10.3390/ma18050924.
[123] G. Ferraris, 'Highlights in mineralogical crystallography', *Crystallography Reviews*, vol. 22, no. 4, pp. 280–282, Oct. 2016, doi: 10.1080/0889311X.2016.1157788.
[124] C. Ricci *et al.*, 'A Technical Study of Chinese Buddhist Sculptures: First Insights into a Complex History of Transformation through Analysis of the Polychrome Decoration', *Coatings*, vol. 14, no. 3, p. 344, Mar. 2024, doi: 10.3390/coatings14030344.